TURUN
YLIOPISTO
UNIVERSITY
OF TURKU

INTERPLAY BETWEEN DYNAMICS OF POLYMERIC TEMPLATES AND ADAPTIVE SYNTHESIS OF SPECIES FROM DYNAMIC COMBINATORIAL LIBRARIES

Dawei Qi

TURUN YLIOPISTON JULKAISUJA – ANNALES UNIVERSITATIS TURKUENSIS
SARJA - SER. AI OSA - TOM. 737 | ASTRONOMICA – CHEMICA – PHYSICA – MATHEMATICA | TURKU 2025

TURUN
YLIOPISTO
UNIVERSITY
OF TURKU

INTERPLAY BETWEEN DYNAMICS OF POLYMERIC TEMPLATES AND ADAPTIVE SYNTHESIS OF SPECIES FROM DYNAMIC COMBINATORIAL LIBRARIES

Dawei Qi

TURUN YLIOPISTON JULKAISUJA – ANNALES UNIVERSITATIS TURKUENSIS
SARJA – SER. AI OSA – TOM. 737 | ASTRONOMICA – CHEMICA – PHYSICA – MATHEMATICA | TURKU 2025

University of Turku

Faculty of Medicine
Institute of Biomedicine
Pharmacology, Drug Development and Therapeutics
Drug Research Doctoral Programme
Medicity Research Laboratory

Supervised by

Senior Researcher Jianwei Li Ph.D.,
MediCity Research Laboratory
Institute of Biomedicine
University of Turku
Turku, Finland

Academician Sirpa Jalkanen M.D. Ph.D.,
MediCity Research Laboratory
Institute of Biomedicine
University of Turku
Turku, Finland

Reviewed by

Scientific Researcher Ignacio Alfonso Ph.D.
Department of Biological Chemistry
Institute for Advanced Chemistry of Catalonia, IQAC-CSIC
Barcelona, Spain

Professor Li-Tang Yan Ph.D.
Institute of Polymer Science & Technology
Department of Chemical Engineering
Tsinghua University
Beijing, China

Opponent

Professor Emeritus Heikki Tenhu Ph.D.
Department of Chemistry
University of Helsinki

The originality of this publication has been checked in accordance with the University of Turku quality assurance system using the Turnitin OriginalityCheck service.

ISBN 978-952-02-0181-4 (PRINT)
ISBN 978-952-02-0182-1 (PDF)
ISSN 0082-7002 (Print)
ISSN 2343-3175 (Online)
Punamusta oy, Joensuu, Finland, 2025

UNIVERSITY OF TURKU
Faculty of Medicine
Institute of Biomedicine
Pharmacology, Drug Development and Therapeutics
Medicity Research Laboratory
DAWEI QI: Interplay Between Dynamics of Polymeric Templates and Adaptive Synthesis of Species from Dynamic Combinatorial Libraries
Doctoral Dissertation, 164 pp.
Drug Research Doctoral Programme (DRDP)
04 2025

ABSTRACT

Dynamic combinatorial chemistry (DCC) utilize reversible covalent reactions to synthesize dynamic combinatorial libraries (DCLs) of interconvertible products. The output of DCL could be directed by the template effect, in a way that the products restructure for self-assembling with the template at the free energy minimum. Typically, the templates are discrete small molecules with relatively elementary chemical structure and static conformation. In this thesis, the dynamics of polymeric template was studied for controlling the self-assembly in DCLs. In general, a polymeric template will complex with the DCL of macrocyclic disulfides (DCMs) synthesized from an anionic dithiol building block, then response with different dynamics interactive with the structural transition of DCMs. As a result, this study brought two new fundamental factors to the template effect, one is the conformational dynamics, another is the entropy-driven configurational dynamics.

In the first project, the conformational dynamics was studied during the folding process of the polymer-DCMs complexation. The DCMs adjusted their structures in real time to adapt with and control the conformational changes during the folding process. The DCMs could further re-adapt to adjust the folding for building high drug-loading content drug delivery systems (DDSs) against drug-resistant cancer.

The second project explored the entropy-driven configurational dynamics in the polymer-DCM complexation. The increased binding of DCMs decreased the conformational entropy. To compensate for the entropy loss, the DCMs restructured for faster binding kinetics and high configurational entropy. While the increased addition of a kosmotropic salt NaCl applied penalty to the solvation entropy, which enhanced hydrophobic aggregation and production of DCMs in larger size.

In the third project, the polymeric templates from the first two projects were combined as a diblock copolymeric template, from which the interplay between two different dynamics was studied. The increased binding of DCMs to the copolymeric template gradually initiated the two dynamics sequentially due to the difference in DCMs' binding affinity to each chain block.

KEYWORDS: Dynamic combinatorial chemistry, template effect, polymer dynamics, macrocyclic disulfides, drug delivery systems

TURUN YLIOPISTO
Lääketieteellinen tiedekunta
Biolääketieteen Laitos
Farmakologia, lääkekehitys ja lääkehoito
MediCity tutkimuslaboratorio
DAWEI QI: Polymeeristen mallien dynamiikan ja dynaamisten kombinatoristen kirjastojen lajien adaptiivisen synteesin välinen vuorovaikutus
Väitöskirja, 164 s.
Lääketutkimuksen Tohtoriohjelma (DRDP)
04 2025

TIIVISTELMÄ

Dynaaminen kombinatorinen kemia (DCC) hyödyntää reversiibelejä kovalenttisia reaktioita luodakseen muuntuvia kombinatorisia kirjastoja (DCL), joita voi ohjata templaattiefektin avulla. Tällöin tuotteet hakeutuvat templaattinsa kanssa kohti matalimman vapaan energian rakennetta. Yleensä templaattina toimii pieni, yksinkertainen ja staattinen molekyyli. Tässä väitöskirjassa tutkittiin polymeeritemplaatin dynamiikkaa DCL-järjestelmän itsejärjestäytymisessä.

Polymeeritemplaatti muodostaa komplekseja makrosyklisten disulfidien (DCM) kanssa, jotka syntyvät anionisesta ditioolirakenneosasta. Sen reaktio DCM-rakenteiden muutoksiin tuo templaattiefektiin kaksi uutta tekijää: konformationaalisen dynamiikan ja entropiaperusteisen konfiguraatiodynamiikan.

Ensimmäisessä projektissa analysoitiin konformationaalista dynamiikkaa laskostumisprosessissa. DCM:t sopeuttivat rakennettaan reaaliaikaisesti ja ohjasivat laskostumista, mahdollistaen korkean lääkeainelatauksen DDS-järjestelmiin lääkeresistenttejä syöpiä vastaan.

Toisessa projektissa tutkittiin entropiaperusteista konfiguraatiodynamiikkaa. Sitoutumisen kasvu alensi DCM:ien konformationaalista entropiaa, joten ne rakentuivat nopeampaan sitoutumiskinetiikkaan ja korkeaan konfiguraatioentropiaan. NaCl-suolan lisäys rajoitti liuotinentropiaa, edistäen hydrofobista aggregaatiota ja suurikokoisten DCM-rakenteiden muodostumista.

Kolmannessa projektissa ensimmäisten tutkimusten polymeeritemplaatit yhdistettiin diblokkikopolymeeriksi, jolla tutkittiin kahden dynamiikan yhteisvaikutusta. DCM:ien sitoutumisen kasvaessa ne käynnistyivät peräkkäin, johtuen erilaisista sitoutumistaipumuksista kopolymeerin lohkoihin.

AVAINSANAT: Dynaaminen kombinatorinen kemia, templaattiefekti, polymeeridynamiikka, makrosykliset disulfidit, lääkeaineen kuljetusjärjestelmät

Table of Contents

Abbreviations

AFM	atomic force microscopy
CCK-8	cell counting kit 8
CPMG	Carr-Purcell-Meiboom-Gill
D	diffusion coefficient
Đ	dispersity
DCC	dynamic combinatorial chemistry
DCL	dynamic combinatorial library
DCMs	dynamic combinatorial library of macrocyclic disulfides
DLC	drug loading content
DLE	drug loading efficiency
DLS	dynamic light scattering
DOSY	diffusion-ordered spectroscopy
DOX	doxorubicin
DP_n	degree of polymerization
GSH	glutathione
HPLC	high-perforemance liquid chromatography
HSQC	heteronuclear single quantum coherence spectroscopy
LCSM	laser confocal scanning microscopy
MIM	mechanically interlocked molecule
M_n	number-average molar mass
MP	mass photometry
MS	mass spectroscopy
M_w	weight-average molar mass
NMR	nuclear magnetic resonance spectroscopy
NOESY	nuclear Overhauser effect spectroscopy
PBS	phosphate buffered saline
R_g	radius of gyration
R_h	hydrodynamic radius
SAXS	small angle X-ray scattering
SCNP	single-chain nanoparticle
SEC	size exclusion chromatrography

Supra-SCNP	supramolecular single-chain nanoparticle
T_2	transverse NMR relaxation time
TEM	transmission electron microscopy
TOCSY	total correlation spectroscopy
XPS	X-ray photoelectron spectroscopy

List of Original Publications

This dissertation is based on the following original publications, which are referred to in the text by their Roman numerals:

I Dawei Qi, Xuncheng Shi, Caihong Lin, Ferdinand Holzhausen, Liljeström Ville, Xun Sun, Jinghui Luo, Leena Pitkänen, Ya Zhu, Jessica Rosenholm, Sirpa Jalkanen, Jianwei Li. Self-Adaptive Synthesis of Non-Covalent Crosslinkers while Folding Single-Chain Polymers. *Angewandte Chemie International Edition*, 2024; 38: e202408670.

II Dr. Jingjing Yu, Dawei Qi, Dr. Ermei Mäkilä, Dr. Lippo Lassila, Prof. Dr. Anastassios C. Papageorgiou, Dr. Markus Peurla, Prof. Dr. Jessica M. Rosenholm, Dr. Zhao Zhao, Prof. Dr. Pekka Vallittu, Dr. Sirpa Jalkanen, Prof. Dr. Chunman Jia, Dr. Jianwei Li. Small-Molecule-based Supramolecular Plastics Mediated by Liquid-Liquid Phase Separation. *Angewandte Chemie International Edition*, 2022; 39: e202204611.

III Dawei Qi, Caihong Lin, Xuncheng Shi, Anastassios C. Papageorgiou, Jianwei Li. High-Entropy Supramolecular Self-Assemblies from Polymer-Directed Dynamic Combinatorial Libraries (Manuscript).

IV Dawei Qi, Caihong Lin, Xuncheng Shi, Sari Granroth, Jianwei Li. Polymersome Fusion against Inter-Particle Electrostatic Repulsion Governed by The Kinetic Pathway from Dynamic Molecular Networks (Manuscript).

1 Introduction

1.1 Dynamic combinatorial chemistry (DCC) and dynamic combinatorial library (DCL)

Dynamic combinatorial chemistry (DCC) is an approach used to realize systems chemistry[1-6]. Unlike conventional chemistry, which focuses on the study of purified compounds, systems chemistry examines the interactive networks of molecular mixtures and their emergent properties at a systems level[7-10]. These properties can differ from and surpass the direct sum of the individual properties of each molecular species.

Specifically, DCC utilizes reversible covalent reactions to organize reactants that act as building blocks for the chemical structures of products. This process creates dynamic combinatorial libraries (DCLs) of products that can restructure themselves by recombining the building blocks over accessible kinetic barriers. Consequently, the yield of certain specific products is enhanced when their chemical structures facilitate downhill processes toward equilibrium at a free energy minimum, or when they favor kinetic asymmetry in out-of-equilibrium DCLs[11-15].

Furthermore, since reversible covalent reactions and supramolecular interactions occur in DCLs, changes in product distribution follow Le Chatelier's principle[16, 17]. This principle states that when the equilibrium of a system is disturbed by changes in factors that determine equilibrium, the system will self-adjust to establish a new equilibrium by counteracting the effect of the change.

Therefore, the output of a DCL can be controlled by altering environmental factors (such as pH, temperature, salts, solvents, etc.), the concentration of the DCL, catalysts, chemical fuels, and molecular self-assembly within the DCL. Specifically, controlling the DCL through self-assembly triggered by the introduction of a template molecule—termed the "template effect"—is an important area in developing functional chemical systems and studying the origin of life[8, 18-21].

1.2 Template effect for controlling the self-assembly in the DCLs

In DCC, the template effect refers to the process by which template molecules within a DCL regulate dynamic covalent reactions and supramolecular self-assembly. This regulation occurs through the assembly of template molecules with both the building blocks and the products in the DCL. The dominant self-assembly between a product species of specific chemical structure and the template molecule at the free energy minimum drives the DCL to amplify this particular product via a downhill energy potential.

By employing template molecules with different chemical structures, the dominant self-assembly and the associated reaction outcomes can be altered, allowing for customizable control over the DCLs. Template molecules can be broadly categorized into small molecules and macromolecules. To date, template molecules have primarily induced host-guest complexes, mechanically interlocked molecules (MIMs), and higher-order self-assemblies such as micelles, nanosheets, nanorods, nanofibers, and droplets formed via liquid-liquid phase separation, among others.

1.2.1 Self-assembly in DCL controlled by small molecular templates

1.2.1.1 Host-guest complexes

Host-guest complexes are perhaps the most well-known and extensively studied molecular assemblies emerging from DCLs. They involve the selective binding between a guest molecule and a complementary host molecule. Small molecular template molecules—such as ions, carbohydrates, short peptides, and amphiphiles—have primarily served as guest molecules to amplify host molecules synthesized from DCLs. This amplification aids in developing catalysts[22-24], sensors[25-28], and other synthetic receptors[29, 30]. Conversely, macromolecular template molecules have mostly acted as host molecules to amplify ligand molecules synthesized from DCLs for applications in materials engineering, drug discovery, and therapeutic delivery.

Typically, host-guest complexation in aqueous buffers is driven by polar interactions and solvophobic effects, encompassing both enthalpy and entropy contributions[31]. When complexation maximizes interactions and minimizes solvent-accessible solvophobic areas, the molecular complex stabilizes at the free energy minimum. Building blocks and guest molecules can be designed with complementary configurations to form desired host-guest complexes with high selectivity and affinity (**Figure 1**)[22, 29, 30].

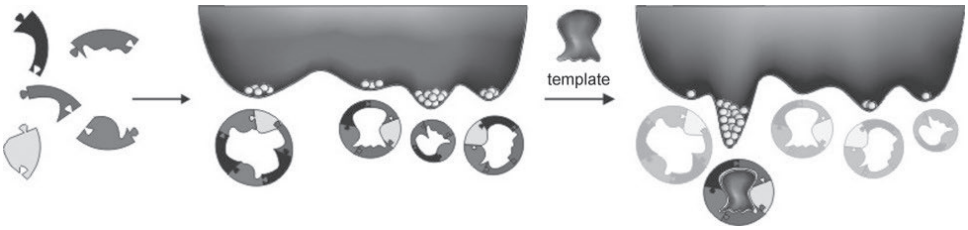

Figure 1 Scheme of template effect in DCLs controlled by host-guest complexation between library members and template molecules. Reprinted with permission from ref.[30]

In pioneering work by the Otto group, DCLs composed of three different anionic dithiol building blocks selectively amplified the production of two macrocyclic receptors, each with a different composition of building blocks, for two distinct cationic small-molecule templates[29]. Later, they found that DCLs operated by two anionic dithiol building blocks could selectively amplify different macrocyclic receptors for 13 kinds of neutral or cationic small-molecule templates, including biologically relevant molecules such as acetylcholine and morphine[30]. This study confirmed that the selective amplification of a specific receptor under the template effect was due to the receptor's binding with the template at the free energy minimum.

In parallel work by the Waters group, multiple well-designed building blocks in DCLs were utilized to develop efficient macrocyclic receptors for highly hydrophilic lysine guests in different methylation states (KMe_n, where n = 1, 2, 3). In their primary study, they identified a small-molecule receptor that selectively recognizes trimethyl lysine (KMe_3) in a histone peptide with native, protein-like affinity[32]. To achieve this, the dithiol building blocks combined aromatic groups and carboxylates to facilitate various interactions. Upon introducing the dipeptide Ac-KMe_3-G-NH_2 as a template, they identified a selective receptor, which could stably interact with the KMe_3 moiety. This receptor demonstrated the potential of small-molecule receptors as alternative sensors for protein post-translational modifications (PTMs). Building upon this success, subsequent work used various building blocks with different structures to yield macrocyclic structures with advanced binding selectivity and affinity for PTMs[25, 33-39].

Based on these solid studies, the Waters group developed a unique sensor array approach using "imprint-and-report" DCLs, eliminating the need for receptor synthesis and isolation (**Figure 2**)[26]. Employing in situ fluorescent indicator displacement analysis, they differentiated analytes using this high-throughput method. This approach led to the development of 19 combinations of three to five DCL data sets capable of discriminating all seven PTMs of methylated arginine and lysine. Moreover, they extended this method to detect and measure betaine, choline, carnitine, and trimethylamine N-oxide (TMAO) metabolites at physiological plasma concentrations[27]. Lastly, they designed a fluorescent sensor array for both individual

perfluoroalkyl substances (PFAS) and complex PFAS mixtures using DCLs with only three building blocks each, enabling rapid detection of PFAS contamination at nanomolar concentrations in water samples from various natural environments[28].

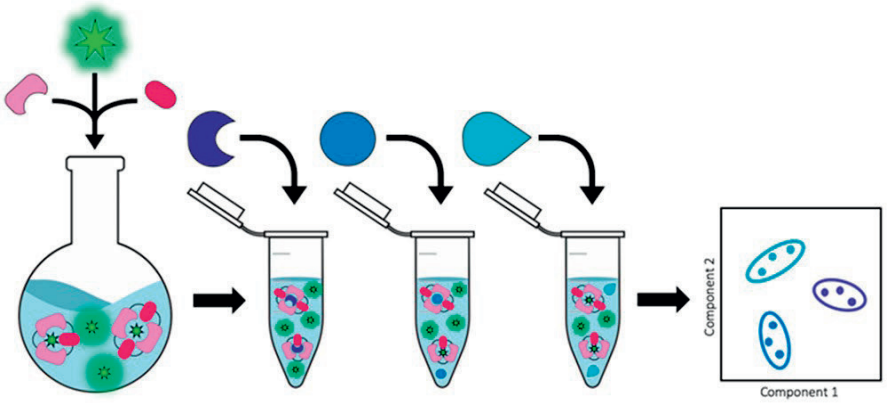

Figure 2 Scheme of the working mode of "imprint and report" DCLs for differential sensing applications. Reprinted with permission from ref.[32]

To develop synthetic receptors capable of binding even more challenging small molecular templates—such as anions, cations, and carbohydrates—the conformational flexibility of the receptor was further exploited to achieve higher binding affinities through induced fit or cooperative binding. The Sanders group developed a linear receptor that binds two $H_2PO_4^-$ anions cooperatively ($K_1K_2 = 8 \times 10^5$ M^{-2}, $K_1 \ll K_2$) from a hydrazone DCL based on a valine-modified ferrocene[40]. From another set of hydrazone DCLs, they developed an efficient macrocyclic receptor for the Li^+ cation ($K \approx 4 \times 10^4$ M^{-1}), observing that the receptor changed its conformation to induce binding[41].

For carbohydrate templates, the Ravoo group created DCLs using a set of tripeptide dithiol building blocks[42]. These building blocks were flanked with two cysteines at the N- and C-termini to equip the thiol side groups and were named based on their central amino acids: Arg, Asp, Glu, Gln, His, Ser, and Thr for hydrogen bonding with carbohydrates; Phe, Trp, and Tyr to facilitate hydrophobic effects; and Gly as an inert spacer. In a DCL templated by N-acetylneuraminic acid (NANA), a His-His cyclic dimer was amplified to bind two NANA molecules cooperatively ($K_1 = 72.7$ M^{-1}, $K_2 = 7.76 \times 10^3$ M^{-1}). Additionally, a Tyr-Tyr cyclic dimer emerged for binding trehalose, and a Thr-Thr cyclic dimer for binding α-D-methylfucopyranoside, both in a 1:1 binding stoichiometry from DCLs templated by these respective carbohydrates.

Furthermore, solvent molecules can function as guest templates to facilitate host-guest complexation. In a co-solvent system, the protic solvent methanol (MeOH) acts as an on-switch for the structural exchange of macrocycles, while the aprotic solvents toluene or benzene serve as templates directing the final structure (**Figure 3**)[43]. Using MeOH alone leads to polymer precipitation in the absence of a templating solvent, and aprotic solvents like benzene or toluene alone do not trigger the reaction.

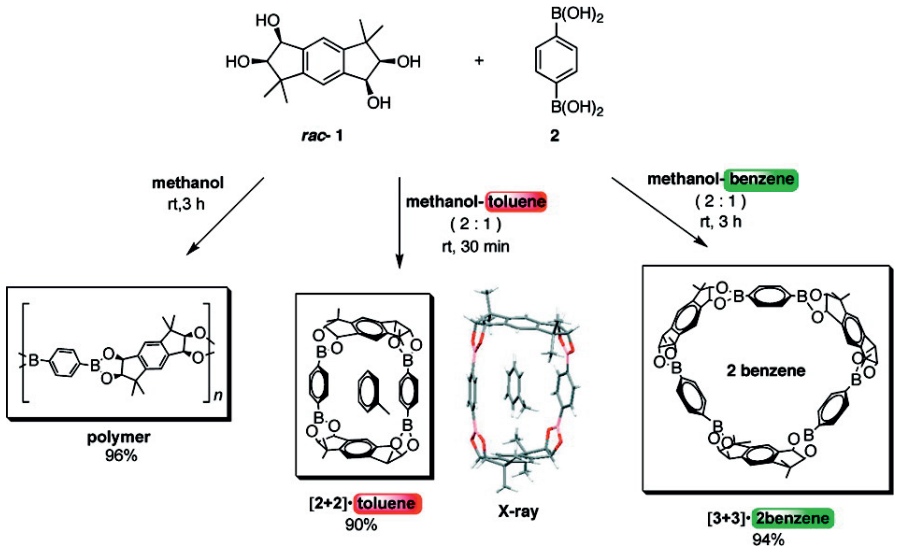

Figure 3 Scheme of solvent templation in a DCL operated by exchange of boronic ester. Reprinted with permission from ref.[43]

In the presence of MeOH (protic) and toluene or benzene (aprotic), the co-solvent can alter the macrocyclization manner of racemic compound 1, selectively forming either 2+2 or 3+3 macrocycles stabilized by the included aprotic solvent molecules. These macrocycles were obtained in high yield, could be isolated by spontaneous precipitation, and were confirmed after recrystallization. The guest solvent molecules could be evaporated to obtain solely the macrocycles. Redissolving the macrocycles into another aprotic solvent resulted in the inclusion of the new solvent guest but did not reshuffle the structure. However, full conversion could be achieved in 1.5 days when MeOH was added as a cosolvent. Additionally, optically pure compound 1 did not induce such efficient selective production of macrocycles. In this self-assembling system, guest-induced precipitation with the packing of enantiomers plays a crucial role in the selective formation of a single macrocyclic boronic ester.

Moreover, through rational design, DCLs can produce binding pockets confined by multiple macrocyclic receptors that bind hydrophilic small molecular guest

molecules with high affinity. To develop efficient anion receptors, the Otto and Kubik groups collaboratively developed a new type of DCL that exchanges the spacers linking two neutral cyclopeptides (**Figure 4**A and B)[44-47]. The DCL can adjust these spacers so that anion templates bind strongly between two linked cyclopeptides with optimized spacing.

Meanwhile, the Otto group explored new possibilities by utilizing two template molecules in a DCL of anionic macrocycles formed via disulfide bonds: γ-cyclodextrin (γ-CD) as the host template and a cationic small-molecule amphiphile as the guest molecule (**Figure 4**C)[48]. The simultaneous presence of these two templates led to the emergence of an allosteric receptor facilitating ternary binding among the two guest molecules and itself. Remarkably, the isolated allosteric macrocycle exhibited high affinity when binding to each of the template molecules separately.

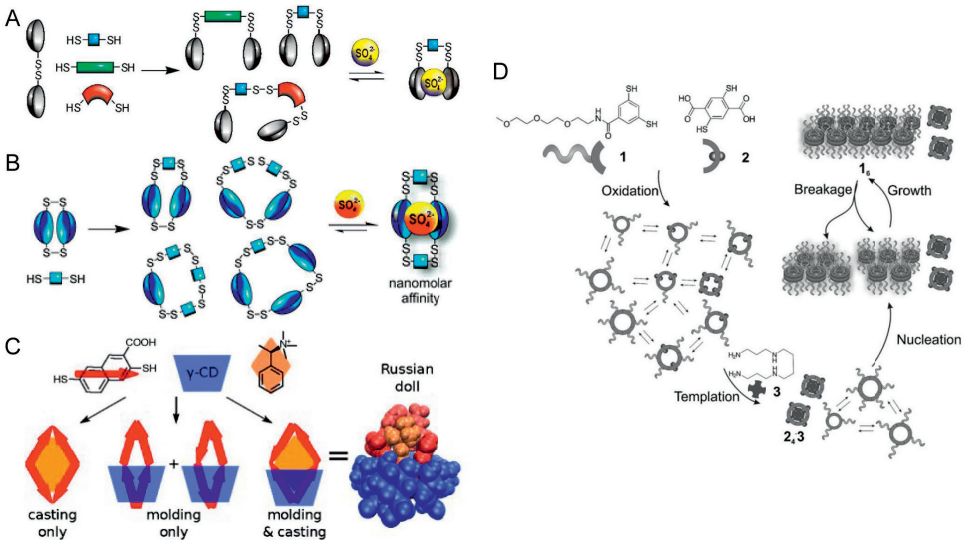

Figure 4 (A) Dimer of neutral cyclic peptide linked by disulfide bond was mixed with a series of dithiol spacer molecules to operate DCLs. Upon introducing anions to the DCL, the most efficient anion receptor will emerge, which would "clip" the bound anion in a confined pocket in micromolar affinity. (B) Dimer of neutral cyclic peptide linked by two disulfide bonds was mixed with dithiol spacer molecules to operate DCLs, which could emerge anion binders using refined binding confinements to achieve nanomolar binding affinity. (C) In a DCL synthesized from an anionic dithiol building block, introducing the host template and guest template at the same time will amplify the allosteric binder for both of the templates. (D) Scheme of the effector-triggered self-replication in coupled system. The effector was a template molecule for amplifying a DCL member by host-guest complexation, which will disentangle the coupled system and release the self-replication process. Reprinted with permission from ref.[44, 47-49]

The Otto group further discovered that host-guest complexation can act as an external effector to release and control the self-replication process of a macrocyclic disulfide (**Figure 4**D)[49]. Initially, in the absence of a template, there was a statistical product mixture from the dithiol building block of a self-replicator catalyzing its own formation through force-induced aggregation, and a dithiol building block that could quantitatively synthesize a high-affinity host under the template effect of a guest effector molecule. The self-replication process was inactive in this mixed dynamic molecular network. However, upon adding the guest effector template, the second building block dissociated from the initial molecular network under the template effect, releasing another building block to resume its self-replication process. By regulating the amount of the guest effector molecule introduced, the onset, rate, and extent of self-replication could be controlled.

1.2.1.2 Mechanically interlocked molecules (MIMs)

Building upon the concept of host-guest molecular complexes—where one molecule is non-covalently encapsulated by another—mechanically interlocked molecules (MIMs) represent a class of compounds in which two or more molecular components are interlocked without covalent bonds[50]. Typical examples include catenanes, knots, and rotaxanes. Due to their advanced complexity, MIMs offer greater conformational variety and dynamic behaviors beyond those of host-guest complexes. This complexity is advantageous for developing molecular machines, switches, sensors, and materials, as the dynamic properties of MIMs are not typically observed in the relatively static host-guest systems. However, these dynamic properties can also make their synthesis, purification, and characterization more challenging due to multiple conformations and interconversions between different states. Currently, most MIMs emerging from DCLs are based on imine and/or disulfide bonds.

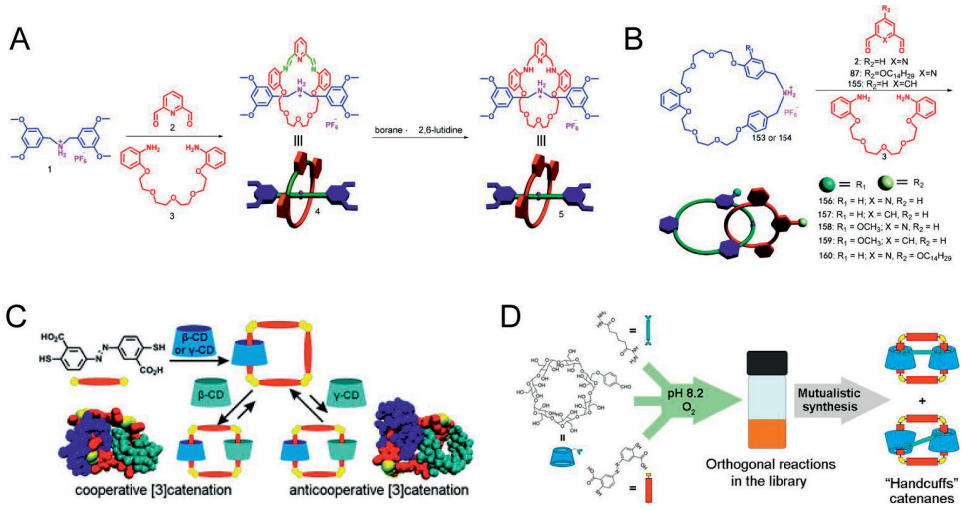

Figure 5 Scheme of the "clipping" strategy for synthesis of rotaxanes (A) and catenanes (B) based on templated imine chemistry. (C) The synthesis of [3]catenanes controlled by cyclodextrin templates in DCLs operated by anionic dithiol building blocks. (D) "Handcuff" catenanes were quantitatively amplified by a hydrazone formation between the template molecules being mutualistic with the formation of a tetrameric macrocyclic disulfides. Reprinted with permission from ref.[51-53]

Imines are reversible bonds with high directionality and a strong ability to act as hydrogen-bond acceptors or coordinate with metal ions via their nitrogen atom[54, 55]. They have been extensively used in DCLs, templated by secondary amine molecules or metal ions to form thermodynamically stable MIMs such as rotaxanes, catenanes, and knots[51, 56]. To prevent the obtained MIMs from decomposing or restructuring through hydrolysis and imine exchange, reductive borohydride reagents can be used to reduce and fix the imine bonds, achieving persistent MIMs.

To form rotaxanes, building blocks capable of imine formation are mixed with a linear template molecule containing non-covalently interactive motifs and inert steric hindrances at its termini. Through non-covalent interactions, the building blocks "clip" around the linear template via imine formation, synthesizing the rotaxane (**Figure 5**A)[51]. For catenane formation, a cyclic template is employed (**Figure 5**B)[51], sometimes utilizing the assistance of sodium ions[57].

Even more complex MIMs, such as molecular knots, have been synthesized by "interweaving" imine molecules using metal ion templates. Structures like Hopf links, Borromean rings, pentafoil knots, and Solomon links have emerged from metal-templated DCLs operated via imine chemistry[51, 55, 56, 58, 59].

Unlike studies where the template molecule directly participates in the MIM's structure, the Sanders group found that an acetylcholine template could quantitatively amplify the [2]catenation of a macrocycle synthesized from DCLs

operated by dynamic imine chemistry[60]. This amplification occurs because the confined binding pocket in the catenane facilitates stable host-guest complexation with the template.

In DCLs operated by building blocks with thiol motifs, the use of additional template molecules for MIM formation is rare. Instead, thiol-flanked building blocks with electron-rich aromatics like dialkoxynaphthalene (DN) and tetrathiafulvalene (TTF), and electron-deficient aromatics such as naphthalenediimide (NDI) and paraquat, have been widely employed to facilitate self-templation for MIM synthesis through electron donor-acceptor interactions[61, 62]. Environmental conditions such as salt concentration and temperature have been found to regulate the yield of MIMs in these systems by adjusting the hydrophobic effect[61, 63, 64].

Moreover, the Link group discovered that thiol-bearing lasso peptides can facilitate MIM formation[65, 66]. They described the self-assembly of catenanes from lasso peptides cleaved at the disulfide bond in their loop region and further extended their work on mechanically interlocked peptides (MIPs). Using a simple, one-pot DCL protocol in water, they synthesized not only catenanes but also rotaxanes, daisy chains, and double-lasso macrocycles.

However, there are examples where additional template molecules are used to synthesize MIMs in DCLs built from thiol building blocks. The Otto group described the development of a new azobenzene-based dithiol building block that predominantly formed a [2]catenane consisting of two interlocked trimers upon oxidation (**Figure 5**C)[52]. In the presence of cyclodextrin (CD) templates, a series of [2]- and [3]-catenanes was formed. Recently, our group advanced the dynamicity and complexity of this strategy by inducing dimerization of the CD templates via imine chemistry to achieve mutualistic synthesis of catenanes (**Figure 5**D)[53]. Specifically, the CD templates were modified with an aldehyde moiety on their hydrophilic surface to yield CD-CHO. CD-CHO alone could not form hydrazone bonds with a small linear dihydrazine co-template molecule. However, in a ternary system containing the azobenzene building block, CD-CHO template, and dihydrazine co-template, a new MIM was formed quantitatively. This MIM consisted of a tetrameric macrocyclic disulfide "handcuffed" by the emergent template—with two CDs linked by one co-template—alongside catalyzed and stabilized hydrazone formation.

1.2.1.3 Higher order of self-assembly

To enhance the complexity and functionality of templated dynamic combinatorial libraries (DCLs), higher-order self-assemblies have been explored. Larger-scale intermolecular supramolecular interactions mediated by small molecular templates can lead to diverse assembly modes with new functions,

including crystallization[24, 67], hydrogelation supported by nanofibers[67], self-replication during aggregation[68], and drug delivery systems[69-73].

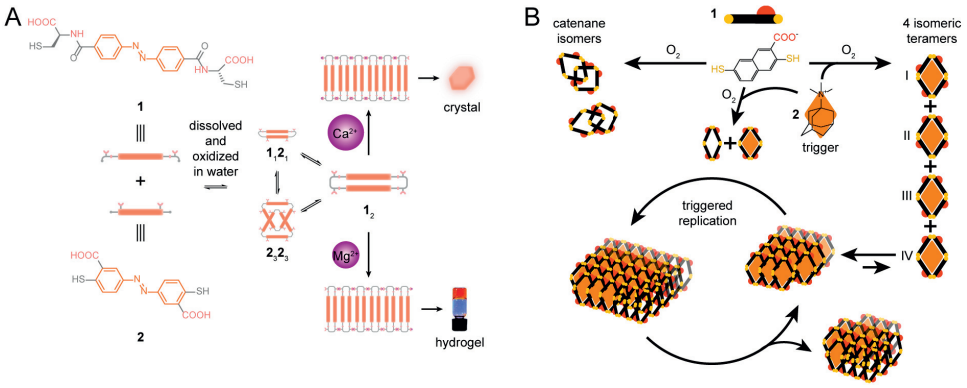

Figure 6 (A) Scheme of stacking self-assembly in DCL controlled by coordinating cation template ions. Modified from ref.[67] (B) Scheme of self-replication process initiated by the aggregation of host-guest complexation mediated by the guest template molecule. Reprinted with permission from ref.[68]

The Otto group discovered that in DCLs of macrocyclic disulfides, an azobenzene-derived dimeric macrocyclic disulfide with a densely packed configuration was particularly effective at inducing self-assemblies akin to supramolecular polymerization, assisted by water molecules and cationic coordinating species (**Figure 6**A)[67]. Initially, its coordination with calcium induced crystallization, revealing cooperative assistance from water molecules and calcium ions in the one-dimensional packing of the macrocycle. When magnesium was used instead of calcium, the self-assembly formed nanofibers of shorter order, supporting hydrogelation. X-ray diffraction (XRD) and cryo-transmission electron microscopy (cryo-TEM) analyses showed that the fibers exhibited characteristic diffraction peaks featuring π-π stacking and had a similar width to the individual dimeric macrocyclic disulfides. This suggested one-dimensional packing mediated by magnesium cations. The resulting hydrogel was self-healing and capable of undergoing reversible sol-gel transitions upon UV irradiation and redox cycles.

Furthermore, the Otto group introduced an additional layer of molecular assembly atop the host-guest inclusion (**Figure 6**B)[67]. This innovative approach led to the two-stage emergence of a self-replicating macrocycle: a thermodynamically controlled initiation process mediated by host-guest inclusion was followed by a kinetically controlled self-replicating self-assembly. Interestingly, the self-assembly of the self-replicating macrocycle catalyzed its own formation even in the absence of the guest molecule.

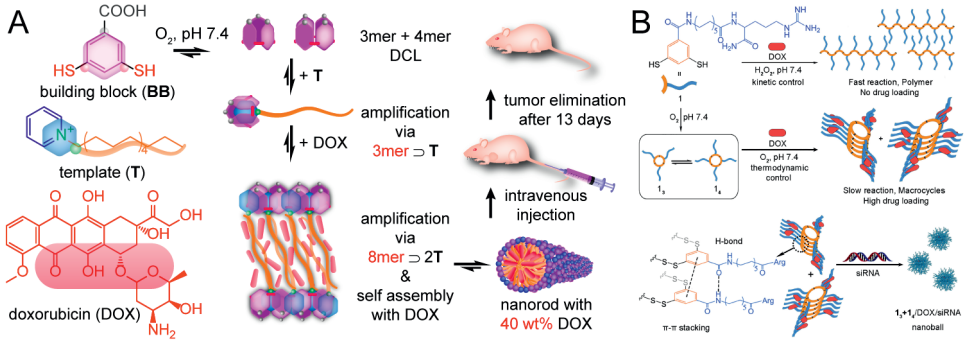

Figure 7 (A) Scheme of the co-self-assembly of nanorod in a self-synthesizing DCL controlled by a surfactant template molecule and a drug template molecule. The obtained nanorod was with high drug loading content and efficient to deliver the drug molecules against the drug resistant cancer both *in vitro* and *in vivo*. (B) Scheme of how thermodynamically controlled and kinetically controlled DCL interacted with the drug template. The thermodynamically controlled DCL could form fibrous self-assembly with the drug template efficiently to building drug delivery systems, which could further co-assemble with siRNA templates to form nanoballs capable of efficiently delivering both drug and gene therapeutics into drug resistant cancer cells to take anti-cancer effect *in vitro*. However, the kinetically controlled DCL could not assemble with the drug molecule in the first place. Reprinted with permission from ref.[72, 74]

Later, they discovered that primary amine templates could facilitate the self-replication of hexameric macrocyclic disulfides formed by oxidation of small dithiol building blocks. Without assistance from the template, the equilibrated DCL exhibited ill-defined self-assemblies with no significantly amplified macrocyclic disulfide species. In stark contrast, upon addition of primary amine templates, the hexameric macrocyclic disulfides dominated the DCL through self-replication during self-assembly with the template[75].

Our group reported a disulfide-exchange-operated DCL of anionic macrocycles involving two template molecules (**Figure 7**A): the cationic surfactant cetylpyridinium bromide (CPBr) and the anticancer drug doxorubicin (DOX)[72]. From this ternary system, an octameric macrocycle emerged, co-self-assembling with the two template molecules to produce nanorods with an ultra-high drug loading content (DLC) of 40.1%. The octameric macrocycle demonstrated high affinity as a host molecule for CPBr with a binding stoichiometry of 1:2. Notably, using only one of the template molecules did not yield the same synthetic or assembly outcome. The nanorods were stable under physiological conditions, effectively delivered the drug to multidrug-resistant ovarian cancer cells, and significantly enhanced the potency of encapsulated DOX both in vitro and in vivo.

Recently, we reported that under physiological pH conditions, cationic dithiol building blocks could slowly convert into thermodynamically controlled macrocycles through mild oxidation by atmospheric oxygen (**Figure 6**B)[74].

Conversely, rapid oxidation of the thiols mediated by the strong oxidant hydrogen peroxide (H_2O_2) resulted in the formation of kinetically controlled polymers. When assembled with DOX, the thermodynamically controlled macrocycles formed macrocycle-DOX-stacked nanofibers with a high DLC of 30.2%. In contrast, the kinetically controlled polymers could not load any drugs. These nanofibers could co-assemble with therapeutic gene siRNA into nanoballs, successfully co-delivering the drug and gene to enhance anticancer efficacy against multidrug-resistant cancer cells in vitro.

1.2.2 Molecular recognition controlled by macromolecular templates

DCC has been widely employed to develop synthetic ligands for biomacromolecules such as proteins and nucleic acids[19-21]. In these applications, DCLs are typically templated by the biomacromolecules themselves to amplify small-molecule ligands that best fit them. However, compared to native biological recognition processes, these small-molecule ligands have limited binding valency and structural complexity when interacting with biomacromolecular templates. To address this limitation, two new methods have been developed by the Fulton group and the Otto group, respectively.

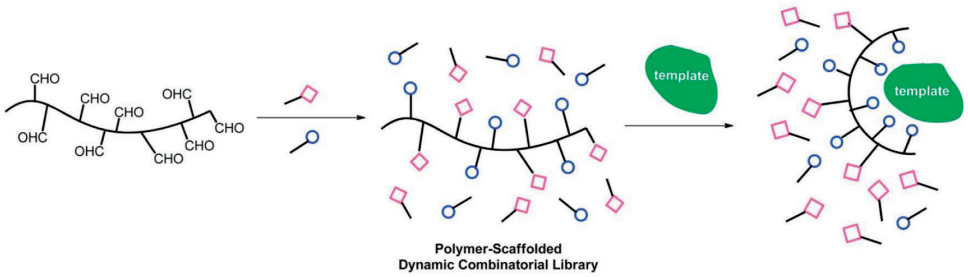

Figure 8 Scheme of polymer-scaffolded dynamic combinatorial library (PS-DCL). The pendants in the scaffold polymer were modified with aldehyde groups, which could undergo hydrazone formation and exchange with the small molecular building blocks modified with hydrazide and molecular recognition groups. Introducing a template molecule into the PS-DCL will trigger the reshuffle both of the chemical components and conformation in the polymer scaffold. Reprinted with permission from ref.[76]

The Fulton group introduced polymer-scaffolded dynamic combinatorial chemistry (PS-DCC)[76-82]. They utilized polymeric aldehydes as macromolecular building blocks—referred to as polymer scaffolds—which react with acylhydrazide building blocks bearing various motifs for supramolecular interactions (**Figure 8**). The resulting DCL products are polymers with pendant modifications in different

sequences, formed via reversible hydrazone bond formation. Moreover, these polymer products can adjust their conformations to bind with biomacromolecular templates. Due to the enhanced binding valency, adaptive motif composition and sequence in the polymer products, and their ability to conformationally adapt for binding, the binding stability was significantly enhanced in biomacromolecule-templated PS-DCC compared to conventional small-molecule DCC.

Similarly, aldehyde groups capable of reversible reactions with hydrazide building blocks were functionalized onto the surface of gold nanoparticles (**Figure 9**A)[83]. Under the guidance of a DNA template, cationic motifs were grafted onto the nanoparticle surfaces through hydrazone bond formation and exchange, effectively transferring the molecular information of the DNA into the grafting pattern on the nanoparticle surfaces. Once the catalyst aniline—required for hydrazone formation—was removed, the hydrazone exchange ceased, and the grafting pattern became kinetically stable. In a parallel approach, amine building blocks were used to functionalize nanoparticle surfaces under the direction of a DNA template[84]. Only the amines that interacted with the DNA reacted with the aldehydes to form imine bonds, thereby becoming fixed on the surface. Although only three types of simple amines were included in the library, their attachment to the surface was highly dependent on the DNA sequence, providing new platforms for synthesizing multivalent, nanoparticle-based receptors for DNA sequence-dependent sensing.

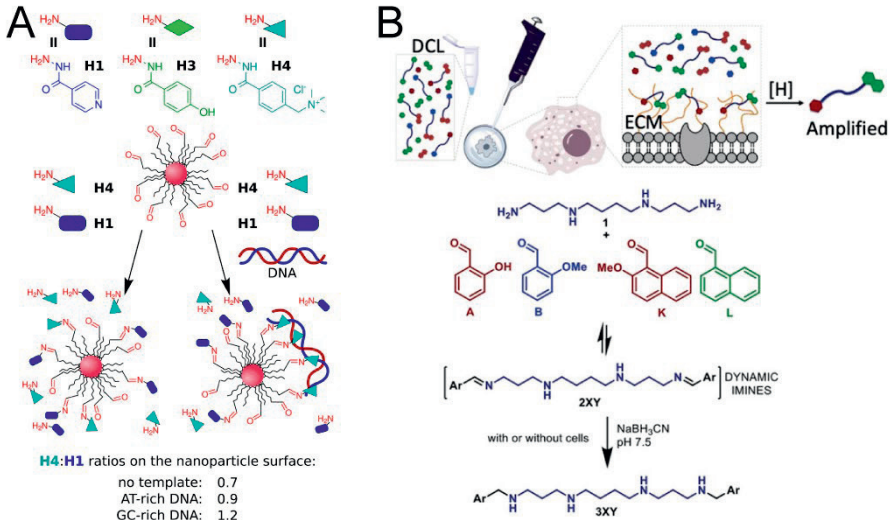

Figure 9 (A) Scheme of DCL operated on the surface of nanoparticle, which was grafted with aldehyde groups that could undergo hydrazone formation and exchange with the building blocks with hydrazide group and molecular recognition groups. The DNA template will reshuffle the DCL to facilitate optimized binding. (B) Scheme of the DCL using the macromolecules on the live cells' surface as template molecules. Reprinted with permission from ref.[83, 85]

Another challenge in using biomacromolecules as templates is operating the templation of DCLs within real, complex biological systems, where numerous biomolecules can influence the DCL, making it difficult to study and regulate molecular interactions. The Alfonso group was the first to advance in this area by utilizing glycosaminoglycans (GAGs)—components of the complex network of glycoproteins and anionic polysaccharides on the cell surface—as templates for a DCL (**Figure 9**B)[85]. In their previous work, a DCL composed of spermine and aldehydes had been shown to yield high-affinity binders for heparins, which share structural similarities with GAGs[86]. In this study, the strongest binder was indeed amplified by the GAG templates on the external cell surface, and binding in this system was monitored using T_2 filter and WATER-LOGSY NMR experiments. Furthermore, two different cell lines, HeLa and A549, each with different compositions of GAGs on their external surfaces, induced different product amplification patterns in the DCL, demonstrating the diagnostic potential of this strategy.

In another advancement, the Boekhoven group investigated the effect of macromolecular templates in out-of-equilibrium DCLs (**Figure 10**B)[87]. They attached nucleobases to isophthalic acid to create building blocks for forming dissipative DCLs. Using the condensing agent EDC, condensation reactions between the acid groups occurred, while simultaneously, hydrolysis of the condensed products took place. These two competing kinetics determined the degree of condensation in the products. Without template molecules, hydrolysis was significant compared to condensation, resulting primarily in dimeric products. However, when templates bearing complementary nucleobases were introduced into the DCLs, oligomeric products were amplified. This amplification was due to kinetic control, which accelerated oligomeric condensation facilitated by the templates' selective concentration of longer oligomers and decelerated hydrolysis owing to hydrophobic protection provided by coacervation between the oligomeric products and the template.

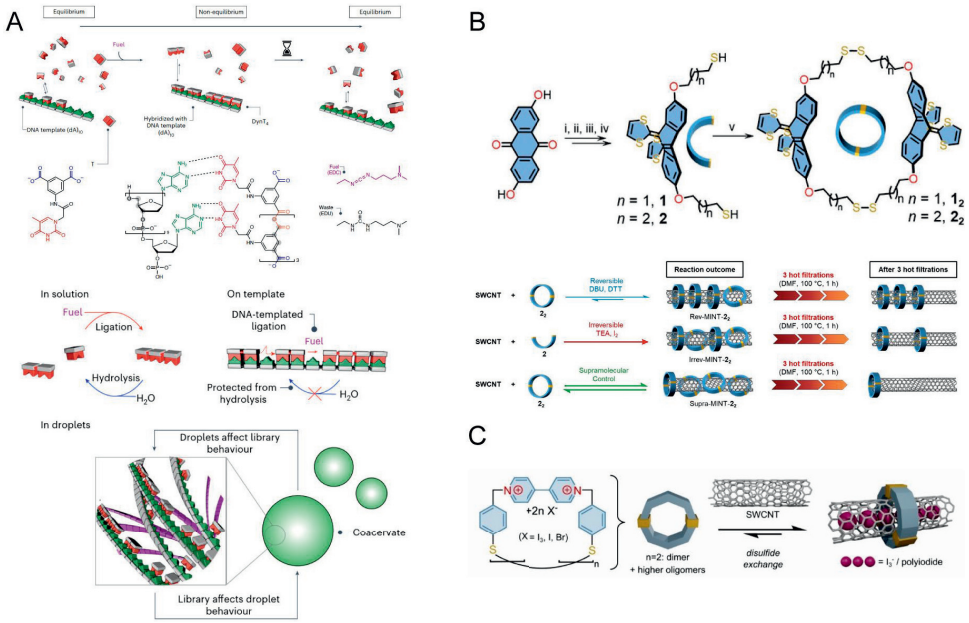

Figure 10 (A) Scheme of the DNA templated dissipative DCL. The building block with equipped with two carboxylate acid groups for operating dissipative condensation reactions fueled by EDC, and one thymine group for molecular recognition with the adenosine units in the DNA template. The interaction between the oligomer of building block and the DNA template accelerate the oligomerization and decclerate the hydrolysis by protection, thereby enhance the oligomerization by kinetic control. In turn, the enhanced oligomerization drove the coacervation and affect the fusion behaviors of the coacervates. (B) Scheme of the synthesis of the macrocyclic disulfide, and its installation methods to the single-walled carbon nanotubes (SWCNTs). (C) Treatment of cationic macrocyclic disulfides with counter ions to the SWCNTs lead to the simultaneous inside (counter ion) and outside (macrocyclic disulfide) functionalization to the SWCNTs. Reprinted with permission from ref.[87, 88]

Recent work has demonstrated that reversible disulfide exchange reactions can be used to install mechanically interlocked disulfide macrocycles on one-dimensional nanotubes (**Figure 10**B)[88]. This approach resulted in size-selective functionalization, which could be beneficial for purifying nanotube mixtures. The reversible disulfide exchange reactions, occurring under mild conditions, enabled the installation of large amounts of mechanically interlocked disulfide macrocycles on nanotubes. The size-selective functionalization arose from error correction mechanisms and the presence of relatively rigid, curved π-systems in the key building blocks. In their subsequent work, the dynamic combinatorial library of triiodide salts of cationic macrocyclic disulfides assembled with nanotubes in aqueous solvent differently: the cationic macrocycle encapsulated the nanotube from the outside, while the anionic triiodides inserted into the interior of the nanotube (**Figure 10**C)[89].

1.3 Dynamic combinatorial libraries of macrocyclic disulfides (DCMs)

Macrocycles have been a predominant configuration of products in DCLs due to their ability to control the spatial arrangement of guest molecules, leading to intricate and stimuli-responsive molecular assemblies. These assemblies have enabled potential applications in drug delivery, sensing, catalysis, living chemical systems, smart materials, and more. Macrocycles are formed by the cyclization of molecular building blocks, a process that competes with linear polymerization. By designing amphiphilic building blocks, the cyclized conformations can achieve a lower free energy level than linear ones through a more compact and solvophilic outer shell, reducing exposure of the solvophobic portions[31, 90]. Thus, when building blocks are linked by reversible reactions in a DCL, cyclization can efficiently outcompete linear polymerization, as the DCL spontaneously favors the production of macrocyclic products at the free energy minimum.

Among all the macrocycles synthesized from DCLs, dynamic combinatorial macrocyclic disulfides (DCMs)—linked by disulfide bonds—have gained significant attention due to their unique features. First, their formation, reversion, and exchange are spontaneous and efficient in the presence of mild oxidizing agents (e.g., oxygen), nucleophilic attackers (e.g., hydroxide anion), or free radicals (e.g., sulfur/oxygen radicals) in aqueous environments over a broad pH range[91-95]. Consequently, organized by these highly dynamic and efficient covalent reactions, the product outcome is highly sensitive to changes in environmental factors and molecular assemblies.

In comparison, macrocycles from DCLs operated by alkyne or olefin metathesis require iterative design and screening of catalysts when using building blocks with different structures and in various environments. Additionally, macrocycles linked by imine bonds or Schiff bases present challenges between reversibility and stability, or oligomerization and cyclization, related to pH, solvent, reactive motif structure, and temperature[54, 55].

Moreover, at lower pH values, the dynamic covalent reactions of DCMs or their thiol precursors can be switched off because the formation of thiolates—a necessary intermediate for redox and exchange reactions—is strongly inhibited by protonation[95]. Thus, the responsiveness is turned off upon deactivating the reactions, fixing the product distribution. However, if the pH is adjusted back to sufficiently basic values, the dynamic covalent reactions operating the DCMs can be reactivated. This pH-controlled on/off switching provides easily accessible protocols for gating, purification, and characterization using standard techniques.

Additionally, DCMs can be driven out of equilibrium by treatment with chemical stimuli such as free thiols, thiolates, free radicals, or by inputting sufficient kinetic energy from light, stress, heat, or sound to cleave the disulfide bonds. These features

provide responsive, complex synthetic systems for stable and stimuli-responsive macrocycles or their assemblies. This behavior is valid over a wide pH range from slightly acidic to basic, including physiological pH.

In terms of non-covalent organization, the rotational flexibility of the disulfide bond allows for a broad range of macrocycle conformations[95]. This flexibility is essential for facilitating solvation, induced fit, supramolecular polymerization, and folding processes of DCMs[96-98]—diversified features that have been difficult to achieve with macrocycles formed by rigid reversible covalent bonds such as imines[55], boronic esters[24], alkynes[99], and olefins[100-102].

Lastly, and most importantly, the diverse dynamic covalent reactions associated with DCMs—including thiol oxidation, thiol-disulfide exchange, and disulfide interchange—can exhibit different kinetic and thermodynamic features depending on the substitution groups linked to the sulfur atom[95]. This variability results in markedly different dynamic molecular networks among DCMs. As a result of these unique merits, research on DCMs has significantly expanded over the last 20 years.

1.3.1 Dynamic covalent chemistry of the DCMs

In most cases, DCMs are obtained by preparing DCLs by dissolving building blocks containing multivalent thiol groups in a solvent. Understanding the chemical processes from the starting building blocks to the final equilibrium or kinetic intermediate states of the DCLs is pivotal for controlling their emergent properties. Since all the DCLs studied in this thesis were prepared in phosphate buffer, this section will focus on the dynamic covalent chemistries occurring in aqueous environments, which include thiol oxidation, thiol-disulfide exchange, and disulfide interchange.

1.3.1.1 Thiol-oxidation

The products and pathways of thiol oxidation are diverse. Thiols can be oxidized into disulfides and other sulfur species with higher oxidation states than disulfides. The oxidation pathways can be nucleophilic, electrophilic, or enzymatic. When thiols are oxidized into disulfides by ambient oxygen in aqueous buffer, generally three steps are followed (**Figure 11**)[95]:

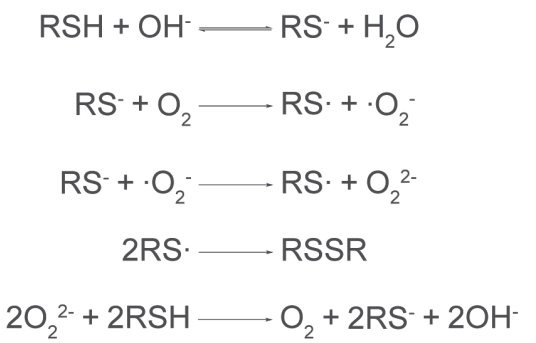

Figure 11 General mechanism of thiol oxidation in basic aqueous solvent systems at atmospheric pressure.

1. Deprotonation: Thiols are deprotonated to form thiolates.
2. Oxidation: The thiolates are oxidized by oxygen to form thiyl radicals.
3. Combination: The thiyl radicals combine to produce disulfides.

However, sometimes the thiolate group is too stable—for example, thiolates reduced from Ellman's reagent—and ambient oxygen is insufficient to further oxidize the thiolate. In such cases, stronger oxidants like hydrogen peroxide (H_2O_2) are needed to facilitate oxidation toward disulfide bonds.

1.3.1.2 Thiol-disulfide exchange

Thiol-disulfide exchange can be described as a nucleophilic substitution reaction or a redox reaction. The process involves (**Figure 12**)[95]:

Formation of Thiolates: Thiols are deprotonated by hydroxide ions to form thiolates, which act as nucleophiles.

Exchange Reaction: Thiolates attack disulfide bonds, reshuffling them and forming a new thiolate and disulfide bond.

This means the sulfur atoms in the thiolate and disulfide bond are exchanged after the reaction. Alternatively, viewed as a redox reaction, a thiolate is oxidized by a disulfide bond, and a sulfur atom in the disulfide bond is reduced by the oxidized thiolate into a new thiolate. The kinetics of thiol-disulfide exchange can be rapid and may dominate over thiol oxidation and disulfide interchange. However, it is necessary for the thiolate and disulfide groups to be in the same phase for the exchange to occur.

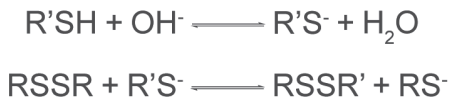

Figure 12 Scheme of general mechanism of thiol-disulfide exchange in basic aqueous solvent systems at atmospheric pressure.

1.3.1.3 Disulfide interchange

When all thiols in the reaction system are fully oxidized into disulfides, exchange between disulfide bonds can still occur if the disulfide bonds are active enough to undergo ionic nucleophilic scission via alkaline hydrolysis. The process involves (**Figure 13**)[91, 93, 95]:

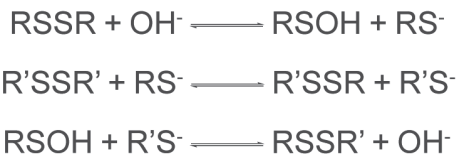

Figure 13 Scheme of general mechanism of the disulfide interchange in basic aqueous solvent systems at atmospheric pressure.

Hydrolysis: Hydroxide ions attack the disulfide bond, hydrolyzing it into two parts—a thiolate motif and a sulfenic acid motif. Both are metastable because the thiolate is more nucleophilic toward sulfur atoms than the hydroxide ion.

Recombination: The thiolate attacks another disulfide bond to form a new pair of thiolate and disulfide bond or substitutes the hydroxide anion from a sulfenic acid motif to reform a disulfide bond.

This process repeats spontaneously, facilitating extensive interchange of disulfide bonds in the system.

However, this ionic scission is only valid for disulfide bonds substituted by electron-withdrawing groups, which are active enough for alkaline hydrolysis. For example, diaryl disulfide bonds are generally active for interchange. In contrast, dialkyl disulfide bonds, having electron-donating characteristics, are generally too stable to be hydrolyzed under these conditions. Consequently:

Aryl Thiol Building Blocks: DCLs synthesized from aryl thiol building blocks are usually thermodynamically controlled regardless of the oxidation rate of thiols, provided there is no other kinetic trap offered by molecular assembly.

Alkyl Thiol Building Blocks: DCLs synthesized from alkyl thiol building blocks tend to be kinetically controlled if the oxidation rate of thiols is faster than the rate of thiol-disulfide exchange.

Understanding these distinctions is crucial for manipulating the dynamic behavior of DCLs and achieving desired properties in macrocyclic disulfides.

1.4 Aims of this thesis: exploiting dynamics from polymeric templates for DCMs to control supramolecular self-assembly

DCLs templated by small molecules—with limited recognition valency—or by well-organized macromolecules like proteins and nucleic acids have already demonstrated promising functions. However, these templates often possess rigid conformations. This thesis explores the use of polymer templates that exhibit controllable high multivalency and highly dynamic topology/conformation to introduce an additional layer of complexity and dynamics into DCLs. Specifically, I investigate how polymeric templates with different dynamic behaviors affect the self-assembly and synthesis within DCLs.

Polymers possess greater structural complexity than small molecules, making them ideal for generating unique template effects not attainable with small-molecule-directed DCLs. The conformation of a polymer chain extends beyond the sum of its monomers and exhibits diverse, stable thermodynamic equilibrium states[103]. Monomer interactions determine the free energy levels of possible conformations, reshaping the chain into its most favorable states. For example, polymer chains can adopt conformations ranging from collapsed globules due to strong attraction, random coils due to inert interactions, to extended rods due to long-range repulsion—each presenting different levels of entropic elasticity. To better manipulate polymer among different states for controlling properties and functions in materials and chemical systems, polymer dynamics had been studied extensively as an important research topic[104]. Furthermore, there had been even more complex polymer dynamics upon the confinement of polymer by porous materials, surfaces, and nanoparticles, which facilitated the development of functional materials[105, 106]. This variability offers DCLs opportunities to manipulate higher-level structural responsiveness, self-assembly and functions.

Moreover, compared to small monomers dissolved in solution, monomer units within a polymer backbone have restricted movement. As a result, the recognition moieties of polymers can cooperate with adjacent moieties to amplify specific library species that cannot be amplified by freely dissolved corresponding small monomers, even if they share the same recognition sites. This unique confinement in polymers can lead to intriguing template effects that are not simply extrapolations of small-molecule behavior.

Beyond the potential for discovering new template effects to enhance the fundamental concept of DCC, polymer templates offer practical application

advantages. Generally, polymer-based materials exhibit higher kinetic barriers between conformational states, making them more stable than materials self-assembled from small molecules. One advanced application of polymers is in controlled drug delivery. Compared to drug delivery systems (DDSs) self-assembled from small molecules, polymer-based DDSs are safer and more efficacious, as they can control the rate, timing, and location of drug release in the body. However, in the complex biochemical environments within cancer patients, conventional covalent synthesis and screening methods hinder the rational and reproducible synthesis and sufficient parallel screening needed to acquire stable yet responsive DDSs with high drug loading content (DLC).

1.4.1 Conformational Dynamics

Firstly, I explore conformational dynamics of polymeric template affect the synthesis and self-assembly in the polymer-templated DCMs. After a template molecule is polymerized, its spatial arrangement is dictated more by the polymer's conformation than by Brownian motion. The confinement of template units means that their conformational state determines the best-fit binding and guides the synthesis of library members, leading to new thermodynamic control over the output of DCC. Interestingly, as library members bind to the templates as monomer units, they can also alter the conformation of the polymeric template. Since monomer interactions determine the free energy landscape of the conformational space, this reshapes the chain into conformations at the free energy minimum. This means we can control the conformation of the polymer via DCC. To understand conformational dynamics in DCC with polymeric templates, we need to address the fundamental scientific question: How do chemical exchange and conformational exchange interact with each other?

1.4.2 Entropy-Driven Configurational Dynamics

Next, I investigate how the entropy-driven configurational dynamics of polymeric template function in polymer-templated DCMs. During supramolecular complexation, polymers exhibit multiple significant entropic features. Driven by the second law of thermodynamics, which requires a net gain of entropy after a spontaneous process, the various entropy contributions from a polymer can become an interactive network that controls chemistry and self-assembly in DCC. There are three main entropy features being exploited in this project. The first is conformational entropy, determined by all the current exchangeable states of the polymer's conformation. A stretched or fully collapsed polymer has minimal entropy, while a polymer in a fully random coil conformation has maximal entropy. The

second is configurational entropy after supramolecular complexation, decided by all the exchangeable states of binding configurations. Faster kinetics during binding increase configurational entropy by increasing the configurational dynamics. The third is solvation entropy, influenced by the polymer's restriction on the movement of associated solvent molecules, which decreases entropy. At a critical point, the polymer may fold or aggregate to counter this decrease in solvation entropy. In this study, I attempt to suppress one type of entropy at a time to observe how the others respond and direct self-assembly in DCC.

1.4.3 Combined Dynamics

In systems chemistry, we are not satisfied with a single mode of dynamics within a chemical system; we are interested in how different types of dynamics work together. Numerous studies have explored how various dynamic covalent reactions can operate simultaneously in a single chemical system. These reactions can be orthogonal or communicating, working concurrently or separately. Such working modes not only increase the system's complexity—better mimicking life behaviors—but also empower chemical systems as molecular machinery and functional hydrogels. In stark contrast, due to the lack of dynamics in conventional templates, there has been little research on the template effect in this context. Now, thanks to the new dynamics introduced by polymeric templates, we can build a chemical system with different dynamics originating from the template itself and study how they work together. Therefore, in the third part of my thesis, I aim to investigate what new emergent properties appear when these two dynamics operate together from the same polymeric template.

2 Experimental Methods

2.1 Preparation of the DCLs

Stock solutions of building blocks, macrocyclic disulfides, and templates at high concentrations (30-40 mM) were prepared immediately before the preparation of the DCL. The solvent used was a phosphate buffer of KH_2PO_4 at pH 7.4. The stock solutions were then mixed and diluted in various ratios to achieve the designated concentrations in the DCLs. The DCLs were stirred at 500 rpm at room temperature (~23 °C) with continuous exposure to air. Evaporated water was replenished daily. For the drug-loading DCLs, doxorubicin was first thoroughly mixed with the polymer before introducing the macrocyclic disulfides. To remove unbound doxorubicin, the DCLs were centrifuged at 16,000 g for 30 minutes after reaching equilibrium. The supernatant was discarded and replaced with fresh buffer to restore the original volume.

2.2 High Perforemance Liquid Chromatrography-Mass Spectrometry (HPLC-MS)

10 µL of the supernatant from the DCLs was diluted with 190 µL of acetonitrile containing 1 v% trifluoroacetic acid (TFA) in preparation for injection. Analytical HPLC experiments were performed using an Ultimate 3000 HPLC system with a reversed-phase column (Macherey-Nagel EC 125/4 Nucleosil 100-5 C18 HPLC column) at 40 °C. The eluent flow rate was 1.0 mL/min, with eluent A consisting of H_2O (0.1 v% TFA) and eluent B of acetonitrile (0.1 v% TFA).

Table 1. Eluent gradient of the HPLC-MS analysis. From original publication I.

Time (Minutes)	A (%)	B (%)
0	80	20
23	0	100
25	80	20
30	80	20

Mass spectrometry was conducted using the Bruker Daltonics micrOTOF in negative ion mode.

For Van 't Hoff equation fitting, the 1.8**A**-*y***P** DCLs and control DCL 1.8**A** were incubated at each temperature for 24 hours to reach equilibrium, as no further changes in the composition of $\mathbf{A}_n$ (as indicated by HPLC analysis) were observed after 24 hours. After reaching equilibrium at each incubation temperature (295.1 K, 303.1 K, 308.1 K, 313.1 K, 318.1 K, 323.1 K, 328.1 K, 333.1 K), samples for HPLC analysis were taken immediately to prevent further chemical exchange. The samples were then returned to the incubator to equilibrate at the next temperature.

From the HPLC analysis results for each DCL at each temperature, the concentration of $\mathbf{A}_3$ or $\mathbf{A}_4$ was determined using the formula: $[\mathbf{A}_n] = 1.8(I_n/I_{total})/n$, where I_n represents the peak area of the $\mathbf{A}_3$ or $\mathbf{A}_4$ species, and I_{total} is the total peak area summed from all $\mathbf{A}_n$ species. The equilibrium constant, $\ln K_{eq}$, for the conversion of $\mathbf{A}_3$ to $\mathbf{A}_4$ was calculated as $\ln([\mathbf{A}_4]/[\mathbf{A}_3])$. Fitting $\ln K_{eq}$ and T to a modified Van 't Hoff equation: $\ln K_{eq} = a + b/T + c/T^2$, allowed the determination of $\Delta H_{reaction}$ and $\Delta S_{reaction}$ at room temperature (296.1 K) using the fitted values of a, b, and c: $\Delta H_{reaction} = -R(b + 2c/T)$, $\Delta S_{reaction} = -R(a - c/T^2)$, where R is the ideal gas constant.

By subtracting the $\Delta H_{reaction}$ or $\Delta S_{reaction}$ of the control DCL 1.8**A** from that of the 1.8**A**-*y***P** DCL, the $\Delta\Delta H_{reaction}$ or $\Delta\Delta S_{reaction}$ of the 1.8**A**-*y***P** DCLs was obtained. Finally, $\Delta\Delta H_{total} = \Delta\Delta H_{reaction}[\mathbf{A}_4]/3$, and $\Delta\Delta S_{total} = \Delta\Delta S_{reaction}[\mathbf{A}_4]/3$.

2.3 Size Exclusion Chromatography (SEC)

The experiments were conducted using an Agilent 1260 Infinity II Multi-Detector GPC/SEC System (Agilent Technologies, Santa Clara, CA, USA) equipped with two Agilent 7.5 mm × 300 mm PL aquagel-OH MIXED-M columns and a 7.5 mm × 50 mm PL aquagel-OH guard column. The eluent was an aqueous solution at pH 3 containing 0.3 M Na_2SO_4 and 0.5 M CH_3COOH, with a flow rate of 1 mL/min. The polymer was dissolved in the eluent at a concentration of 5 mg/mL by stirring for 24 hours, then filtered through a 0.22 μm aqueous syringe filter before injection into the SEC system, with an injection volume of 100 μL. Poly(2-vinylpyridine) (Sigma Aldrich) was used as the standard to construct the calibration curve. The number-average molar mass (M_n), weight-average molar mass (M_w), dispersity (Đ), and degree of polymerization (DP_n) for $\mathbf{PT}_{703}$ were determined based on the refractive index signal data.

2.4 Nuclear Magnetic Resonance Spectroscopy (NMR)

For sample preparation, DCLs were prepared in a deuterated phosphate buffer (D_2O) at pD 7.4. NMR spectroscopy was conducted using an 850 MHz Avance III HD, a 600 MHz Bruker AVANCE-III NMR system, or a 500 MHz Bruker AVANCE-III NMR system, all equipped with cryoprobes. The sample temperature was maintained at 298 K. Before each NMR experiment, pulse calibrations (p1 and p2) were performed.

TOCSY and NOESY experiments were conducted using the mlevphpp and noesygpphpp pulse programs, respectively. The DOSY experiment was performed with the ledbpgp2s pulse program with linear decay. Signal decay was kept below 5% residual signal by adjusting Δ and δ using the ledbpgp2s1d pulse program. Transverse relaxation time (T_2) was measured using the Carr-Purcell-Meiboom-Gill (CPMG) NMR experiment. Data processing and analysis were completed with Topspin software.

For fitting NMR data from the *x***A**-9**P** DCLs to the Langmuir isotherm according to a previously reported method, the concentration of $\mathbf{A}_3$, $\mathbf{A}_4$, $\mathbf{A}_5$ or $\mathbf{A}_6$ in each DCL was calculated using $[\mathbf{A}_n] = 1.8(I_n / I_{total}) / n$, where I_n represents the peak area of the species with a specified n, and I_{total} is the total peak area summed from all $\mathbf{A}_n$ species. The change in chemical shift (Δδ) for He in the *x***A**-9**P** DCLs was calculated by subtracting the chemical shift of H_e in the 9**P** sample (9 mM **P** in deuterated phosphate buffer at pD = 7.4). Δδ and concentration data from each *x***A**-9**P** DCL were fitted to a three-component Langmuir isotherm: $\Delta\delta = a_1[\mathbf{A}_3] + b_1[\mathbf{A}_3]/(c_1 + [\mathbf{A}_3]) + a_2[\mathbf{A}_4] + b_2[\mathbf{A}_4]/(c_2 + [\mathbf{A}_4]) + a_3([\mathbf{A}_5] + [\mathbf{A}_6]) + b_3([\mathbf{A}_5] + [\mathbf{A}_6])/(c_3 + ([\mathbf{A}_5] + [\mathbf{A}_6]))$. Parameter c represents the dissociation constant (K_D) for each species. However, the fitted K_D values are only apparent and intended for qualitative comparison, as the fitting assumes identical binding sites for each $\mathbf{A}_n$ species, which does not fully account for the complex binding dynamics of **P**.

NOESY experiments were conducted using the noesygpphpp pulse program with D8 = 0.1 ms on the 600 MHz Bruker AVANCE-III NMR system equipped with a cryoprobe. To avoid spin diffusion in the NOE results, D8 of 0.1 ms was selected based on a general rule of thumb used in the NOESY experiments for macromolecules.

Saturation Transfer Difference (STD) NMR was conducted using the stddiffesgp.3 pulse program, with D1 = 2 s, D20 = 1.5 s, off-resonance at -40 ppm, and on-resonance at 0 ppm on the 500 MHz Bruker AVANCE-III NMR system.

DOSY experiments were performed with the ledbpgp2s pulse program with linear decay on the 600 MHz Bruker AVANCE-III NMR system equipped with a cryoprobe. Signal decay was kept below 5% residual by adjusting Δ and δ using the ledbpgp2s1d pulse program. The apparent diffusion coefficient (D) was obtained by

fitting the DOSY data to the one-component decay function: $I = I(0)\exp[-(\gamma g\delta)^2 D(\Delta-\delta/3)]$. To differentiate between contributions to D from free and bound $\mathbf{A}_n$, D was fitted for the $\mathbf{A}_n$ species using a two-component decay function: $I = I_1(0)\exp[-(\gamma g\delta)^2 D_1(\Delta-\delta/3)] + I_2(0)\exp[-(\gamma g\delta)^2 D_2(\Delta-\delta/3)]$. Since the D of protons in polymer $\mathbf{P}_{90}$ was on the order of 10^{-11} m²/s, and the D of protons in the free $\mathbf{A}_n$ DCL was on the order of 10^{-10} m²/s, initial guesses for D_1 and D_2 were set to 1×10^{-10} and 1×10^{-11}, respectively, to represent free and bound $\mathbf{A}_n$.

T_2 was measured using the Carr-Purcell-Meiboom-Gill (CPMG) NMR experiment on the 850 MHz Bruker AVANCE-III NMR system equipped with a cryoprobe. The experimental parameters were D1 = 15 s, D16 = 0.0002 s, and D20 = 0.0005 s, with a loop counter sequence of 2, 4, 6, 8, 10, 12, 16, 32, 64, 128, 256, 512, 1024, 2048, 4096, and 8192. The fitting function was $I = I(0)\exp(-t/T_2)$. All data were processed and analyzed with Topspin software.

2.5 Small Angle X-ray Scattering (SAXS)

Phosphate buffer (for background subtraction), 15 mM $\mathbf{PT}_{703}$ and 3**A**-15$\mathbf{PT}_{703}$ were the samples analyzed. Synchrotron SAXS (small-angle X-ray scattering) experiments were performed at the X12SA beamline, cSAXS, at the Swiss Light Source (Villigen, Switzerland). Sample solutions were placed in 1 mm diameter quartz capillaries. X-rays were used at 12.4 keV, and 200 measurements of 0.25 s each were recorded across 10 positions along the length of the capillary, which was mounted at a detector distance of 200 mm. Background measurements with buffer only were taken using identical capillaries, positions, and measurement protocols. Data analysis was conducted using Matlab 2022 and SasView 4.2.2. Guinier analysis was applied to each sample, assuming very small angles ($q < 1.3/R_g$).

2.6 Mass Photometry (MP)

Measurements were conducted using a Refeyn TwoMP-Auto mass photometer. All samples were diluted 500-fold in their original phosphate buffer, prepared with NaOH and 120 mM KH_2PO_4 at pH 7.4. Molecular mass measurements were performed immediately after dilution to minimize concentration-induced chemical re-equilibration. The calibration standard, bovine serum albumin, was diluted to 20 nM in the same phosphate buffer as the samples just before the experiments.

2.7 Dynamic Light Scattering (DLS)

The samples were diluted 10-fold in the original buffer before measurements on the Zetasizer Nano-ZS (Malvern Instruments Ltd., Worcestershire, UK) equipped

with a 633 nm He-Ne ion laser. Dynamic light scattering (DLS) was recorded at a 173° backscattering angle and converted into a number-averaged size distribution. All measurements were conducted at 23 °C, with operating parameters automatically optimized by the Zetasizer software.

2.8 Refractometry

For high-accuracy measurements, polyethylene pipettes were used to place 1 mL of each sample on the polished measuring surface of the refractometer prism (Anton Paar Abbemat 300, LED wavelength 589 nm), ensuring the sample was positioned at least 1 mm above the prism surface. Each sample was tested three times at a temperature of 23 °C.

2.9 Transmission Electron Microscopy (TEM)

Formvar film-coated copper grids (EMCN^{TM}, Beijing Zhongjingkeyi Technology Co., Ltd) were glow-discharged prior to sample application. The sample was then applied to the discharged grid film, followed immediately by negative staining with an aqueous solution of uranyl acetate. Transmission electron microscopy (TEM) was performed on a JEM 1400 Plus (JEOL) at 80 kV.

2.10 Atomic Force Microscopy (AFM)

The experiment was conducted in contact mode using a JPK Nanowizard I and a PNP-DB-20 probe (200 μm length) purchased from NanoAndMore GmbH. In order to initiate the self-assembly, 10 mM **ADM** and 40 mM **CTAB** were dissolved and mixed in H_2O by adding NaOH to adjust the pH to 10. Aliquots of the sample were taken and diluted by 10 times after 5 minutes and 15 minutes for AFM image acquisition. 20 μL of the diluted sample was applied to a freshly cleaved mica substrate. The sample was air-dried in a laminar flow hood, then rinsed with ultrapure water and air-dried again before imaging.

2.11 Rheometry

The bulk rheometry was carried out by the Haake Rheo Stress 300 rheometer, using a parallel plate 20 mm in diameter.gap. The sample was loaded under a 0.3 mm gap and trimmed, then sealed with silicone oil to prevent water evaporation. The amplitude sweep employed the following parameter set: γ: 0.01% ~ 3000% logarithmically changed, 5 data points per decade; ω: 10 rad/s; F_N control activated, floating within 0.5 ~ 0.6 N.

2.12 X-ray Photoelectron Spectroscopy (XPS)

The fused polymersomes were collected by centrifugation and washed three times with water, each wash followed by centrifugation. The resulting powder was air-dried before undergoing XPS analysis.

X-ray photoelectron spectroscopy (XPS) measurements were performed using a Thermo Scientific Nexsa spectrometer equipped with a monochromated, micro-focused Al Kα X-ray source (hν = 1486.6 eV) with a 250 μm spot size in an ultrahigh vacuum chamber. The pass energy and energy step were set to 200 eV/1.0 eV for survey spectra and 50 eV/0.1 eV for high resolution core-level spectra.

2.13 Turbidity Measurement

Immediately before measurement, the sample was diluted tenfold with its buffer and placed into a cuvette with a 0.5 mm path length. The diluted sample was then analyzed using a UV-Vis spectrophotometer (Perkin Elmer Lambda 365) to measure its absorbance at 700 nm, serving as an indicator of the sample's turbidity.

2.14 Drug Release Experiment

Each 10 μL SCNP-DOX sample (n = 3) was mixed with 9 mL buffer (pH 7.4, pH 5.8, pH 7.4 with 5 μM glutathione (GSH), and pH 5.8 with 5 μM GSH) in 15 mL centrifuge tubes and placed on a shaker at 120 rpm and 37 °C. At each time point, 1 mL was taken from each tube, centrifuged at 16,000 g for 30 minutes, and 100 μL of the supernatant was analyzed by HPLC to determine the amount of released drug. The sampled tubes were promptly refilled with buffer to the original volume, vortexed, and returned to the shaker.

2.15 Cell Culture

The multi-drug resistant NCI/ADR-RES human ovarian cancer cell line was kindly provided by Prof. Maria Vilanova from the Department of Biology at Universitat de Girona and the Biomedical Research Institute of Girona, Spain. The cell line originated from Dr. Ramon Colomer at the Institut Català d'Oncologia de Girona, Hospital Universitari de Girona, Spain. Cells were cultured in Dulbecco's Modified Eagle Medium (DMEM), supplemented with 10% fetal bovine serum (FBS, Biowest, Riverside, United States), 4 mM L-Glutamine, 50 U/mL penicillin, 50 μg/mL streptomycin, 3 μM doxorubicin, and 3 μM paclitaxel, in a humidified incubator at 37 °C with 5% CO_2. Cells were confirmed to be free of Mycoplasma contamination and propagated according to established protocols.

2.16 Cell Viability Test

Cells were cultured in 96-well microplates at a density of 7.0×10^3 cells per well. After overnight adhesion, the culture medium was replaced with fresh medium. For the control group ($n = 6$), the original culture medium was used. For the experimental groups ($n = 6$), the medium was supplemented with **PT**$_{703}$, 3**A**-15**PT**$_{703}$ and doxorubicin in various forms (free DOX, polymer-DOX (15**PT**$_{703}$-2.3DOX) and Supra-SCNP-DOX (3**A**-15**PT**$_{703}$-2.3DOX)). The concentrations of **PT**$_{703}$ and 3**A**-15**PT**$_{703}$ matched those in 3**A**-15**PT**$_{703}$-2.3DOX for each corresponding concentration of doxorubicin. After 24 hours, all wells were cleaned, rinsed, and refilled with CCK-8 working solution (Dojindo Molecular Technologies, Munich, Germany) in a 1:10 v/v ratio of CCK-8 to culture medium. Additionally, a blank group ($n = 6$) without cells was treated with CCK-8 solution. After 1 hour of incubation, absorbance at 450 nm was measured using a microplate reader (Cytation 5, BioTek, Agilent Technologies). Cell viability was calculated as: *cell viability* (%) $= 100\% \times (Abs_{exp} - Abs_{blank})/(Abs_{control} - Abs_{blank})$. The cytotoxicity profile was fitted to a logistic function: $y = A_2 + (A_1 - A_2) / (1 + (x / x_0)^p)$.

2.17 Lasor Confocal Scanning Microscopy

Cells (2.5×10^4) were cultured in each 35 mm confocal petri dish and allowed to adhere overnight. The cells were then treated with fresh medium supplemented with doxorubicin in various forms (free DOX, polymer-DOX (15**PT**$_{703}$-2.3DOX), and SCNP-DOX (3**A**-15**PT**$_{703}$-2.3DOX)). After 4 hours of incubation, each dish was rinsed three times with PBS. Live cell staining was performed in the dark. A 2 mL Lysotracker Deep Red solution (Molecular Probes, Thermo Fisher Scientific), diluted 1:20,000 in DMEM, was incubated with the cells for 15 minutes to visualize lysosomes. After three PBS rinses, a 2 mL Hoechst 33342 solution (Molecular Probes, Thermo Fisher Scientific), diluted 1:20,000 in PBS, was incubated with the cells for 15 minutes to stain cell nuclei. Each dish was rinsed and then supplemented with 2 mL of PBS prior to imaging.

Confocal imaging was conducted using a 3i Marianas CSU-W1 spinning disk microscope with 50 µm pinholes. Excitation and emission settings were as follows: 405 nm excitation and 445/45 nm emission for cell nuclei, 561 nm excitation and 617/73 nm emission for doxorubicin, and 640 nm excitation and 692/40 nm emission for lysosomes. Data was processed using ImageJ.

2.18 Flow Cytometry

Cells were seeded in 6-well plates at a density of 4×10^5 cells per well. After overnight adhesion, the medium was replaced. The control group ($n = 3$) received

the original culture medium, while the experimental groups (n = 3) were treated with free DOX, polymer-DOX, or SCNP-DOX at an equivalent doxorubicin concentration of 0.072 mM. Cells were incubated for 4 hours, then harvested and washed three times with phosphate-buffered saline (PBS) before analysis on the BD LSRFortessa (BD Biosciences). Side scatter (SSC) and forward scatter (FSC) were used to discriminate doublets and identify the cell population, and the PE-Cy5 channel was used to assess doxorubicin internalization.

3 Results and Discussion

3.1 Conformational dynamics: self-adaptive synthesis of DCMs as non-covalent crosslinkers for single-chain folding of polymeric template

The conformational dynamics of biomacromolecules such as DNA, RNA, and peptides are fundamental to biological function, enabling precise control and regulation of essential biochemical processes[107-109]. Peptide folding, driven by non-covalent interactions, is particularly crucial in biological activities like enzyme catalysis, transmembrane protein transport, and antigen binding[109, 110]. Inspired by these natural processes, synthetic approaches have attempted to mimic biological folding by using crosslinkers that non-covalently interact with recognition sites on polymers to create supramolecular single-chain nanoparticles (Supra-SCNPs)[111-114]. However, a primary challenge arises because these synthetic non-covalent crosslinkers often have fixed chemical structures, while the molecular environment around their binding sites changes throughout the folding process. This variability leads to inconsistent association strengths between the crosslinkers and the polymer, limiting effective control over the folding.

In contrast, nature employs highly adaptable strategies to facilitate folding with precise timing. Biological systems dynamically regulate the structures of non-covalent crosslinkers according to the folding stage. For instance, molecular chaperones act as transient non-covalent crosslinkers, binding to peptides to promote conformational changes and stabilize folding intermediates; they are then downregulated to permit the binding of subsequent molecules[115, 116]. Additionally, post-translational modifications occur at specific times to modify intra-peptide non-covalent interactions, guiding folding toward the correct configuration[117, 118]. Without these adaptive mechanisms, proteins can misfold or aggregate, leading to dysfunction[116, 119, 120]. The natural system's ability to adapt crosslinker structures in response to folding progression highlights the importance of such structural adjustments in achieving precise control. Inspired by this, hetero-functional polymers and orthogonal crosslinking chemistries have been developed to improve control over synthetic polymer folding[114, 121-124]. However, current prefabricated

crosslinkers still fall short of emulating the real-time adaptations seen in natural folding processes.

To address this limitation, we developed a self-regulating system where the synthesis of non-covalent crosslinkers in a DCL autonomously adapts in response to the polymeric template's simultaneous folding process. Polymer folding, governed by thermodynamics, involves complex conformational chemical environments and progresses through kinetic intermediate states toward its most stable structure at thermodynamic equilibrium[103, 112, 114]. When folding occurs in the polymeric template of a DCL, the complex conformational environment could spontaneously amplify non-covalent crosslinkers from the DCL with strong associations in different folding regimes. This amplification could assist the polymer in navigating transitional states and enhances stability. Moreover, the dynamic nature of folding would allow for dynamic templation of species evolution in DCLs, facilitating real-time adaptive structural adjustment of the crosslinkers, which could result in time-dependent dynamic interactions between the folding and DCC processes.

Specifically, we used a cationic linear homopolymer as the polymeric template and an anionic dithiol building block to synthesize the DCL of macrocyclic disulfides (DCMs). Upon interaction between the polymeric template and DCMs bearing opposite charges, they neutralize each other and initiate folding driven by the hydrophobic effect. First, we studied the adaptation mechanism of DCMs to folding under equilibrium conditions. Then, we investigated the dynamic interaction between the DCMs and folding through kinetic experiments. Finally, we utilized the adaptation mechanism and dynamic interaction in this system to build high-loading-content drug delivery systems against drug-resistant cancer.

By synchronizing polymer folding with self-adaptive synthesis from DCLs, we push the boundaries of dynamic combinatorial chemistry and achieve dynamic, stepwise control over synthetic polymer folding into Supra-SCNPs. This integration offers the potential for synthetic polymers to attain functionalities comparable to those of proteins, advancing our understanding of folding dynamics and control. Our system introduces a new approach to mimic the adaptive, real-time regulation observed in natural protein folding, providing a promising foundation for creating synthetic polymers with sophisticated, protein-like behavior.

3.1.1 Synthesis and characterization of the polymeric template and small molecular template

Initially, both polymeric and small-molecule templates were designed and synthesized for comparative studies. We synthesized the cationic polymeric template poly[3-(methacryloylamino)propyl]trimethylammonium chloride with a degree of polymerization (DP_n) of 703, referred to as $\mathbf{PT}_{703}$, to serve as the folding scaffold.

The inherent positive charge of the monomer units causes the polymer to adopt an elongated conformation in aqueous solution, priming it for subsequent folding.

PT$_{703}$ was synthesized via reversible addition–fragmentation chain-transfer (RAFT) polymerization (**Figure 14**A). Specifically, 0.016 mmol (0.0065 g, 1.00 eq) of 4-cyano-4-[(dodecylthio)carbonothioyl]thio]pentanoic acid (**CTA**, >97%, TCI) was used as the chain-transfer agent, and 0.004 mmol (0.0014 g with ~20 wt% H_2O, 0.25 eq) of 4,4′-azobis(4-cyanovaleric acid) (ACVA, 98%, Alfa Aesar) served as the initiator. The monomer, [3-(methacryloylamino)propyl]trimethylammonium chloride (**MAPTAC**, 50 wt% aqueous solution, 4.44 g, ~10.80 mmol, ~675 eq, Sigma-Aldrich), along with the CTA and initiator, were dissolved in 15 mL of a mixed solvent of water and dimethylformamide (H_2O/DMF = 2:1 v/v) in a Schlenk flask. The polymerization was conducted at 75 °C for 8 hours under a nitrogen atmosphere. The product, **PT**$_{703}$ (1.98 g), was obtained by freeze-drying after dialysis against water (molecular weight cutoff [MWCO] 3,000) for 7 days, with the water changed every 12 hours.

The chemical structure of **PT**$_{703}$ was confirmed by ^{1}H NMR spectroscopy in D_2O (**Figure 14**B), with proton peaks assigned accordingly. The DP_n was determined based on the integration areas of H_b, H_e, and H_f: $DP_n = (I_e + I_f) / (13(I_b / 18))$. Furthermore, the molecular weight distribution of **PT**$_{703}$ was characterized by size exclusion chromatography (SEC, **Figure 14**C).

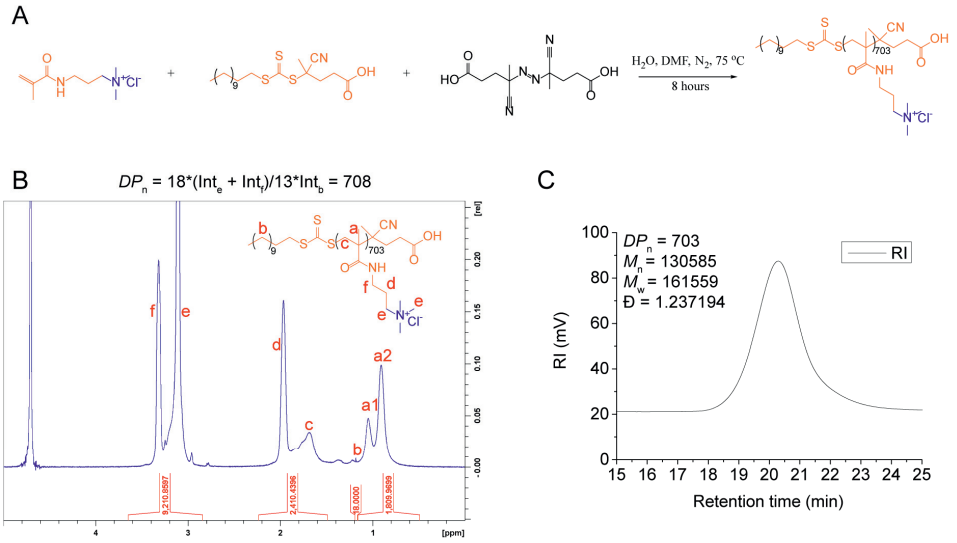

Figure 14 (A) Scheme of the RAFT polymerization of **PT**$_{703}$. (B) ^{1}H NMR spectrum of 15 mM polymeric template **PT**$_{703}$, dissolved in D_2O. NMR spectroscopy was operated at 298 K and 600 MHz. The DP_n was determined from the integration area of the H_e and H_f from the monomer pendants, and the integration area of H_b from the polymer terminus. (C) The SEC trace of **PT**$_{703}$, recorded by the RI channel. The distribution of molecular weight was derived by referencing with the SEC traces of the standard samples with known molecular weight distribution. From original publication I.

In this study, the concentration of **PT**$_{703}$ is expressed in terms of its monomer concentration to clearly represent the amount of cationic pendant groups.

To mimic the monomer unit of **PT**$_{703}$ and avoid Michael addition between olefinic and thiol groups, we designed and synthesized a small-molecule template, (3-acetamidopropyl)trimethylammonium chloride (**ST**, **Figure 15**A). First, N-(3-(dimethylamino)propyl)acetamide was synthesized according to a previously reported method[125]. Subsequently, 15 mmol (2.3888 g, 1 eq) of N-(3-(dimethylamino)propyl)acetamide and 9.5 mL (~22 g, 10 eq) of iodomethane (>99%, Sigma-Aldrich) were mixed and refluxed under a nitrogen atmosphere for 2 days. After completion, the crude product was obtained by rotary evaporation and washed with acetone to yield 3.61 g of (3-acetamidopropyl)trimethylammonium iodide, with an 80% yield. Finally, the iodide in the crude product was exchanged for chloride by incubating the aqueous solution of the crude product with AgCl. The chemical structure of **ST** was confirmed by ^{1}H NMR spectroscopy (**Figure 15**B), ^{13}C NMR spectroscopy (**Figure 15**C), and mass spectrometry (**Figure 15**D).

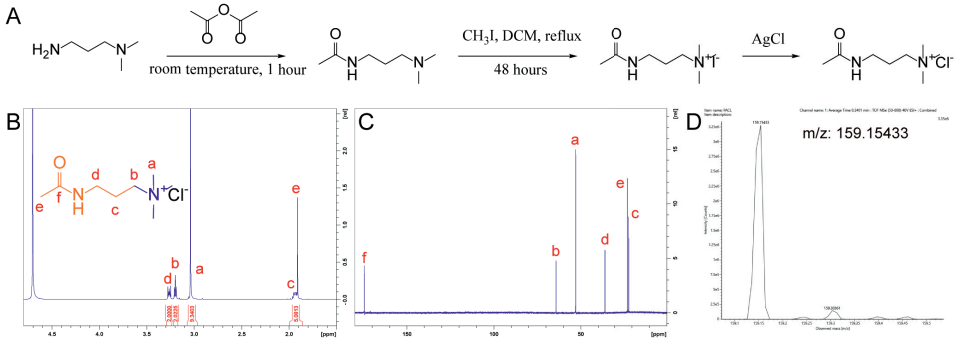

Figure 15 (A) Scheme of the synthetic route of **ST**. (B) ^{1}H NMR spectrum (dissolved in D_2O at 15 mM, 298 K, 600 MHz), (C) ^{13}C NMR spectrum (dissolved in D_2O at 64 mM, 298 K, 150 MHz), and (D) mass spectrum of the small molecular template **ST**. m/z calculated $[M\text{-}Cl^-]^+$ = 159.1492, m/z found: 159.1543. From original publication I.

3.1.2 Synthesis and characterization of the thiol building block **A**, DCMs $\mathbf{A}_n$, and **ADM**

All the main DCMs used for studying the dynamics of the polymeric template in this thesis are based on the classic anionic dithiol building block **A**. Under physiological conditions, building block **A** becomes deprotonated, acquiring a negative charge. Upon exposure to air, its thiol groups undergo oxidation to form disulfide bonds. This process yields DCMs denoted as $\mathbf{A}_n$, which are capable of both thiol-disulfide exchange and disulfide interchange. Consequently, changes in the chemical environment around $\mathbf{A}_n$—including variations in concentration, temperature, and template addition—can trigger adaptive readjustments in the product distribution of $\mathbf{A}_n$.

The interaction between $\mathbf{A}_n$ and the pendant groups of $\mathbf{PT}_{703}$ leads to charge neutralization, which induces the polymer's folding through hydrophobic effects among the neutralized segments. This folding process alters the chemical environment around $\mathbf{A}_n$, allowing the structure of the non-covalent crosslinker $\mathbf{A}_n$ to adapt during folding.

In this thesis, the total concentration of any $\mathbf{A}_n$ library is expressed in terms of its equivalent concentration calculated from building block **A**.

The synthesis of building block **A** followed the procedure described in previous reports[29, 126] (**Figure 16**A). Briefly, 3,5-bis(dimethylthiocarbamoyloxy)benzoic acid methyl ester was synthesized via esterification between methyl 3,5-dihydroxybenzoate (>99%, TCI) and *N,N*-dimethylthiocarbamoyl chloride (>99%, TCI). This intermediate was then transformed into 3,5-bis(dimethylcarbamoylsulfanyl)benzoic acid methyl ester through the Newman–Kwart rearrangement. Finally, 3,5-dimercaptobenzoic acid (**A**) was obtained by de-esterification and acidification of 3,5-bis(dimethylcarbamoylsulfanyl)benzoic acid.

All reactions were carried out under nitrogen protection. The synthetic outcomes were confirmed by ^{1}H NMR spectroscopy (**Figure 16**B and C) and mass spectrometry (MS, **Figure 16**D).

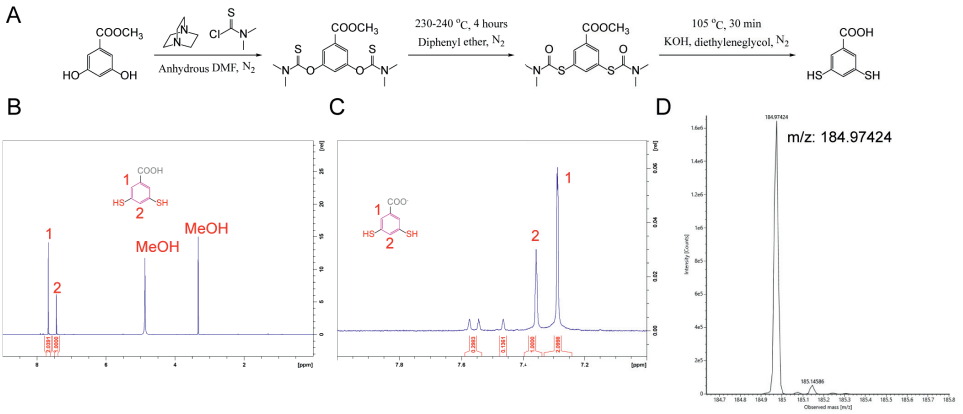

Figure 16 (A) Scheme of the synthetic route of building block **A**. And ^{1}H NMR spectrum of freshly prepared 3 mM **A** dissolved in CD_3OD (A) or D_2O, tested at 298 K and 600 MHz. (B). (C) Mass spectrum of **A**, m/z calculated $[M\text{-}H]^-$ = 184.9736, m/z found: 184.9724. From original publication I.

The synthesis DCMs of $\mathbf{A}_n$ was tested by dissolving 36 mM **A** in the phosphate buffer at pH 7.4, and letting it undergo air oxidation until equilibrium, where the HPLC spectrum of the sample showed no trace of free thiol and no longer changed with time. HPLC-MS analysis to the equilibrated DCL suggested a major conversion of **A** to $\mathbf{A}_3$, $\mathbf{A}_4$ and $\mathbf{A}_7$-$\mathbf{A}_{11}$, accompanied with a minor conversion to $\mathbf{A}_5$ and $\mathbf{A}_6$ (**Figure 17**A-F).

And the dynamicity of the chemical structure of $\mathbf{A}_n$ was simply tested by diluting the 36 mM equilibrated $\mathbf{A}_n$ DCL (36**A**) to a 3 mM $\mathbf{A}_n$ DCL (3**A**), and allow it to equilibrate. The conversion of **A** to different $\mathbf{A}_n$ species in each equilibrated DCL was compared by the HPLC-MS analysis (**Figure 17**A). It turned out that 3**A** had much less conversion to $\mathbf{A}_7$-$\mathbf{A}_{11}$ than 36**A**, confirming the restructuring of $\mathbf{A}_n$ via disulfide interchange upon the altered $\mathbf{A}_n$ concentration. Thus the chemical structure of $\mathbf{A}_n$ is dynamic regardless of the prescence of free thiol.

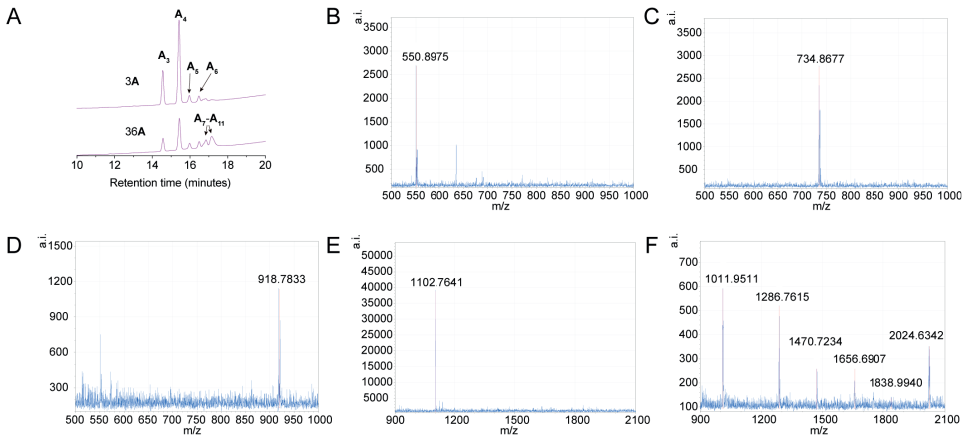

Figure 17 (A) HPLC-MS analysis of the DCLs equilibrated from 36 mM **A** (36**A**) and 3 mM **A** (3**A**). Mass spectrum correlated to the HPLC-MS analysis: (B) 1st peak, trimer ($\mathbf{A}_3$), retention time 14.5 min, m/z calculated: $[M-H]^-$ = 550.8885, m/z found: 550.8975. (C) 2nd peak, retention time 15.5 min, tetramer ($\mathbf{A}_4$), m/z calculated $[M-H]^-$ = 734.8538, m/z found: 734.8677. (D) 3rd peak, retention time 16.0 min, pentamer ($\mathbf{A}_5$), m/z calculated $[M-H]^-$ = 918.8191, m/z found: 918.7833. (E) 4th peak, retention time 16.5 min, hexamer ($\mathbf{A}_6$), m/z calculated $[M-H]^-$ = 1102.7844, m/z found: 1102.7641. (F) Merged 6th and 7th peak, retention time 16.8 min-17.2 min, heptamer ($\mathbf{A}_7$), m/z calculated $[M-H]^-$ = 1286.7496, m/z found: 1286.7615. Octamer ($\mathbf{A}_8$), m/z calculated $[M-H]^-$ = 1470.7149, m/z found: 1470.7234. Nonamer ($\mathbf{A}_9$), m/z calculated $[M-H]^-$ = 1656.6802, m/z found: 1656.6907. Ten-membered macrocycle ($\mathbf{A}_{10}$), m/z calculated $[M-H]^-$ = 1838.6454, m/z found: 1838.9940. Eleven-membered macrocycle ($\mathbf{A}_{11}$), m/z calculated $[M-H]^-$ = 2024.6107, $[M-2H]^{2-}$ = 1011.8017. m/z found: 2024.6342, 1011.9511. From original publication I.

To verify the significance of the structural adaptability of the DCMs during self-assembly with the polymeric template, small molecules with fixed chemical structures analogous to $\mathbf{A}_n$ were also employed to interact with the polymeric templates. These small molecules include commercially available non-cyclic benzoic acid (**BA**, BLD Pharma), perylene-3,4,9,10-tetracarboxylic acid (**PTA**, BLD Pharma), and a static azobenzene-derived macrocyclic disulfide (**ADM**).

ADM was synthesized following a previous report (**Figure 18**A). Briefly, 4-nitrobenzoic acid (>99%, TCI) underwent reductive coupling with glucose (>95%, TCI) to yield 4,4′-(diazene-1,2-diyl)dibenzoic acid. Then, (2S,2'S)-2,2'-((4,4'-((E)-Diazene-1,2-diyl)bis(benzoyl))bis(azanediyl))bis(3-mercaptopropanoic acid) (**B**) was synthesized through esterification between 4,4′-(diazene-1,2-diyl)dibenzoic acid and *L*-cysteine. Finally, **B** was oxidized in air until equilibrium was reached to obtain **ADM**. The chemical structure of ADM was confirmed by ^{1}H NMR and ^{1}H-^{13}C heteronuclear single quantum coherence spectroscopy (HSQC) (**Figure 18**B and C).

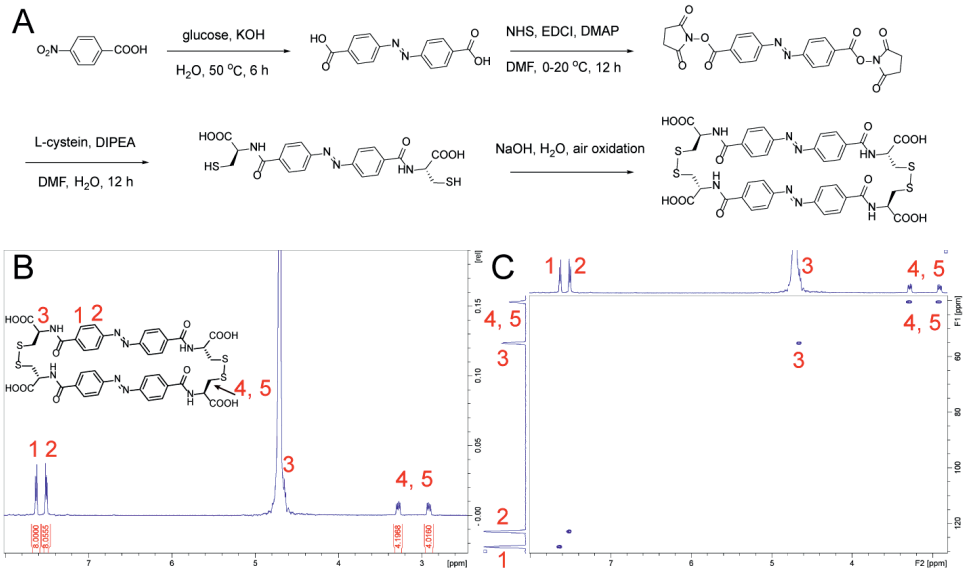

Figure 18 (A) Scheme of the synthesis of **ADM**. The pH at the final oxidation stage was 10. (B) ^{1}H NMR spectrum and (C) ^{1}H-^{13}C HSQC plot of the as-synthesized **ADM** dissolved in D_2O at pH 10. NMR spectroscopy was operated at 298 K and 500/125 MHz for $^{1}H/^{13}C$. From original publication II.

The disulfide bond in **ADM** is more stable than that in $\mathbf{A}_n$, making it resistant to disulfide interchange when dissolved in phosphate buffer at pH 7.4, as there was no observable difference between the HPLC spectra of the as-synthesized **ADM** and **ADM** dissolved by phosphate buffer for 1 year at least. Moreover, to verify if the chemical structure of **ADM** was stable upon self-assembly, 10 mM **ADM** was interacted with 40 mM of a small molecular surfactant cetyltrimethylammonium bromide (**CTAB**, Sigma-Aldrich) at pH 10 to fully neutralize each other's polarity and initiate hydrophobic-effect-mediated self-assembly process, during which the AFM image and HPLC spectra of the sample were monitored in parallel to investigate if any self-assembly process affected the chemical structural alteration of **ADM**.

AFM images at 5 minutes and 15 minutes after sample preparation were taken and suggested a stepwise self-assembly from nanosheet to droplets (**Figure 19**A and B). 5 minutes after the sample being prepared, there were nanosheets and neonatant droplets stacked from the nanosheets (**Figure 19**A). Reaching 15 minutes, the droplets grew bigger and in much regular sphere form (**Figure 19**B). Finally, those droplets further assembled together and sequestered out from the solution to form a bulk material after overnight incubation. The amplitude sweep rheometry to the material presented a linear viscoelastic region where the loss modulus (G'') was larger than the strorage modulus (G'), indicating a liquid-form material was formed

during a liquid-liquid phase separation process induced by the self-assembly (**Figure 19**C). Throughout the whole process, in order to monitor the possible chemical change of **ADM** by HPLC analysis, the self-assembly was collected by centrifugation and redissloved by CH_3OH containing 0.1% TFA for HPLC sample preparation and measurement. It turned out that all the HPLC spectra were the same as the as-synthesized **ADM**, confirming the no disulfide-interchange of **ADM** upon self-assembly (**Figure 19**D).

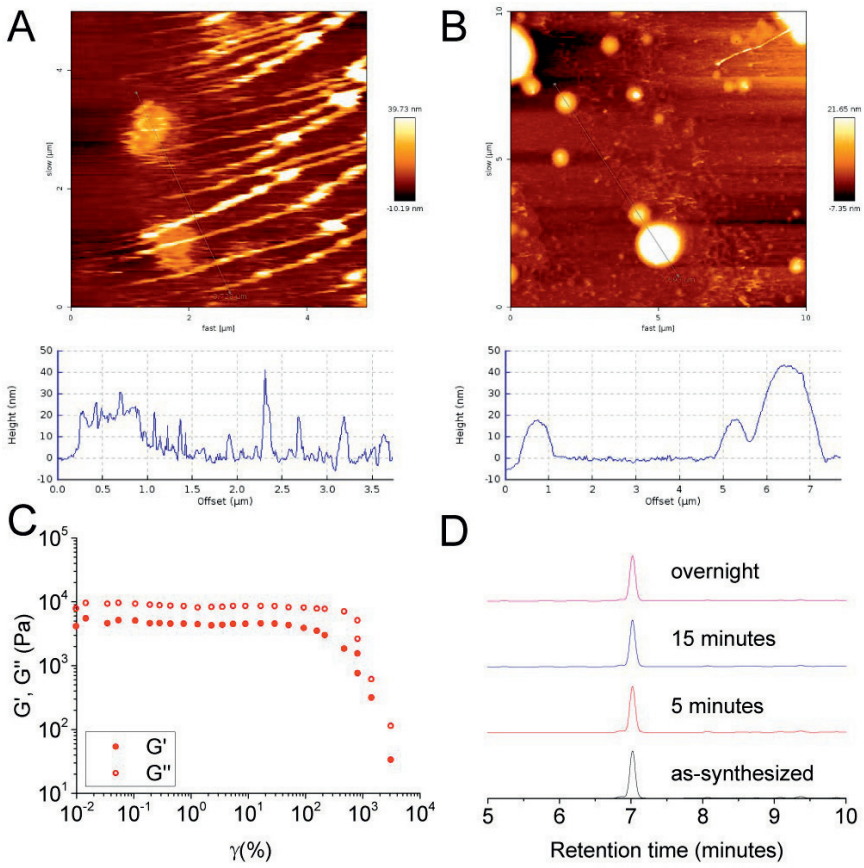

Figure 19 Contact-mode AFM images and measured height profiles of the self-assembly between **ADM** and **CTAB** acquired at 5 minutes (A) and 15 minutes (B) after sample preparation. (C) Amplitude sweep rheometry of the bulk material formed by the LLPS process of the self-assembly between **ADM** and **CTAB**. (D) HPLC analysis to the as-synthesized **ADM** and self-assembly between **ADM** and **CTAB** at different time points after sample preparation. From original publication II.

3.1.3 Distinctive folding of polymeric template and synthetic outcome of DCMs at the equilibrium

To determine whether the polymeric template $\mathbf{PT}_{703}$ binds with and folds due to the DCMs of $\mathbf{A}_n$, we examined a DCL equilibrated from 3 mM **A** and 15 mM $\mathbf{PT}_{703}$, designated as 3**A**-15$\mathbf{PT}_{703}$. The analysis involved measuring the hydrodynamic radius (R_h), radius of gyration (R_g), transverse NMR relaxation time (T_2), and conducting transmission electron microscopy (TEM). The initial concentrations of **A** and $\mathbf{PT}_{703}$ were selected for two reasons: (1) High enough concentration to provide adequate signal-to-noise (S/N) ratio from all protons for NMR detection. (2) Cationic pendants from $\mathbf{PT}_{703}$ were in 5-times excess to the anionic **A** for maintaining inter-polymer electrostatic repulsion. Thereby the hydrophobic effect upon charge neutralization between **A** and $\mathbf{PT}_{703}$ was expected to drive folding rather than inter-polymer aggregation.

First, diffusion-ordered spectroscopy (DOSY) and dynamic light scattering (DLS) were utilized to confirm the self-assembly and measure the R_h within the DCL (**Figure 20**). In the DOSY two-dimensional (2D) plot, the ^{1}H-NMR signals from both $\mathbf{A}_n$ and $\mathbf{PT}_{703}$ were broadened and aligned at the same diffusion coefficient (D), indicating their nearly quantitative self-assembly (**Figure 20**A). The diffusion coefficient of the supramolecular assembly was larger than that of 15 mM $\mathbf{PT}_{703}$ (15$\mathbf{PT}_{703}$) alone. By converting D to R_h using the Stokes-Einstein equation, we observed a decrease in R_h from approximately 6.86 nm for 15$\mathbf{PT}_{703}$ to about 4.67 nm for 3**A**-15$\mathbf{PT}_{703}$, suggesting that the polymer had folded. Dynamic light scattering (DLS) analysis also showed a decrease in the number-averaged R_h from 8.10 nm to 6.31 nm when $\mathbf{PT}_{703}$ was folded by $\mathbf{A}_n$, which is in good agreement with the DOSY results (**Figure 20**B and C).

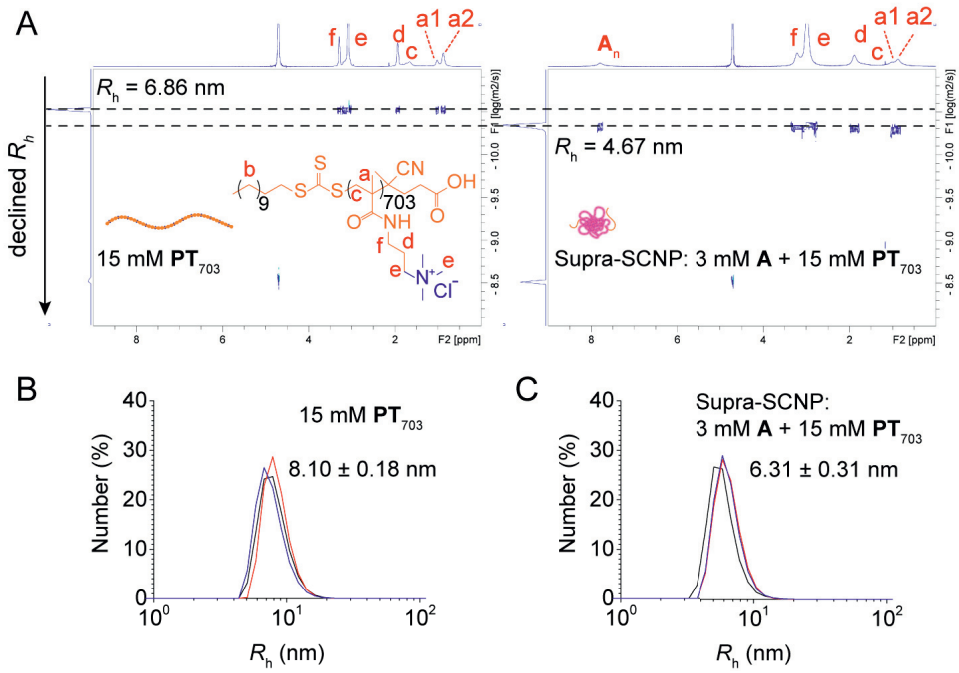

Figure 20 (A) DOSY 2D plot of the 15 mM polymeric template **PT**$_{703}$ alone (left), and DCL equilibrated from 3 mM **A** mixing with 15 mM **PT**$_{703}$ (right). NMR spectroscopy was operated at 298 K and 600 MHz. In parallel, DLS analysis showed the number averaged distribution of R_h of 15 mM **PT**$_{703}$ (B), and the DCL equilibrated from mixing 3 mM **A** mixing with 15 mM **PT**$_{703}$ (C). From original publication I.

Moreover, if folding occurs, both the R_g and T_2 of the polymer should decrease. A smaller R_g indicates a reduced root mean square distance from the monomers to the polymer's center of mass, while a shorter T_2 suggests a more compact microenvironment around the molecule[127-130]. Indeed, **PT**$_{703}$ exhibited significantly smaller R_g and shorter T_2 in the 3**A**-15**PT**$_{703}$ library compared to **PT**$_{703}$ alone (**Figure 21**A-C), confirming that the polymer was folded by **A**$_n$.

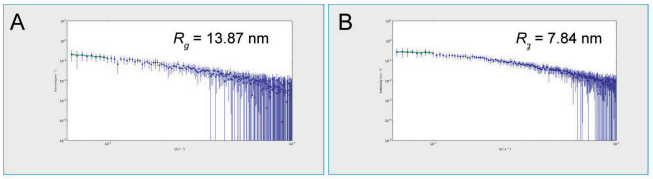

C

T_2/ms	A_3 H_1	A_4 H_1	A_5-A_{11} H_1	H_d	H_e	H_f	H_{a1}	H_{a2}
15**PT**$_{703}$				35	149	54	14	12
3**A**-15**PT**$_{703}$	6			12	26	17	8	7
3**A**-15**PT**$_{703}$ with 30% CD_3CN	89	42	37	12	79	25	8	8
3**A**	4148	1010	622					

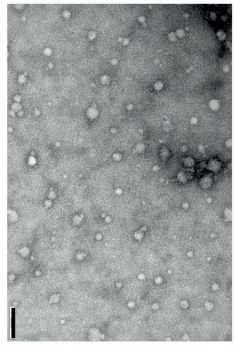

Figure 21 SAXS profile and Guinier fitting for determining the R_g of 15 mM **PT**$_{703}$ (A) and DCL equilibrated from mixing 3 mM **A** mixing with 15 mM **PT**$_{703}$ (B). (C) T_2 of the characteristic protons in different DCLs, measured at 600 MHz, 298 K. (D) TEM image of the DCL equilibrated from mixing 3 mM **A** mixing with 15 mM **PT**$_{703}$, scale bar = 100 nm. From original publication I.

Finally, TEM revealed that the Supra-SCNPs formed from 3**A**-15**PT**$_{703}$ appeared as compact globules with an average radius of approximately 7.5 nm (**Figure 21**D), consistent with the sizes determined from R_h and R_g measurements. Collectively, these results confirm that the polymer **PT**$_{703}$ was successfully folded into Supra-SCNPs by **A**$_n$ synthesized from the 3**A**-15**PT**$_{703}$ DCL.

In stark contrast, the library equilibrated from 3 mM **A** and 15 mM **ST**, designated as 3**A**-15**ST**, did not exhibit any observable self-assembly between **ST** and **A**$_n$. In the DOSY 2D plot of this library, the ^{1}H-NMR signals of **ST** and **A**$_n$ did not align in the diffusion dimension and showed diffusion constants similar to their respective control samples containing only 15 mM **ST** (15**ST**) or 3 mM **A**$_n$ (3**A**) (**Figure 22**). This indicates that there was insufficient interaction between **ST** and **A**$_n$ to observably alter their diffusion constants.

Since there was no observable self-assembly in the 3**A**-15**ST** DCL to alter the chemical environment around **A**$_n$, no significant difference was observed in the product distribution of **A**$_n$ compared to the control sample 3**A**. In contrast, in the DCL of 3**A**-15**PT**$_{703}$, where folding occurred, the production of **A**$_4$ was suppressed while the production of **A**$_7$-**A**$_{11}$ was enhanced. This unique template effect in the 3**A**-15**PT**$_{703}$ DCL suggests a possible structural adaptation of **A**$_n$ to the chemical environments emerging from the folding process.

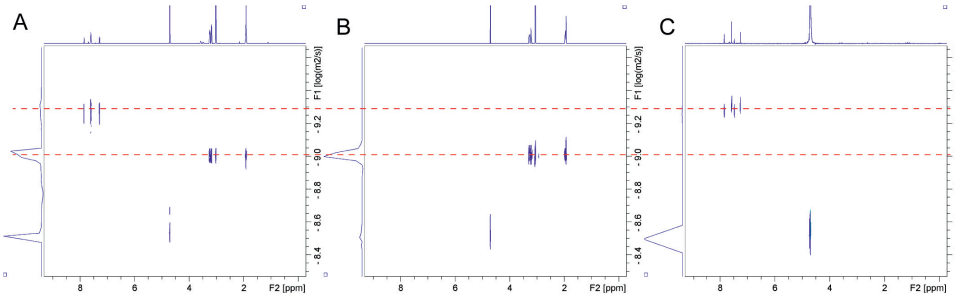

Figure 22 DOSY 2D plots of the samples (A) DCL equilibrated from 15 mM **ST** and 3 mM **A**, (B) 15 mM **ST**, and (C) 3 mM **A**, measured at 298 K, 500 MHz. From original publication I.

3.1.4 Different chemical environments around the DCMs in the folded polymeric template

To elucidate the adaptation mechanism of DCMs to the conformational dynamics during the folding process of the polymeric template, it is essential first to differentiate the chemical environments surrounding each DCM species in the folded state at equilibrium.

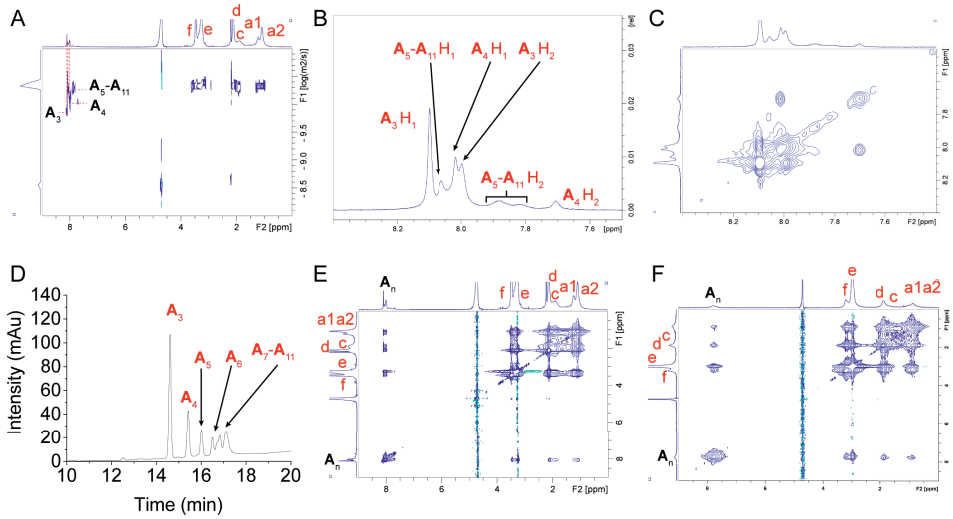

Figure 23 (A) DOSY 2D plot, (B) partial 1H NMR spectrum, (C) ^{1}H-^{1}H TOCSY 2D plot, (D) HPLC spectrum and (E) ^{1}H-^{1}H NOESY 2D plot of the Supra-SCNP (equilibrated from 15 mM **PT**$_{703}$ and 3 mM **A**) swollen by 30% CD_3CN in volume ratio. (F) of the native Supra-SCNP (equilibrated from 15 mM **PT**$_{703}$ and 3 mM **A**). From original publication I. NMR in this Figure are measured at 298K, 600 MHz.

As previously mentioned, relaxation measurement in NMR spectroscopy is a quintessential method for distinguishing chemical environments by non-invasively measuring the rotational motion of molecules. Typically, faster relaxation featured by shorter T_2 indicates a more compact chemical environment or stronger intermolecular associations affecting the molecule. Therefore, if a particular species within the non-covalent crosslinkers of $\mathbf{A}_n$ induces $\mathbf{PT}_{703}$ to adopt a more compact conformation, the T_2 of that $\mathbf{A}_n$ species would be shorter. By measuring the T_2 of each $\mathbf{A}_n$ species, we can determine the specific conformational chemical environments within the folded polymer where they reside.

However, upon folding in the 3**A**-15$\mathbf{PT}_{703}$ DCL, the proton signals from all DCMs species of $\mathbf{A}_n$ coalesced, making it impossible to differentiate their chemical environments. This coalescence could be attributed to the complex chemical environments within the highly compact folded polymer being too similar to distinguish. To enhance the differences in chemical environments and gain clearer insights, we applied a swelling method to partially open the compact folding without fully disrupting it. Considering that the folding is driven by hydrophobic effects among non-polar complexes, we introduced CD_3CN, which has lower polarity than D_2O and higher affinity for the non-polar folding regions. By adding CD_3CN at a 30% volume content, we swelled the Supra-SCNPs in the 3**A**-15$\mathbf{PT}_{703}$ DCL.

This swelling approach, corroborated by DOSY (**Figure 23**A), ^{1}H NMR spectrum (**Figure 23**B), proton–proton total correlation spectroscopy (^{1}H-^{1}H TOCSY, **Figure 23**C), and HPLC analyses (**Figure 23**D), allowed for precise assignment of the H_1 and H_2 signals for $\mathbf{A}_3$, $\mathbf{A}_4$, and the coalesced $\mathbf{A}_5$-$\mathbf{A}_{11}$ species. Importantly, the supramolecular integrity of the Supra-SCNPs was preserved after swelling, as evidenced by the T_2 values of $\mathbf{A}_n$ and $\mathbf{PT}_{703}$ (**Figure 21**C) and the similar nuclear Overhauser effect (NOE) correlations between the swollen and native samples in the ^{1}H-^{1}H NOE spectroscopy (NOESY) 2D plots (**Figure 23**E and F).

With the ability to differentiate the chemical environments using NMR, we proceeded to measure the T_2 of H_1 in the separated $\mathbf{A}_n$ species. The T_2 values decreased sequentially from $\mathbf{A}_3$ to $\mathbf{A}_4$ to the coalesced $\mathbf{A}_5$-$\mathbf{A}_{11}$ (**Figure 21**C). This trend suggests that their molecular motions are increasingly restricted within more compact chemical environments—that is, they are surrounded by chain conformations with higher degrees of folding. The DOSY experiments further confirmed this conclusion, as $\mathbf{A}_3$, $\mathbf{A}_4$, and the coalesced $\mathbf{A}_5$-$\mathbf{A}_{11}$ exhibited sequentially decreased diffusion coefficients, correlating with their increasingly restricted motions (**Figure 23**A).

Additionally, H_1 of $\mathbf{A}_3$ and $\mathbf{A}_4$ showed clear NOE correlations with the proton signal of H_2O, whereas the coalesced $\mathbf{A}_5$-$\mathbf{A}_{11}$ did not (**Figure 24**). Given their differing chemical environments and varying degrees of compactness corresponding to different folding stages, we conclude that $\mathbf{A}_3$ and $\mathbf{A}_4$ are located in the sparsely

folded hydrophilic shell of the Supra-SCNP, where they are better associated with the solvent. In contrast, $\mathbf{A}_5$-$\mathbf{A}_{11}$ are situated in the compactly folded hydrophobic core of the Supra-SCNP, away from the solvent.

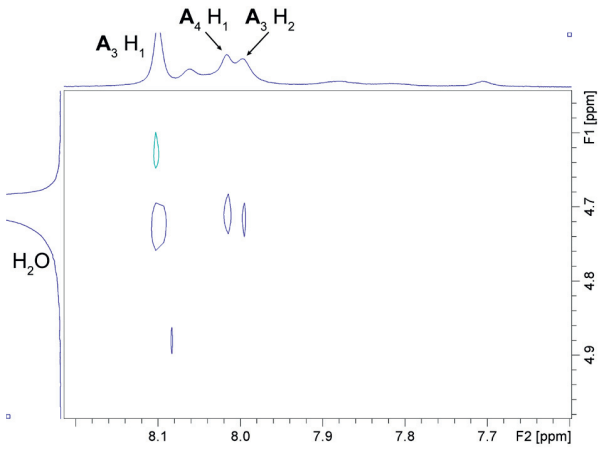

Figure 24 ^{1}H-1H NOESY 2D plot of the swollen Supra-SCNP (equilibrated from 15 mM $\mathbf{PT}_{703}$ and 3 mM **A**) in the solvent system where 30% volume of the deuterated phosphate buffer at pD 7.4 was replaced by CD_3CN, measured at 298 K, 600 MHz. From original publication I.

3.1.5 The adaptation mechanism of the DCMs in different conformational chemical environments

Observing that $\mathbf{A}_n$ species with larger ring sizes (higher n) exhibited shorter T_2, we hypothesized that the more compact conformational chemical environment increases the local effective concentration of $\mathbf{A}_n$. Guided by Le Chatelier's principle—which states that an equilibrium system adjusts to minimize changes in concentration—we proposed that $\mathbf{A}_n$ counteracts this increase in local concentration by decreasing the number of DCMs through restructuring into larger macrocycles.

To verify the hypothesis that higher concentrations of $\mathbf{A}_n$ promote the production of species with larger n, we prepared a series of DCLs with gradually increasing concentrations of $\mathbf{A}_n$ ranging from 0.30 mM to 36 mM (referred to as *x***A** DCLs). These DCLs were equilibrated and analyzed using HPLC-MS (**Figure 25**A). Indeed, as the overall concentration of $\mathbf{A}_n$ increased, the production of larger $\mathbf{A}_n$ species (n = 7–11) was enhanced, accompanied by a decrease in smaller $\mathbf{A}_n$ species (n = 3 and 4). Notably, the production of $\mathbf{A}_5$ and $\mathbf{A}_6$ remained relatively insensitive to changes in $\mathbf{A}_n$ concentration. This result showed how DCLs of $\mathbf{A}_n$ responded to concentration changes under the Le Chatelier's principle. Therefore, if the

production profile of $\mathbf{A}_n$ under increased folding degrees mirrors that of the *x***A** DCLs, we can conclude that the adaptation of $\mathbf{A}_n$'s production to the conformational chemical environments follows Le Chatelier's principle.

Next, we increased the folding degree by altering the stoichiometric ratio between $\mathbf{A}_n$ and $\mathbf{PT}_{703}$. Specifically, we prepared a series of DCLs with a fixed $\mathbf{PT}_{703}$ concentration of 15 mM and increasing $\mathbf{A}_n$ concentrations from 0.30 mM to 7.5 mM (designated as *x***A**-15$\mathbf{PT}_{703}$). The folding degree of these DCLs was characterized by the R_h obtained from DLS and DOSY analyses, as well as the T_2 measured by NMR (**Figure 25**B). The production distribution of $\mathbf{A}_n$ species in each DCL was determined by HPLC-MS analysis (**Figure 25**C). As the concentration of $\mathbf{A}_n$ increased, both R_h and T_2 decreased, indicating an enhanced folding degree. Correspondingly, similar to the observations in the *x***A** DCLs, the production of $\mathbf{A}_3$ and $\mathbf{A}_4$ decreased, enhancing the production of $\mathbf{A}_5$-$\mathbf{A}_{11}$, while $\mathbf{A}_5$ and $\mathbf{A}_6$ remained relatively unaffected by changes in the folding degree. This finding supports the notion that the DCMs dynamically adapt to their folding environment by counterbalancing the increased local effective concentration resulting from folding, in alignment with Le Chatelier's principle.

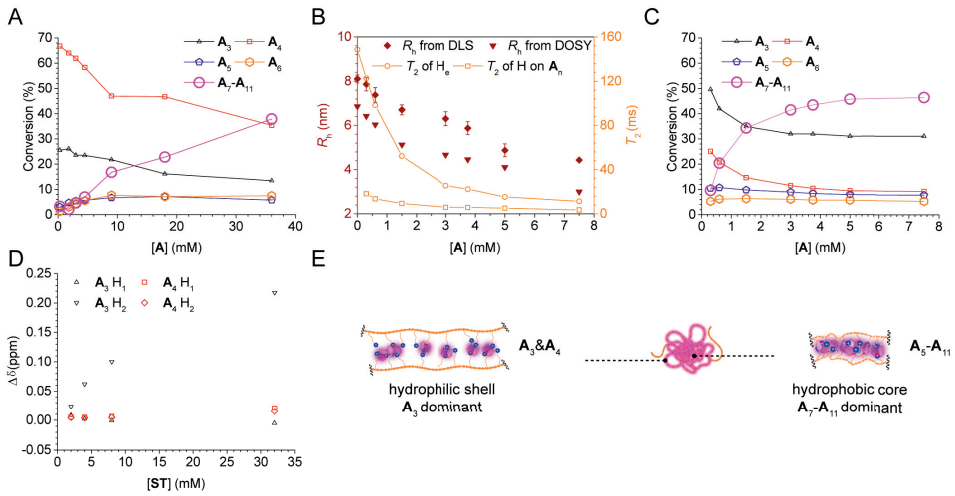

Figure 25 (A) The product distribution of the *x***A** DCLs that equilibrated from *x* mM of **A**. The product distributions were expressed by conversion of **A** to a specified $\mathbf{A}_n$ species, determined by HPLC analysis. (B) The folding degree of the *x***A**-15$\mathbf{PT}_{703}$ DCLs that equilibrated from *x* mM of **A** and 15 mM of $\mathbf{PT}_{703}$. The folding degrees were expressed by R_h determined by DLS and DOSY analysis, and T_2 measured by NMR at 298 K, 600 MHz. (C) The product distribution of the *x***A**-15$\mathbf{PT}_{703}$ DCLs that equilibrated from *x* mM of **A** and 15 mM of $\mathbf{PT}_{703}$, determined by HPLC. (D) The ^{1}H NMR chemical shift of $\mathbf{A}_3$ and $\mathbf{A}_4$ in the 2**A**-*y***ST** DCLs, equilibrated from 2 mM **A** and *y* mM (2, 4, 8, 32) **ST**, measured at 298 k, 600 MHz. (E) Proposed residing chemical environments for different $\mathbf{A}_n$ species. From original publication I.

However, Le Chatelier's principle alone could not fully explain the adaptation observed in the shell of the Supra-SCNPs. Contrary to the control DCLs, the Supra-SCNPs consistently showed a higher conversion to $\mathbf{A}_3$ compared to $\mathbf{A}_4$.

We hypothesized that the amplification of A_3 is due to two primary factors: (1) the sparse and solvated conformational chemical environment in the outer shell, resembling that of its small-molecule counterpart **ST**; and (2) the higher affinity of $\mathbf{A}_3$ for **ST** compared to $\mathbf{A}_4$.

To validate this, we assessed the affinities of $\mathbf{A}_3$ and $\mathbf{A}_4$ for **ST** via ^{1}H NMR titration (**Figure 25**D). We prepared a DCL array by fixing the concentration of **A** at 2.00 mM and incrementally increasing the concentration of **ST** from 2 mM to 32 mM. The resulting chemical shift changes ($\Delta\delta$, ppm) for $\mathbf{A}_3$—specifically, downfield and upfield shifts for H_2 and H_1, respectively—implied a heightened affinity for **ST**. In contrast, negligible shifts were observed for $\mathbf{A}_4$ across all DCL configurations. This result explains the preferential amplification of $\mathbf{A}_3$ within the Supra-SCNP's shell. Nevertheless, the NMR signals of $\mathbf{A}_3$ and **ST** are most from their individual solvated states rather than a stable assembly, as evidenced by the absence of nuclear significant alterations in *D* for each component (**Figure 22**). This suggests a weak interaction with rapid exchange kinetics between the bound and unbound states.

In conclusion, the adaptation of $\mathbf{A}_n$'s chemical structure within the conformational chemical environments of the folded polymeric template follows Le Chatelier's principle. Additionally, in the loosely folded chain regime, the adaptation is also influenced by the binding affinity to individual template monomers. Consequently, $\mathbf{A}_3$ and $\mathbf{A}_4$ are located in the solvated shell, with $\mathbf{A}_3$ being predominant, while $\mathbf{A}_5$-$\mathbf{A}_{11}$ reside in the hydrophobic core, dominated by $\mathbf{A}_7$-$\mathbf{A}_{11}$ (**Figure 25**E).

3.1.6 Comparision between DCMs and analogous static non-covalent crosslinkers for folding the polymer

To confirm the significance of structural adaptability in non-covalent crosslinkers, we characterized the folding degree of $\mathbf{PT}_{703}$ after its interaction with acyclic and macrocyclic analogous non-covalent crosslinkers with fixed chemical structures. The acyclic molecules used were benzoic acid (**BA**) and perylene-3,4,9,10-tetracarboxylic acid (**PTA**), which share the same crosslinking motif as $\mathbf{A}_n$ but have elementary motif valences. The cyclic molecule was an azobenzene-derived macrocyclic disulfide (**ADM**), whose disulfide bond is too inert to undergo disulfide interchange in this solvent system. Typically, 3 mM of each analogous crosslinker (based on their carboxylate groups) was interacted with 15 mM $\mathbf{PT}_{703}$, and the samples were designated as 3**BA**-15$\mathbf{PT}_{703}$, 3**PTA**-15$\mathbf{PT}_{703}$ and 3**ADM**-15$\mathbf{PT}_{703}$,

respectively. Corresponding control samples containing only 3 mM of each non-covalent crosslinker—3**BA**, 3**PTA** and 3**ADM**—were prepared for comparison. Using a 500 MHz NMR spectrometer equipped with a non-cryoprobe, we applied ^{1}H NMR, ^{1}H DOSY, ^{1}H-^{1}H NOESY, and T_2 measurements to the equilibrated samples to probe the binding of the analogous non-covalent crosslinkers to **PT**$_{703}$ and assess the subsequent folding of **PT**$_{703}$.

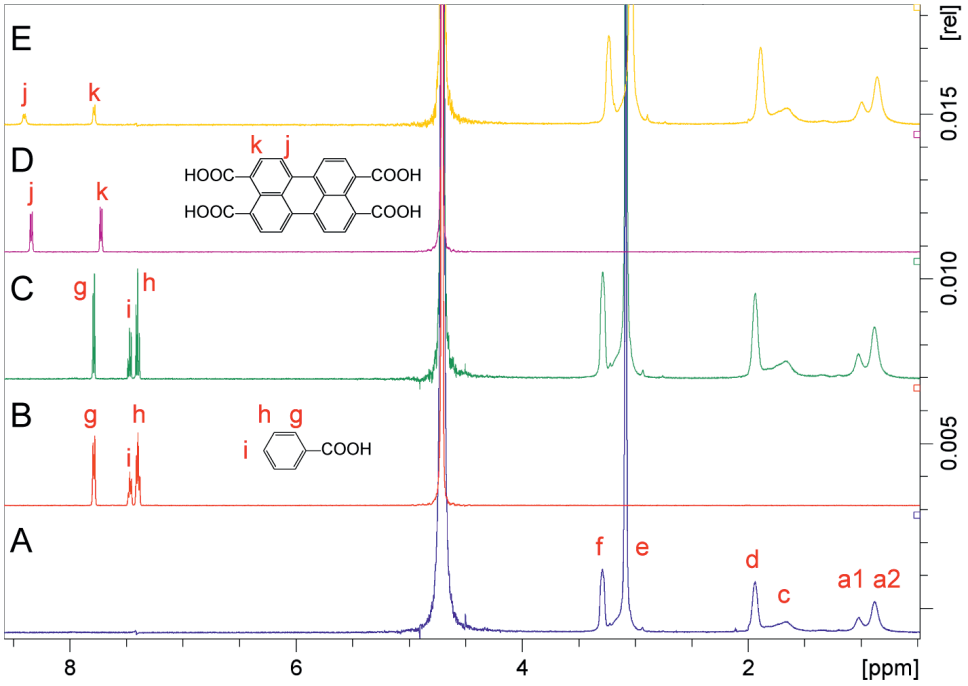

Figure 26 ^{1}H NMR spectra and peak assignment to the samples of (A) 15 mM **PT**$_{703}$, (B) 3 mM **BA**, (C) 15 mM **PT**$_{703}$ mixed with 3 mM **BA**, (D) 0.75 mM **PTA**, (E) 15 mM **PT**$_{703}$ mixed with 0.75 mM **PTA**. Samples were all dissolved in deuterated phosphate buffer at pD 7.4, and measured at 298 K, 500 MHz. From original publication I.

First, the peaks from the spectrum were assigned (**Figure 26**). Then the DOSY results were analysed (**Figure 27**). The diffusion constants of all the non-covalent crosslinkers did not align with that of **PT**$_{703}$ in any of the samples, indicating significantly weaker binding to the polymer compared to the 3**A**-15**PT**$_{703}$ sample, where the diffusion constants were fully aligned. Moreover, **BA**, **PTA** and **ADM** exhibited progressively higher binding affinities to **PT**$_{703}$, as evidenced by increasingly decreased D values compared to their free forms when interacting with **PT**$_{703}$, and by more pronounced NOE signals with **PT**$_{703}$. This suggests that **BA**, **PTA** and **ADM**, and dynamic **A**$_n$ have progressively higher binding affinities to

PT$_{703}$, implying that higher valency of binding motifs, macrocyclic configuration, and adaptive chemical structures can additively enhance the binding affinity of non-covalent crosslinkers to the polymer. Notably, the adaptive chemical structure addresses all these factors simultaneously.

As the binding affinity of the non-covalent crosslinkers to the polymer increased, they induced the polymer to fold into a more compact state. This was evidenced by progressively lower *D* values observed in the 3**BA**-15**PT**$_{703}$, 3**PTA**-15**PT**$_{703}$, 3**ADM**-15**PT**$_{703}$ and 3**A**-15**PT**$_{703}$ samples, indicating increasingly compact folding states.

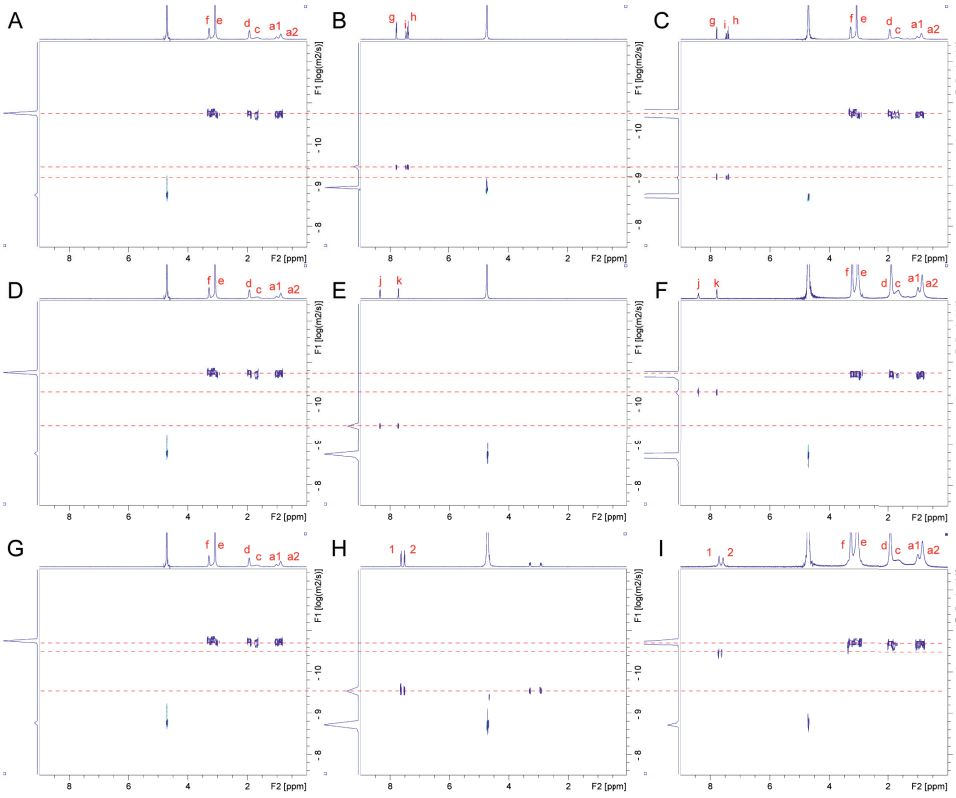

Figure 27 DOSY 2D plot for the samples of (A, D and G) 15 mM **PT**$_{703}$, (B) 3 mM **BA**, (C) 15 mM **PT**$_{703}$ mixed with 3 mM **BA**, (E) 0.75 mM **PTA**, (F) 15 mM **PT**$_{703}$ mixed with 0.75 mM **PTA**. (H) 0.75 mM **ADM**, (I) 15 mM **PT**$_{703}$ mixed with 0.75 mM **ADM**. Samples were all dissolved in deuterated phosphate buffer at pD 7.4, and measured at 298 K, 500 MHz. From original publication I.

In conclusion, the adaptive chemical structure is critical for achieving optimized binding affinity and folding efficiency of non-covalent crosslinkers to the parent polymer.

3.1.7 The effect of synthetic kinetics of DCMs upon folding kinetics of polymeric template

3.1.7.1 Synchronized synthetic and folding kinetics in two stages

Having clarified how the conformational chemical environment affects the synthesis of $\mathbf{A}_n$ at equilibrium, we proceeded to investigate the interaction between the synthetic kinetics of DCMs and the folding kinetics of the polymeric template.

In the 3**A**-15$\mathbf{PT}_{703}$ DCL, we simultaneously observed the folding and synthetic kinetics using DOSY and HPLC-MS from the initial mixing of fresh **A** and $\mathbf{PT}_{703}$ until equilibrium was reached (**Figure 28**A).

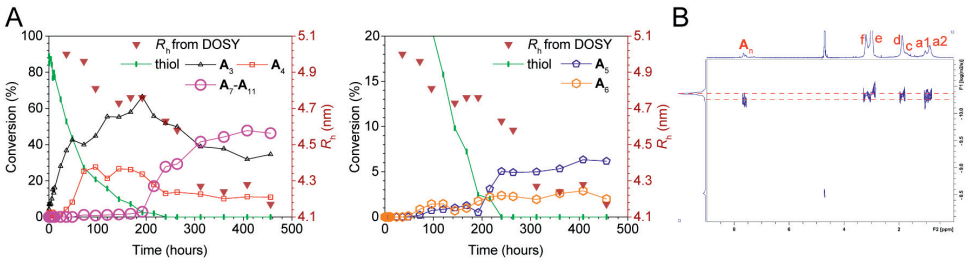

Figure 28 (A) Kinetic monitoring of the DCL equilibrated from mixing 15 mM $\mathbf{PT}_{703}$ and 3 mM **A** (3**A**-15$\mathbf{PT}_{703}$). Product distribution expressed as conversion of **A** to different $\mathbf{A}_n$ species was determined by HPLC analysis. Folding degree was measured by R_h determined from DOSY analysis. (B) The DOSY 2D plot of the 3**A**-15$\mathbf{PT}_{703}$ DCL at the beginning of the oxidation, measured at 298 K, 600 MHz. From original publication I.

We found that the synthetic and folding kinetics were interactive from the outset. At the first monitoring point in the DOSY experiment, $\mathbf{A}_n$ already shared a common diffusion constant with $\mathbf{PT}_{703}$, indicating immediate association (**Figure 28**B). The entire kinetic monitoring revealed a two-stage synchronization between the synthetic and folding processes. In the first 200 hours, **A** was gradually oxidized into $\mathbf{A}_3$ and $\mathbf{A}_4$, reaching a plateau, while the folding progressed in parallel, causing a slight decrease in the R_h of the Supra-SCNPs to a plateau. Thereafter, upon the exhaustion of free thiol groups, $\mathbf{A}_3$ and $\mathbf{A}_4$ were consumed to promote the production of larger macrocycles $\mathbf{A}_5$-$\mathbf{A}_{11}$, particularly showing a sigmoidal increase of $\mathbf{A}_7$-$\mathbf{A}_{11}$. Concurrently, the folding progressed dramatically, with the R_h decreasing to its final equilibrium value.

3.1.7.2 The first kinetic stage

The first kinetic stage was dominated by thiol oxidation and thiol–disulfide exchange reactions. A key phenomenon during this stage was the predominant transformation of larger DCMs ($\mathbf{A}_5$-$\mathbf{A}_{11}$) back into a smaller one ($\mathbf{A}_3$) through thiol–disulfide exchange.

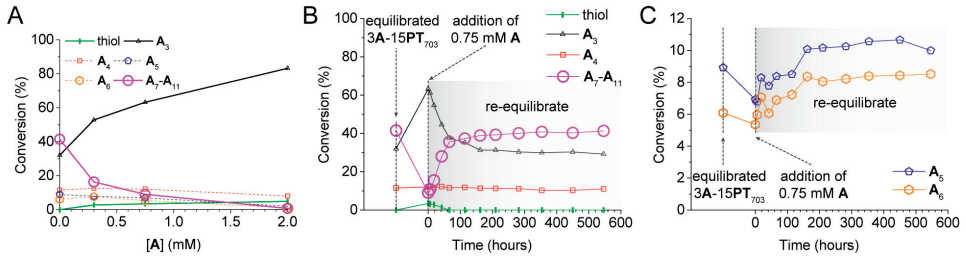

Figure 29 (A) The change on **A**'s conversion to different $\mathbf{A}_n$ species right after adding 0.30, 0.75 or 2.00 mM fresh **A** to the pre-equilibrated 3**A**-15$\mathbf{PT}_{703}$ DCL (3.00 mM **A** + 15.00 mM $\mathbf{PT}_{703}$), determined by HPLC analysis. (B) The kinetic monitoring by HPLC analysis on **A**'s conversion to different $\mathbf{A}_n$ species after adding 0.75 mM fresh **A** to the pre-equilibrated 3**A**-15$\mathbf{PT}_{703}$ DCL. From original publication I.

We validated this transformation by adding fresh **A** to a pre-equilibrated 3**A**-15$\mathbf{PT}_{703}$ DCL. Immediately after the addition, the conversion of **A** to $\mathbf{A}_5$-$\mathbf{A}_{11}$ decreased, leading to a transient increase in the formation of $\mathbf{A}_3$. This transient amplification of $\mathbf{A}_3$ on the consumption of $\mathbf{A}_5$-$\mathbf{A}_{11}$ was will be enhanced when higher amount of fresh **A** was added (**Figure 29**A). As **A** underwent oxidation, the transiently amplified $\mathbf{A}_3$ converted back to $\mathbf{A}_5$-$\mathbf{A}_{11}$ to re-establish equilibrium (**Figure 29**B). Additionally, when 3 mM of fully oxidized $\mathbf{A}_3$ or $\mathbf{A}_4$ was mixed with 15 mM $\mathbf{PT}_{703}$ in the absence of any free thiol groups, the libraries instantly reached the same $\mathbf{A}_n$ distribution and diffusion coefficient as the reference library equilibrated from fresh **A** and $\mathbf{PT}_{703}$, and remained unchanged thereafter, indicating that equilibrium was achieved (**Figure 30**).

These observations confirm that the presence of thiol groups and the thiol–disulfide exchange inhibit the production of larger macrocycles $\mathbf{A}_5$-$\mathbf{A}_{11}$ by transforming them back into smaller macrocycles like $\mathbf{A}_3$. Consequently, the folding kinetics are limited by the rate of thiol oxidation. In the absence of thiol groups, the transition from $\mathbf{A}_3$ and $\mathbf{A}_4$ to $\mathbf{A}_5$-$\mathbf{A}_{11}$ via disulfide interchange is rapid and closely follows the folding kinetics.

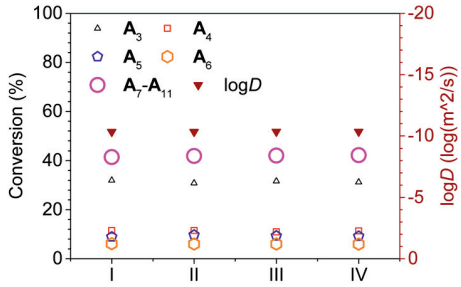

Figure 30 The conversion of **A** to different $\mathbf{A}_n$ species analysed by HPLC, and the corresponding Supra-SCNPs' diffusion coefficient (*D*) measured by DOSY of the 3**A**-15$\mathbf{PT}_{703}$ library prepared by equilibrating from mixing 3 mM fresh **A** and 15 mM $\mathbf{PT}_{703}$ (sample I), mixing 3 mM pure $\mathbf{A}_3$ with 15 mM $\mathbf{PT}_{703}$ (sample II), mixing 3 mM pure $\mathbf{A}_4$ with 15 mM $\mathbf{PT}_{703}$ (sample III), and mixing the mixture of 3 mM $\mathbf{A}_3$, $\mathbf{A}_4$ and $\mathbf{A}_5$-$\mathbf{A}_{11}$ with 15 mM $\mathbf{PT}_{703}$ (sample IV). NMR data were obtained at 298 K, 600 MHz. From original publication I.

3.1.7.3 The second kinetic stage

A significant feature of the second kinetic stage is the catalytic synchronization between DCC and folding, as indicated by the sigmoidal growth of larger macrocycles $\mathbf{A}_7$-$\mathbf{A}_{11}$ at the expense of smaller ones ($\mathbf{A}_3$ and $\mathbf{A}_4$), accompanied by a dramatic progression in folding.

To understand this catalytic synchronization, we consider the molecular dynamics of different $\mathbf{A}_n$ species and the varying rate-determining steps depending on the presence or absence of thiol groups. Based on ^{1}H-^{1}H NOESY and T_2 analysis, $\mathbf{A}_3$ and $\mathbf{A}_4$ accelerate conformational dynamics due to better association with the aqueous solvent, while larger macrocycles $\mathbf{A}_7$-$\mathbf{A}_{11}$ stabilize and mitigate conformational dynamics within the hydrophobic core of the folded polymer. Furthermore, when thiol groups are present, the kinetic rates of folding and synthesis are determined by the rate of thiol oxidation. In the absence of thiol groups, the rates of folding and synthesis are both rapid, allowing equilibrium to be reached quickly (**Figure 31**A).

The binding of $\mathbf{A}_n$ to $\mathbf{PT}_{703}$ introduces hydrophobic effects to drive the folding. As $\mathbf{A}_3$ and $\mathbf{A}_4$ had better association with the water molecule and stronger bound-state motion dynamics than $\mathbf{A}_5$-$\mathbf{A}_{11}$ (**Figure 24** and **Figure 21**C), they may use this outstanding amphiphilicity and dynamics to catalyse the conformational dynamics of $\mathbf{PT}_{703}$. Thus, as thiol groups are consumed by oxidation and more $\mathbf{A}_3$ and $\mathbf{A}_4$ are produced, this catalytic effect becomes increasingly pronounced, overcoming the inhibition from thiol–disulfide exchange and initiating the catalytic synchronization in the second stage. At the beginning of the second stage where the conversion to $\mathbf{A}_3$ and $\mathbf{A}_4$ was dominant, this catalysis should be at its peak perforemance. Subsequently, the increased folding degree promotes the conversion of $\mathbf{A}_3$ and $\mathbf{A}_4$ to

larger macrocycles $\mathbf{A}_5$-$\mathbf{A}_{11}$ (primarily $\mathbf{A}_7$-$\mathbf{A}_{11}$) under the governance of Le Chatelier's principle. The enhanced production of $\mathbf{A}_5$-$\mathbf{A}_{11}$ slows down both folding and synthesis by mitigating conformational dynamics and consuming $\mathbf{A}_3$ and $\mathbf{A}_4$, contributing to the deceleration observed in the sigmoidal growth.

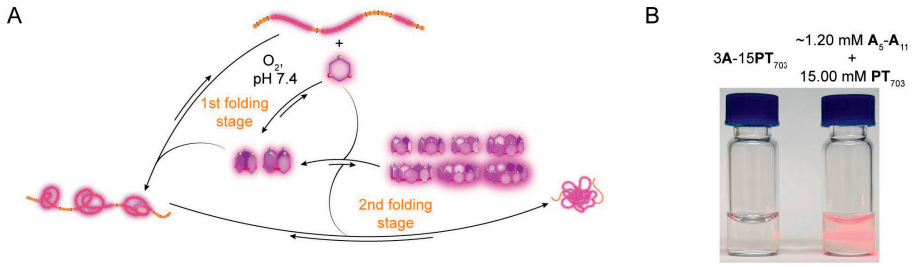

Figure 31 (A) The synchronization between the folding kinetics of the polymeric template $\mathbf{PT}_{703}$ and the synthetic of the DCMs $\mathbf{A}_n$ as non-covalent crosslinkers. The cationic pendants from $\mathbf{PT}_{703}$ were in excess amount compared to the anionic building block **A**. All the reaction in the scheme happened in phosphate buffer at pH 7.4, room temperature, and atmospheric pressure. (B) The Tyndall phenomenon test of the Supra-SCNP sample of 3**A**-15$\mathbf{PT}_{703}$, and the aggregated mixture resulted from adding ~1.20 mM of the ensemble of $\mathbf{A}_5$-$\mathbf{A}_{11}$ to 15.00 mM $\mathbf{PT}_{703}$. From original publication I.

Another important aspect of this catalytic synchronization is its critical dependence on the timing of product emergence, resembling the importance of timing for molecular chaperones and PTMs during biological peptide folding processes. We investigated this timing dependence by manually adjusting the initial $\mathbf{A}_n$ species interacting with $\mathbf{PT}_{703}$.

First, 1.2 mM of larger macrocycles $\mathbf{A}_5$-$\mathbf{A}_{11}$ were collected via preparative HPLC and mixed with 15 mM $\mathbf{PT}_{703}$. Contrary to the expected single-chain self-assembly, precipitation occurred (**Figure 31**B), likely due to interchain aggregation facilitated by the early presence of large macrocycles $\mathbf{A}_5$-$\mathbf{A}_{11}$, which have stronger intermolecular associations with the polymer due to their higher molecular weight. However, when $\mathbf{A}_3$ and $\mathbf{A}_4$ were included alongside the larger species $\mathbf{A}_5$-$\mathbf{A}_{11}$ and $\mathbf{PT}_{703}$, equilibrium at the single-chain level was reached instantly (**Figure 30**). Given that $\mathbf{A}_3$ and $\mathbf{A}_4$ reside in the hydrophilic shell of the Supra-SCNP and can catalyze rearrangement of the polymer conformation, we reasoned that $\mathbf{A}_3$ and $\mathbf{A}_4$ need to be present initially to act as surfactants, stabilizing single-chain folding and preventing the larger DCMs from inducing interchain aggregation.

In conclude, the synthetic kinetics of DCMs and the folding kinetics of the polymeric template are intricately linked and mutually influence each other. The folding process progresses through two distinct kinetic stages, each governed by different mechanisms. In the first stage, thiol oxidation and thiol–disulfide exchange dominate, limiting folding kinetics due to the presence of thiol groups. In the second

stage, catalytic synchronization between DCC and folding occurs, facilitated by the acceleration of conformational dynamics by smaller macrocycles ($\mathbf{A}_3$ and $\mathbf{A}_4$) and the subsequent stabilization by larger macrocycles ($\mathbf{A}_7$-$\mathbf{A}_{11}$).

The timing of product emergence is crucial for proper folding, highlighting parallels with biological systems where the timing of molecular chaperone action and PTMs is essential for correct protein folding. The necessity of having smaller macrocycles like $\mathbf{A}_3$ and $\mathbf{A}_4$ present initially underscores the importance of sequential interactions in achieving efficient and accurate folding of synthetic polymeric templates.

3.1.8 Anti-cancer drug delivery system synthesized from the Supra-SCNPs

Having elucidated the adaptation mechanism and the synchronization between chemical synthesis and folding kinetics in hydrophobic-effect-driven Supra-SCNPs, we proceeded to explore the encapsulation of the hydrophobic anticancer drug doxorubicin (DOX) to develop drug delivery systems (DDSs) effective against drug-resistant cancer. There are two main advantages of using Supra-SCNPs for constructing DOX-based DDSs: (1) the adaptation mechanism within a hydrophobic-effect-driven folding framework can maximize the loading efficiency of the hydrophobic anticancer drug; and (2) the thiol-free synthetic method, which utilizes only disulfide interchange among fully oxidized $\mathbf{A}_n$, is non-reactive toward DOX, preventing potential denaturation of the drug molecule.

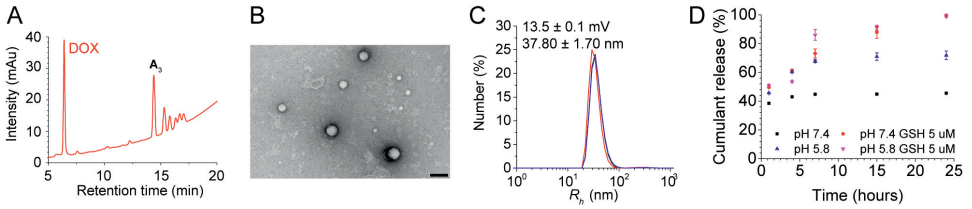

Figure 32 The HPLC analysis (A), TEM image (B), and DLS analysis (C) of the Supra-SCNP-DOX equilibrated from 15 mM $\mathbf{PT}_{703}$, 3 mM **A**, and 2.3 mM DOX at phosphate buffer at pH 7.4. Scale bar = 100 nm. (D) The drug release profile of Supra-SCNP-DOX in different buffer conditions. The acidic pH 5.8 and added 5 mM GSH were set to mimic the cancerous microenvironment. From original publication I.

Therefore, 2.3 mM DOX was first homogenized with 15 mM $\mathbf{PT}_{703}$ and then mixed with a DCL pre-equilibrated with 3.00 mM **A** to achieve instant equilibrium of Supra-SCNP-DOX, ensuring maximum drug loading content (DLC) of fresh DOX. The DLC of Supra-SCNP-DOX was determined by HPLC to be 22%, with a

loading efficiency of 86%. Importantly, no denaturation of DOX was observed (**Figure 32**A).

We found that the maximized DLC benefited from the adaptive enlargement of the Supra-SCNP facilitated by the amplification of $\mathbf{A}_3$. As previously concluded, governed by Le Chatelier's principle, $\mathbf{A}_3$ is responsible for low-degree folding. Specifically, DLS analysis and TEM results suggested that, compared to the R_h of the cargo-free Supra-SCNP (approximately 6 nm), the average R_h of Supra-SCNP-DOX increased to approximately 33 nm (**Figure 32**B and C).

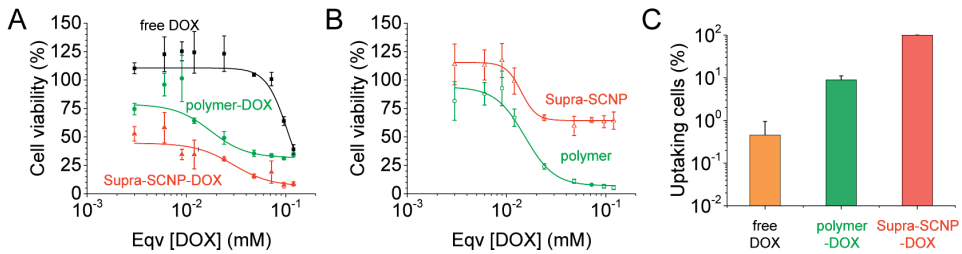

Figure 33 (A) Cytotoxicity test by CCK-8 assay for the different dose forms of DOX at 24 h (standard error, $n = 6$). (B) Cytotoxicity test by CCK-8 of Supra-SCNP and the polymeric template $\mathbf{PT}_{703}$ and $\mathbf{PT}_{703}$ at 24 h (standard error, $n = 6$). (C) The flow cytometry result characterizing the percentage of cells underwent drug internalization after being treated by different dose forms of DOX for 4 hours (standard error, $n = 3$). From original publication I.

Since the single-chain self-assembly is based on disulfide bonds and interactions between deprotonated carboxylate groups and quaternary ammonium groups, Supra-SCNP-DOX is expected to be stable under physiological conditions and responsive in releasing DOX in cancerous environments. Elevated glutathione (GSH) levels and lower intracellular pH (~5.6) had been found in the microenvironment outside the cancer cells[131, 132], which could facilitate the disassembly and drug release by reducing disulfide bonds and protonating carboxylate groups. To verify this property, Supra-SCNP-DOX was incubated in phosphate buffer at pH 7.4 to simulate physiological microenvironments and in reductive or acidic buffers to simulate cancerous microenvironments around the cancer cells. During the incubation period, the drug release profile was monitored by HPLC, which confirmed accelerated drug release in cancerous environments, showcasing the system's responsive drug delivery capability (**Figure 32**D).

The anticancer efficacy of Supra-SCNP-DOX was then evaluated through cell viability tests after incubating it with multidrug-resistant ovarian cancer cells (NCI/RES-ADR), compared to incubation with free DOX, polymer-DOX, polymer, and Supra-SCNP (**Figure 33**A and B). Supra-SCNP-DOX was the most effective, greatly enhancing the drug's potency compared to free DOX and polymer-DOX. In

contrast, the drug-free Supra-SCNP showed minimal cytotoxicity, indicating enhanced biosafety of the carrier molecule alone. Additionally, since the polymer was even more toxic than polymer-DOX, we speculated that the enhancement in anticancer efficacy of Supra-SCNP-DOX mainly stemmed from enhanced drug delivery, while the polymer and polymer-DOX primarily killed cancer cells through inherent toxicity.

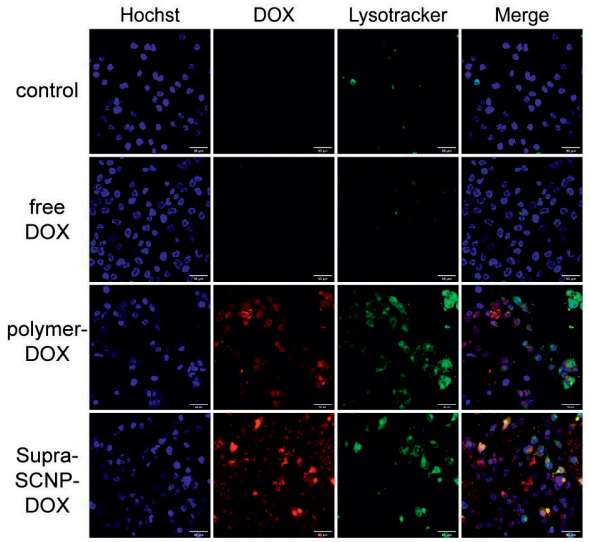

Figure 34 LCSM visualizing intracellular drug internalization after the multi-drug resistant cancer cells were treated by different dose forms of DOX for 4 hours. The blue and green channels are marking the area of cell nucleus and lysosomes stained by Hoechst and lysotracker in the cells respectively. The red channel read the fluorescent signal from DOX, tracking the internalization of the drug molecule. Last the three channels were merged to allow co-localization of the different intracellular component of interest. From original publication I.

To elucidate the anticancer mechanism, flow cytometry and laser confocal scanning microscopy (LCSM) were conducted to track drug delivery efficiency into cancer cells (**Figure 33**C). Flow cytometry revealed that Supra-SCNP-DOX enabled almost the entire cell population to uptake DOX, whereas polymer-DOX facilitated uptake in only about 10% of cancer cells, and free DOX barely entered the cancer cells. Furthermore, LCSM confirmed this difference in delivery efficiency. Thus, the system's efficacy in overcoming drug resistance was attributed to optimized drug delivery (**Figure 34**).

3.1.9 Conclusion

In conclusion, this project successfully addressed the scientific question of how the conformational dynamics and DCC of DCMs interact. This understanding was leveraged to develop high drug-loading-content drug delivery systems (DDSs) effective against drug-resistant cancer *in vitro* (**Figure 35**).

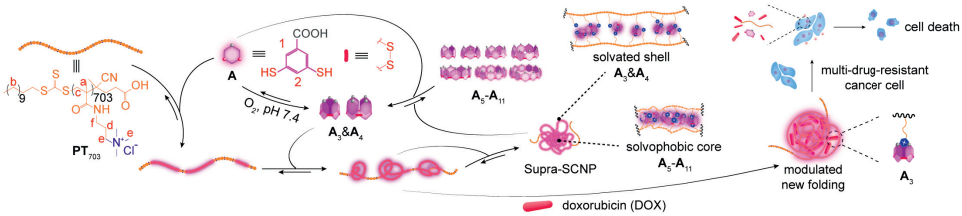

Figure 35 Scheme of the interactive DCMs' molecular network and folding process of the polymeric template for the DCMs, which could further self-adjust adaptively to self-synthesize high drug-loading content drug delivery systems. Cationic pendants were in excess amount over the anionic building block **A**. The molecular network was operated in phosphate buffer at pH 7.4, room temperature and atmospheric pressure. From original publication I.

Specifically, governed by Le Chatelier's principle, larger macrocycles ($\mathbf{A}_5$-$\mathbf{A}_{11}$) were synthesized in the densely folded chain regime, with an amplification of $\mathbf{A}_7$-$\mathbf{A}_{11}$, to counteract the local increase in macrocycle numbers. In contrast, smaller macrocycles ($\mathbf{A}_3$ and $\mathbf{A}_4$) were synthesized in the loosely folded chain regime. The amplification of $\mathbf{A}_3$ was further influenced by its binding affinity, as it demonstrated the most stable binding with available binding sites.

Subsequently, $\mathbf{A}_3$ and $\mathbf{A}_4$ catalyzed conformational exchanges due to their better association with water molecules, facilitating the folding dynamics. Conversely, $\mathbf{A}_5$-$\mathbf{A}_{11}$ tended to stagnate folding and stabilize the polymer in a compact state. However, the presence of free thiol groups in **A** could dominantly reverse the production of larger macrocycles back to $\mathbf{A}_3$, thereby reversing the folding. As the thiols gradually oxidized, disulfide exchange became the major reaction, restoring the folding process.

Finally, by exploiting the adaptation mechanism and synchronized kinetics, the introduction of a hydrophobic molecule like doxorubicin (DOX) into the system led to the amplification of $\mathbf{A}_3$, which enlarged the folding to maximize encapsulation. This resulted in a high-loading-content DDS with stimuli-responsive drug release properties and enhanced potency against drug-resistant cancer.

3.2 Entropy-driven configurational dynamics: high-entropy supramolecular self-assemblies between polymeric template and DCMs

Endowing chemical structures with high configurational entropy represents a new frontier in chemistry, exemplified by the development of high-entropy alloys (HEAs) and high-entropy ceramics (HECs)[133-137]. These materials incorporate multiple principal elements into their sublattice sites, dramatically increasing the number of possible configurations—that is, enhancing configurational entropy—which contributes to their remarkable stability and exceptional properties.

However, this promising approach has been underexplored in the realm of supramolecular self-assemblies, which are fundamental structural components of supramolecular materials[14, 138-142]. One reason is that supramolecular chemical systems are predominantly enthalpy-driven; configurations that facilitate the strongest molecular interactions tend to dominate at equilibrium, thereby minimizing configurational entropy. Moreover, the high-energy processing techniques employed for HEAs and HECs are destructive to the organic components in supramolecular self-assemblies.

Addressing this challenge necessitates new strategies in DCC to enhance the dynamic nature of the constituent species. We posit that the limited structural complexity and flexibility of small molecular templates contribute to this underexplored potential. Upon local entropy loss due to binding, these simple and static molecules offer very few exchangeable states in terms of conformations and configurations, leaving little room for entropy compensation within the supramolecular assembly.

In this project, we investigate the control of supramolecular self-assembly in DCLs by leveraging the entropy-driven configurational dynamics introduced by polymeric templates. Compared to small molecules, polymers possess significant entropic properties, including conformational and solvation entropy, and, most importantly, supramolecular configurational entropy upon binding[143-146]. According to the second law of thermodynamics, the system must achieve a net gain in entropy after the supramolecular assembly process. Therefore, if a penalty to other forms of entropy (such as conformational or solvation entropy) occurs during assembly, the configurational entropy of the self-assembly may increase to compensate.

To achieve high-entropy supramolecular self-assembly, we incorporated DCLs with regulatable dynamic entropy networks using polymers endowed with binding sites on their oligomeric side chains. The numerous binding sites on the polymer offer a greater range of spatial arrangements for binding—in other words, more possible exchangeable states for the configuration of the supramolecular assembly. This variability provides the opportunity to significantly enhance the configurational entropy of the system to compensate for entropy losses from binding, allowing the

bound molecules to engage in dynamic and transient interactions and achieve faster motion along the polymer chain.

3.2.1 Synthesis and characterization of the polymeric template **P**$_{90}$

The polymeric template **P**$_{90}$ was synthesized via reversible addition–fragmentation chain-transfer (RAFT) polymerization (**Figure 36**A). Specifically, 0.160 mmol (0.0646 g, 1.00 equiv) of 4-cyano-4-[(dodecylthio)carbonothioyl]thio]pentanoic acid (CTA, >97%, TCI) was used as the chain-transfer agent, and 0.040 mmol (0.0140 g with approximately 20 wt% H_2O, 1.00 equiv) of 4,4′-azobis(4-cyanovaleric acid) (ACVA, 98%, Alfa Aesar) served as the initiator. Oligo(ethylene glycol) monomethyl ether methacrylate (OEGMA, average oligomerization degree ≈ 9, TCI, ~14.32 mmol, 5.37 g, ~89.50 equiv) was employed as the monomer. All components were dissolved in 15 mL of dimethylformamide (DMF, HPLC grade, Fisher Scientific).

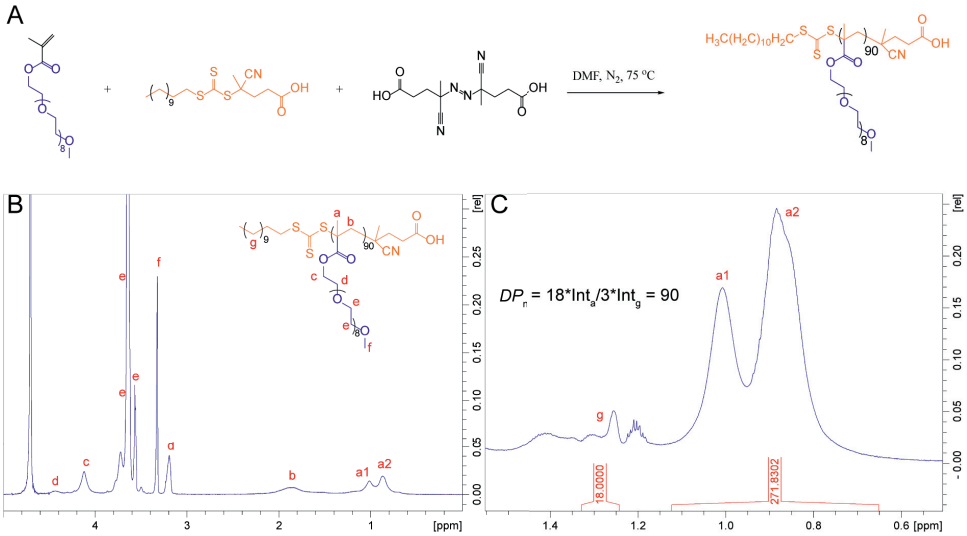

Figure 36 (A) Scheme of the RAFT polymerization to obtain **P**. (B) The assignment to the 1H-NMR spectrum of **P**$_{90}$ dissolved in deuterated phosphate buffer at pD = 7.4. (C) Assignment and integration of the partial ^{1}H-NMR spectrum of 9 mM **P**$_{90}$ dissolved in $CDCl_3$ used for determining the degree of polymerization (DP_n). NMR spectroscopy was operated at 298 K, 600 MHz. From original publication III.

The solution underwent three freeze–pump–thaw cycles to remove dissolved oxygen and establish an inert nitrogen atmosphere. Polymerization was conducted at 75 °C for 8 hours and was terminated by cooling the reaction mixture in an ice bath.

The resulting product, $\mathbf{P}_{90}$ (7.05 g), was obtained as a white solid after dialysis against water (changing the water every 12 hours) using a molecular weight cut-off (MWCO) of 3,000, followed by freeze-drying.

The DP_n of $\mathbf{P}_{90}$ was determined from the proton nuclear magnetic resonance ^{1}H NMR spectroscopy results by comparing the integration areas of the methylene protons (H_a) and the terminal methyl protons (H_g) (**Figure 36**B and C). The DP_n was calculated using the equation: $DP_n = (3I_a) / (I_g / 18) = 90$, where I_a is the integration area of the methylene protons and I_g is the integration area of the terminal methyl protons. This calculation confirms that the polymer consists of approximately 90 repeating units.

3.2.2 Characterizing the binding of $\mathbf{A}_n$ to $\mathbf{P}_{90}$

Ligand binding to polymers is known to impose a penalty on the polymer's conformational entropy by restricting its conformational freedom, and polymerized chains of hydrophilic oligomeric ethylene glycol can bind to small molecules similar to $\mathbf{A}_n$ through the enhanced hydrophobic effects in-between the chains[147, 148]. Typically, a higher ligand-to-polymer binding stoichiometry results in a greater reduction of the polymer's conformational entropy due to increased conformational constraints. Thus, to control conformational entropy of the polymer $\mathbf{P}_{90}$ via the binding of $\mathbf{A}_n$, we prepared a series of DCLs with a fixed concentration of $\mathbf{P}_{90}$ at 9 mM and varying concentrations of the building block **A**, ranging from 0.3 mM to 18 mM. This setup adjusted the stoichiometry of $\mathbf{A}_n/\mathbf{P}_{90}$ from 1:30 to 2:1, and the series was labeled as *x***A**-9**P**, where *x* represents the concentration of **A**.

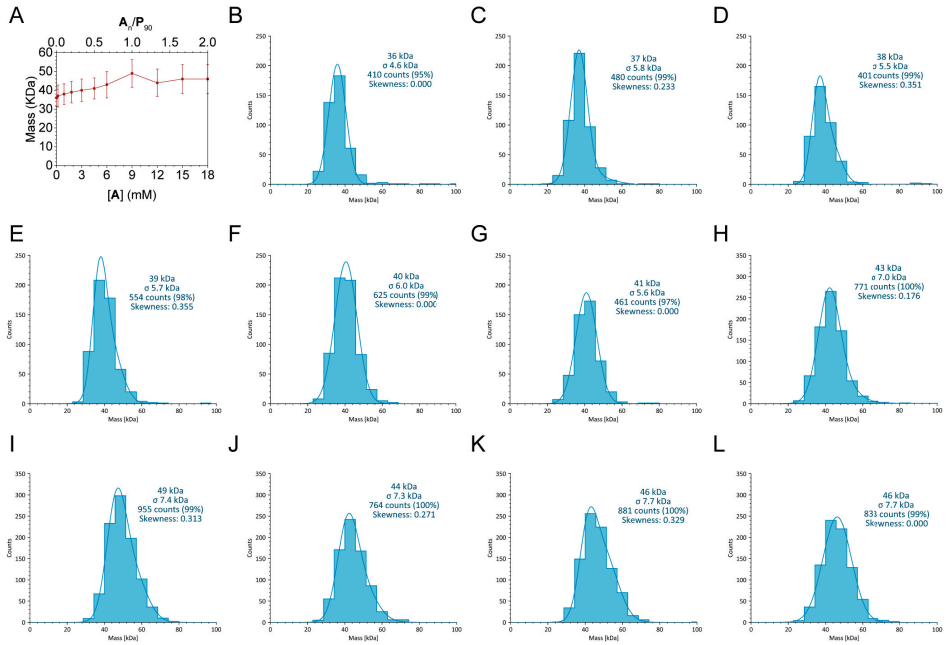

Figure 37 (A) The number-averaged mass and standard deviation of the molecular complexes in the *x***A**-9$\mathbf{P}_{90}$ DCLs equilibrated from *x* mM **A** and 9 mM $\mathbf{P}_{90}$. The x-axis present the concentration of **A** in each sample. And the calibrated histograms of mass photometry for the (B) 9 mM $\mathbf{P}_{90}$ solution, (C) 0.18**A**-9$\mathbf{P}_{90}$ DCL, (D) 0.9**A**-9$\mathbf{P}_{90}$ DCL, (E) 1.8**A**-9$\mathbf{P}_{90}$ DCL, (F) 3**A**-9$\mathbf{P}_{90}$ DCL, (G) 4.5**A**-9$\mathbf{P}_{90}$ DCL, (H) 6**A**-9$\mathbf{P}_{90}$ DCL, (I) 9**A**-9$\mathbf{P}_{90}$ DCL, (J) 12**A**-9$\mathbf{P}_{90}$ DCL, (K) 15**A**-9$\mathbf{P}_{90}$ DCL, and (L) 18**A**-9$\mathbf{P}_{90}$ DCL. From original publication III.

The samples were equilibrated and characterized using mass photometry (MP) (**Figure 37**). The MP results indicated that the binding of $\mathbf{A}_n$ to $\mathbf{P}_{90}$ increased with the $\mathbf{A}_n/\mathbf{P}_{90}$ ratio up to a stoichiometry of 1:1. Specifically, as the $\mathbf{A}_n/\mathbf{P}_{90}$ ratio increased from 0 to 1, the measured mass values consistently rose, reflecting greater binding of $\mathbf{A}_n$ to $\mathbf{P}_{90}$. However, further increasing the $\mathbf{A}_n/\mathbf{P}_{90}$ ratio beyond 1:1 did not lead to a significant change in the measured mass values. This observation suggests that the binding sites on $\mathbf{P}_{90}$ become saturated when the $\mathbf{A}_n/\mathbf{P}_{90}$ ratio reaches 1:1. Therefore, any additional $\mathbf{A}_n$ beyond this ratio likely remains unbound and freely dissolved in the solution.

3.2.3 Charaterizing the conformational entropy upon the binding of $\mathbf{A}_n$ to $\mathbf{P}_{90}$

Having established the binding profile of $\mathbf{A}_n$ to $\mathbf{P}_{90}$, we proceeded to evaluate how this binding affects the polymer's conformational entropy. Specifically, we characterized the conformational changes of $\mathbf{P}_{90}$ upon binding with $\mathbf{A}_n$.

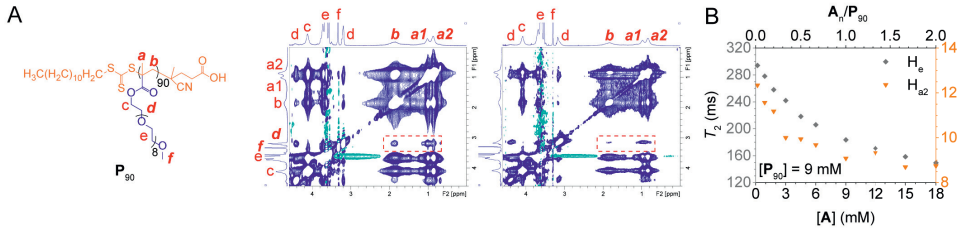

Figure 38 (A) Partial NOESY 2D plot of 9 mM $\mathbf{P}_{90}$ (in monomer, middle), and DCL equilibrated from 9 mM **A** and 9 mM $\mathbf{P}_{90}$ (9**A**-9$\mathbf{P}_{90}$, right). (B) The T_2 of H_e on $\mathbf{P}_{90}$'s pendant and H_{a2} on $\mathbf{P}_{90}$'s backbone from the DCLs equilibrated from different concentration of **A** and a fixed 9 mM concentration of $\mathbf{P}_{90}$ (in monomer, *x*$\mathbf{A}$-9$\mathbf{P}_{90}$ DCLs). NMR spectroscopy was operated at 298 K and 600 MHz. From original publication III.

Firstly, NOESY was employed to investigate chain rearrangements after binding (**Figure 38**A). The NOESY 2D plot showed a dramatic decrease in NOE correlations between the backbone proton Hb and the side-chain protons Hd and Hf upon binding of $\mathbf{A}_n$ to $\mathbf{P}_{90}$. This decrease indicates that the side chains become more distant from the backbone after binding, suggesting that the polymer adopts a more extended conformation.

Since conformational entropy can decrease when a polymer chain becomes more stretched due to restricted conformational freedom, we measured the T_2 of the side chain proton (H_e) and backbone proton (H_{a2}) to assess changes in molecular motion (**Figure 38**B). Indeed, the T_2 values of both characteristic side-chain and backbone protons decreased with increased binding of $\mathbf{A}_n$ to $\mathbf{P}_{90}$, exhibiting a saturation point at an $\mathbf{A}_n/\mathbf{P}_{90}$ ratio of 1:1—consistent with the binding saturation observed in the MP results.

These findings confirm that the binding of $\mathbf{A}_n$ to $\mathbf{P}_{90}$ stretches the polymer conformation, and that increased binding leads to further stretching. This stretching restricts molecular motion, resulting in a decrease in conformational entropy.

3.2.4 Characterizing the DCMs' response of speciation to the penalty on the conformational entropy

To investigate how the DCMs of $\mathbf{A}_n$ respond to penalties on conformational entropy, we analyzed the *x*$\mathbf{A}$-9$\mathbf{P}_{90}$ DCLs using HPLC-MS (**Figure 39**A). As the concentration of **A** increased—thereby imposing a greater penalty on the conformational entropy of the polymer $\mathbf{P}_{90}$—we observed a decrease in the conversion of $\mathbf{A}_3$, while the conversions of $\mathbf{A}_4$ and $\mathbf{A}_7$-$\mathbf{A}_{11}$ increased.

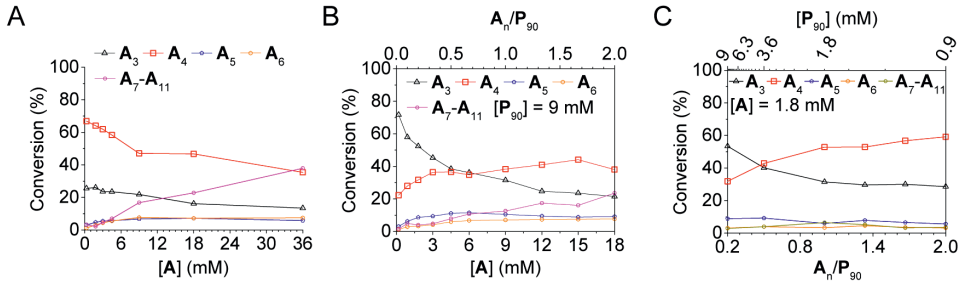

Figure 39 The conversion of **A** to different subsets of $\mathbf{A}_n$ in the DCLs equilibrated from different concentrations of **A** at pH 7.4 and room temperature, in (A) *x***A** DCLs for referencing or (B) *x***A**-9$\mathbf{P}_{90}$ DCLs with the directing polymer $\mathbf{P}_{90}$ (9 mM, in monomer).(C) 1.8**A**-*y*$\mathbf{P}_{90}$ DCLs equilibrated from a fixed 1.8 mM concentration of **A** at pH 7.4, with the changing concentration (in monomer) of the polymeric template $\mathbf{P}_{90}$, which regulated the $\mathbf{A}_n/\mathbf{P}_{90}$ stoichiometry (in building block/monomer) ranged from 0.2 to 2.0, similar to the *x***A**-9$\mathbf{P}_{90}$ DCLs. From original publication III.

In comparison, control DCLs labeled *x***A**, prepared without the polymer $\mathbf{P}_{90}$ and with **A** concentrations ranging from 0.3 mM to 18 mM, showed that increases in **A** concentration led to decreased conversions of both $\mathbf{A}_3$ and $\mathbf{A}_4$ (**Figure 39**B). Only the conversions of $\mathbf{A}_7$-$\mathbf{A}_{11}$ increased, governed by Le Chatelier's principle. The key difference between the *x***A**-9$\mathbf{P}_{90}$ and *x***A** DCLs was the increased conversion of $\mathbf{A}_4$ in the presence of $\mathbf{P}_{90}$ upon increasing **A** concentration, suggesting that $\mathbf{A}_n$ responds to the increased conformational entropy penalty of $\mathbf{P}_{90}$ by favoring the formation of $\mathbf{A}_4$.

To determine whether the increased conversion of $\mathbf{A}_7$-$\mathbf{A}_{11}$ was also a response of $\mathbf{A}_n$ to the conformational entropy penalty, we prepared another set of DCLs with a fixed **A** concentration of 1.8 mM and varying $\mathbf{P}_{90}$ concentrations from 0.9 mM to 9.0 mM, labeled as 1.8**A**-*y*$\mathbf{P}_{90}$. This setup provided similar $\mathbf{A}_n/\mathbf{P}_{90}$ ratios ranging from 1:5 to 2:1, comparable to those in the *x***A**-9$\mathbf{P}_{90}$ DCLs. By fixing the concentration of **A**, we minimized the influence of Le Chatelier's principle, isolating the effect of increased binding stoichiometry ($\mathbf{A}_n/\mathbf{P}_{90}$) on conformational entropy.

In these 1.8**A**-*y*$\mathbf{P}_{90}$ DCLs, the conversions of $\mathbf{A}_7$-$\mathbf{A}_{11}$ remained steady despite the increasing $\mathbf{A}_n/\mathbf{P}_{90}$ ratios, while the conversion of $\mathbf{A}_3$ decreased and that of $\mathbf{A}_4$ increased (**Figure 39**C). This indicates that the changes in $\mathbf{A}_7$-$\mathbf{A}_{11}$ conversions observed in the *x***A**-9$\mathbf{P}_{90}$ DCLs were solely due to Le Chatelier's principle and not related to entropic effects. In contrast, the observed trade-off between $\mathbf{A}_3$ and $\mathbf{A}_4$ appears to be a direct response to the penalty on the conformational entropy of $\mathbf{P}_{90}$. Specifically, the system compensates for the entropy loss by favoring the formation of $\mathbf{A}_4$ over $\mathbf{A}_3$ when the conformational entropy penalty increases due to higher binding stoichiometry.

3.2.5 Characterizing the configurational entropy gained by the conversion to $\mathbf{A}_4$

Recognizing that the amplification of $\mathbf{A}_4$ correlates with the penalty on conformational entropy due to increased binding of $\mathbf{A}_n$ to $\mathbf{P}_{90}$, we investigated the binding affinities of each $\mathbf{A}_n$ subset to $\mathbf{P}_{90}$ and studied the molecular dynamics of the bound $\mathbf{A}_n$ species to understand their responses to the conformational entropy penalty.

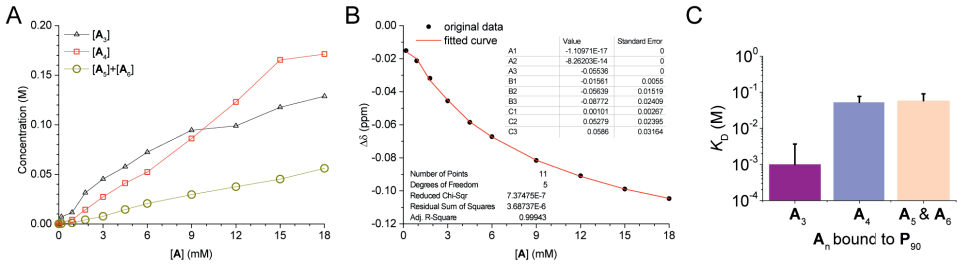

Figure 40 (A) The concentration of $\mathbf{A}_3$, $\mathbf{A}_4$, and $\mathbf{A}_5$+ $\mathbf{A}_6$ in each *x*$\mathbf{A}$-9$\mathbf{P}_{90}$ DCL with different overall concentration of $\mathbf{A}_n$ counted in $\mathbf{A}$. The concentration data was later used in the fitting for the Langmuir isotherm. (B) The fitting result for the three component Langmuir isotherm. (C) Apparent dissociation constants (K_D) of $\mathbf{A}_3$, $\mathbf{A}_4$, and $\mathbf{A}_5$&$\mathbf{A}_6$ when bound to $\mathbf{P}_{90}$. The error bars represent the standard error derived from the fitting process. From original publication III.

Firstly, according to previous reports[149, 150], we applied Langmuir isotherm fitting to the chemical shift data of the binding sites on the polymer (from ^{1}H NMR spectroscopy) and the concentrations of different $\mathbf{A}_n$ species (from HPLC analysis) in the *x*$\mathbf{A}$-9$\mathbf{P}_{90}$ DCLs (**Figure 40**A and B). The model function was simplified based on the binding modes. According to previous studies, the proton H_e is the primary binding site for hydrophobic ligands on the polymer, so its chemical shift was used for fitting.

We omitted the contribution of $\mathbf{A}_7$-$\mathbf{A}_{11}$ since they accounted for less than 10% of the total $\mathbf{A}_n$ concentration and their sub-species were unassignable. $\mathbf{A}_5$ and $\mathbf{A}_6$ were approximated to have the same binding affinity and mode due to their similar minor conversions and coalesced ^{1}H NMR peaks. Thus, three major species—$\mathbf{A}_3$, $\mathbf{A}_4$, and $\mathbf{A}_5$ + $\mathbf{A}_6$—were used in the fitting process. The fitting yielded the apparent binding affinities (dissociation constants, K_D) of $\mathbf{A}_3$, $\mathbf{A}_4$, and $\mathbf{A}_5$ + $\mathbf{A}_6$ to $\mathbf{P}_{90}$ (**Figure 40**C). The results indicated that $\mathbf{A}_3$ is the strongest binder, with a K_D approximately 50 times smaller than those of the weaker binders $\mathbf{A}_4$ and $\mathbf{A}_5$ + $\mathbf{A}_6$. However, it is important to note the K_D determined here is only for qualitative comparison, as it is not accurate due to limited number of data points (10) used for the fitting with 9 parameters.

To further validate these findings, we examined the binding modes of the different $\mathbf{A}_n$ species using Saturation Transfer Difference NMR (STD NMR) (**Figure 41**). In STD NMR, protons closer to the macromolecular binding site exhibit higher STD responses[151, 152]. By measuring and normalizing the STD responses of each proton within the binder molecules relative to the macromolecule, we could elucidate their binding modes.

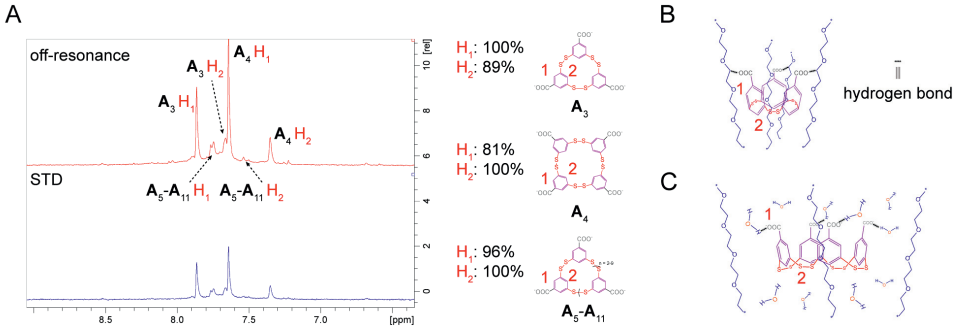

Figure 41 (A) Left: STD-NMR experiment of the DCL equilibrated from 18 mM **A** and 9 mM $\mathbf{P}_{90}$ (in monomer, 18**A**-9$\mathbf{P}_{90}$), presenting the partial spectrum with the peaks from the $\mathbf{A}_n$ species. The experiment was operated at 298 K, 500 MHz. The upper part is the off-resonance spectrum, where saturation was not directly applied to the molecules. Lower is the STD spectrum showing the STD response as saturated portion of $\mathbf{A}_n$'s signal due to their binding events to $\mathbf{P}_{90}$. Right: STD responses in each $\mathbf{A}_n$ species normalized by the strongest responding protons. According to the K_D and STD responses for $\mathbf{A}_3$ and $\mathbf{A}_4$, their binding modes to $\mathbf{P}_{90}$ were rationalized and presented in Schemes (**E**) and (**F**), respectively. From original publication III.

All $\mathbf{A}_n$ species possess protons H_1 and H_2, where H_1 represents the polar hydrophilic part bearing a carboxylate group, and H_2 represents the nonpolar hydrophobic part. For $\mathbf{A}_3$, H_1 showed the highest STD response, suggesting that $\mathbf{A}_3$ enhances its interaction with $\mathbf{P}_{90}$ through a weak hydrogen bond with adjacent polymer pendants in a more compact chain region. This interaction makes $\mathbf{A}_3$ the enthalpy-favored strongest binder. In contrast, for $\mathbf{A}_4$ and $\mathbf{A}_5$–$\mathbf{A}_{11}$, H_2 exhibited the highest STD responses, indicating that their hydrophilic parts mainly interact with water molecules in more extended chain regions, making them weaker binders. The similar STD responses of H_1 and H_2 in $\mathbf{A}_5$–$\mathbf{A}_{11}$ suggest an ill-defined hydrophobic weak binding with $\mathbf{P}_{90}$. Overall, the binding modes align well with their apparent binding constants.

Interestingly, as the binding stoichiometry increased, the conversion to the weak binder $\mathbf{A}_4$ increased the most, suggesting an unusual amplification compared to conventional enthalpy-controlled DCLs. This phenomenon can be attributed to compensation for configurational entropy loss due to the reduction in conformational entropy. A more dynamic translational or rotational motion of the weakly bound

binder on the macromolecule increases the supramolecular configurational entropy by expanding the number of possible arrangements of bound binding sites (**Figure 42**A). To identify whether $\mathbf{A}_4$ contributes most to increasing configurational entropy, we measured the D and T_2 of each bound $\mathbf{A}_n$ species (**Figure 42**B and C). Indeed, $\mathbf{A}_4$ exhibited the highest diffusion constant, and its T_2 was the most sensitive to decreased conformational entropy upon increased binding stoichiometry.

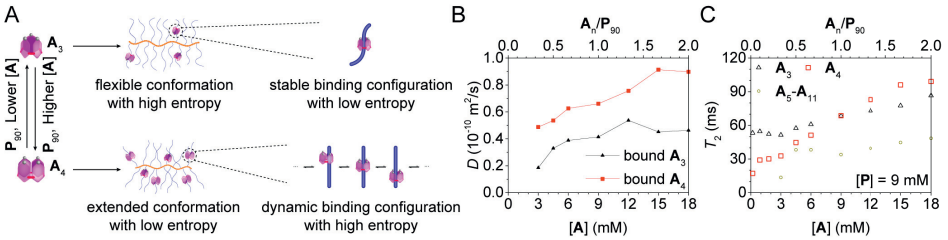

Figure 42 (A) Scheme showing the mechanism for the production of $\mathbf{A}_3$ and $\mathbf{A}_4$ when bound to $\mathbf{P}_{90}$. (B) Diffusion coefficients (D) of $\mathbf{A}_3$ and $\mathbf{A}_4$ bound to **P** in x**A**-9$\mathbf{P}_{90}$ DCLs. (C) T_2 of $\mathbf{A}_3$, $\mathbf{A}_4$ and $\mathbf{A}_5$-$\mathbf{A}_{11}$ in x**A**-9$\mathbf{P}_{90}$ DCLs. From original publication III.

After confirming that the molecular dynamics of $\mathbf{A}_4$ favor enhanced configurational entropy, we proceeded to quantify the compensatory configurational entropy gained by the increased conversion to $\mathbf{A}_4$. In the 1.8**A**-$y\mathbf{P}_{90}$ DCLs, we observed primarily an entropy-induced trade-off between $\mathbf{A}_3$ and $\mathbf{A}_4$, with negligible influence from Le Chatelier's principle on the minor conversion of $\mathbf{A}_5$-$\mathbf{A}_{11}$. This simplification allowed us to assume that the conversion between $\mathbf{A}_3$ and $\mathbf{A}_4$ operates as a closed reaction.

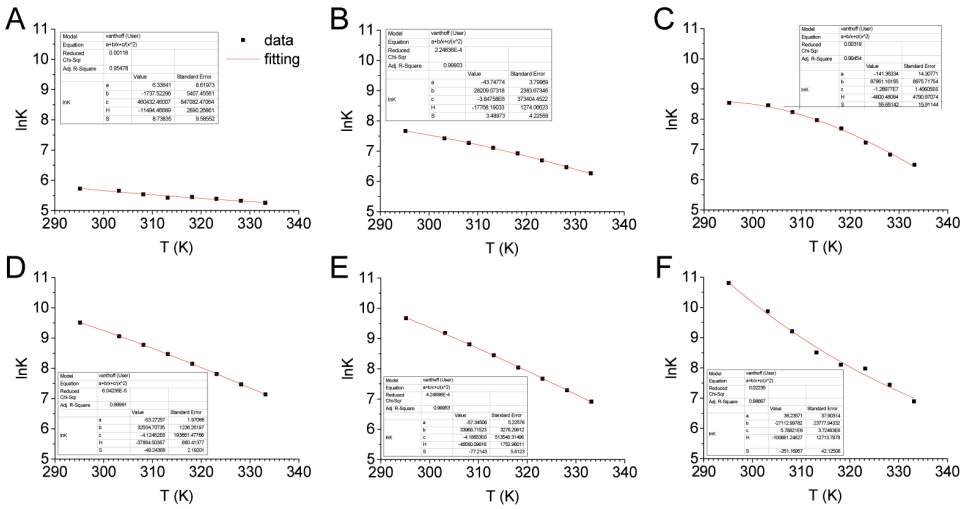

Figure 43 Plotting the changing on lnK_{eq} of 1.8**A**-9$\mathbf{P}_{90}$ DCL (A), 1.8**A**-3.6$\mathbf{P}_{90}$ DCL (B), 1.8**A**-1.8$\mathbf{P}_{90}$ DCL (C), 1.8**A**-1.35$\mathbf{P}_{90}$ DCL (D), 1.8**A**-1.08$\mathbf{P}_{90}$ DCL (E), 1.8**A**-0.9$\mathbf{P}_{90}$ DCL (F) responsive to temperature (T), and fitting the lnK_{eq} –T data to a modified Van 't Hoff equation. From original publication III.

Based on this assumption, we applied a modified Van 't Hoff equation to obtain the changes in entropy ($\Delta S_{reaction}$) and enthalpy ($\Delta H_{reaction}$) associated with the conversion from $\mathbf{A}_3$ to $\mathbf{A}_4$[153]. Each sample in the 1.8**A**-$y\mathbf{P}_{90}$ DCLs and the control sample 1.8**A** was equilibrated at different temperatures and analyzed by HPLC to determine the concentrations of $\mathbf{A}_3$ and $\mathbf{A}_4$, from which we derived the lnK_{eq} of the conversion (**Figure 43**). After fitting, we subtracted the $\Delta S_{reaction}$ and $\Delta H_{reaction}$ of the control sample from those of each experimental sample to obtain $\Delta\Delta S_{reaction}$ and $\Delta\Delta H_{reaction}$ (**Figure 44**A-C), which reflect contributions from molecular dynamics during the binding of $\mathbf{A}_4$ to $\mathbf{P}_{90}$. Finally, we calculated the total changes in entropy ($\Delta\Delta S_{total}$) and enthalpy ($\Delta\Delta H_{total}$) at the system level in each sample based on the amount of $\mathbf{A}_4$ converted (**Figure 44**D and E).

Overall, the conversion became increasingly favorable in terms of free energy during binding, as evidenced by a progressively more negative $\Delta G_{reaction}$ until binding saturation at an $\mathbf{A}_n/\mathbf{P}_{90}$ ratio of 1:1 (**Figure 44**F). Moreover, both $\Delta\Delta S_{total}$ and $\Delta\Delta H_{total}$ in the 1.8**A**-$y\mathbf{P}_{90}$ DCLs increased before reaching binding saturation and remained positive up to an $\mathbf{A}_n/\mathbf{P}_{90}$ ratio of 4:3. This indicates that the conversion to $\mathbf{A}_4$ enhances the configurational entropy and internal energy of the supramolecular self-assembly between $\mathbf{A}_n$ and $\mathbf{P}_{90}$. The subsequent drop in $\Delta\Delta S_{total}$ and $\Delta\Delta H_{total}$ after binding saturation can be attributed to the emergence of bound-free conversions once saturation is achieved.

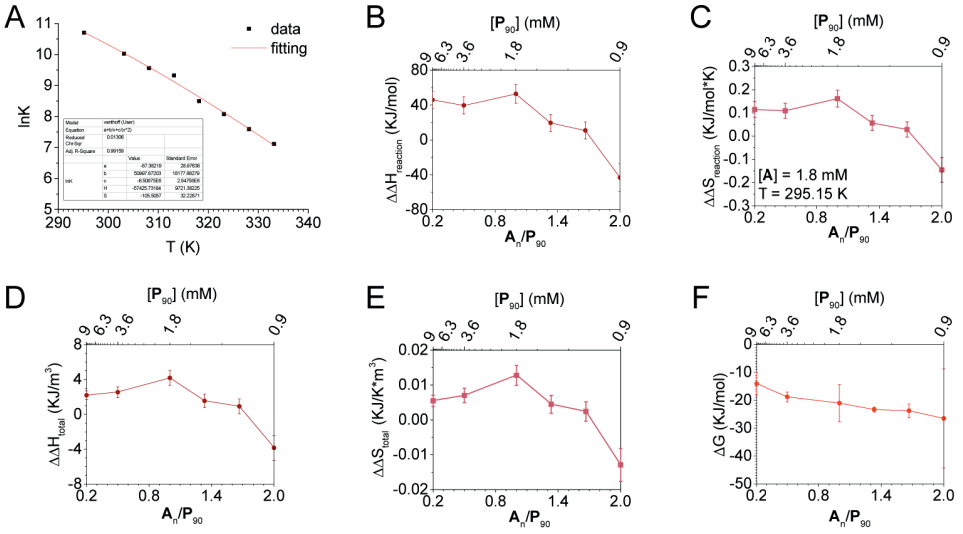

Figure 44 (A) Diagram of changing on lnK_{eq} of the control 1.8**A** DCL in response to varied temperature (T), and fitting the lnK_{eq} –T data to a modified Van 't Hoff equation. $\Delta\Delta H_{reaction}$ (B), $\Delta\Delta S_{reactionl}$ (C), $\Delta\Delta H_{total}$ (D), $\Delta\Delta S_{total}$ (E), and $\Delta G_{reaction}$ (E) of the 1.8**A**-*y***P** DCLs. The standard error was derived from the fitting processes. From original publication III.

In conclusion, we achieved supramolecular self-assembly with high configurational entropy by using the binding of DCMs to the polymeric template to impose a penalty on the polymer's conformational entropy. This induced restructuring of the DCMs toward weaker but more dynamically mobile binders, such as $\mathbf{A}_4$, thereby increasing the configurational entropy of the supramolecular assembly.

3.2.6 Characterization to the solvation entropy change along with salt addition

To further highlight the significance of the dynamics in entropy network in the polymer-based system, we investigated the effect of applying a penalty to the solvation entropy.

This penalty was imposed by adding increasing concentrations of the kosmotropic salt sodium chloride (NaCl) to the DCLs equilibrated from 1.8 mM **A** and 1.8 mM $\mathbf{P}_{90}$. Specifically, NaCl was added at concentrations of 100, 500, and 1000 mM, creating DCLs designated as 1.8**A**-1.8$\mathbf{P}_{90}$-*z*NaCl, where *z* represents the NaCl concentration. The kosmotropic nature of NaCl is well-known for increasing order in aqueous solvent systems, which decreases solvation entropy[150, 154]. This effect enhances the hydrophobicity of macromolecular solutes by restricting their

molecular motion, causing them to "salt out" from the solution and freeing solvent molecules to compensate for the entropy loss. We speculated that the addition of NaCl would restrict molecular motion and induce changes in the self-assembly between the DCMs and the polymeric template.

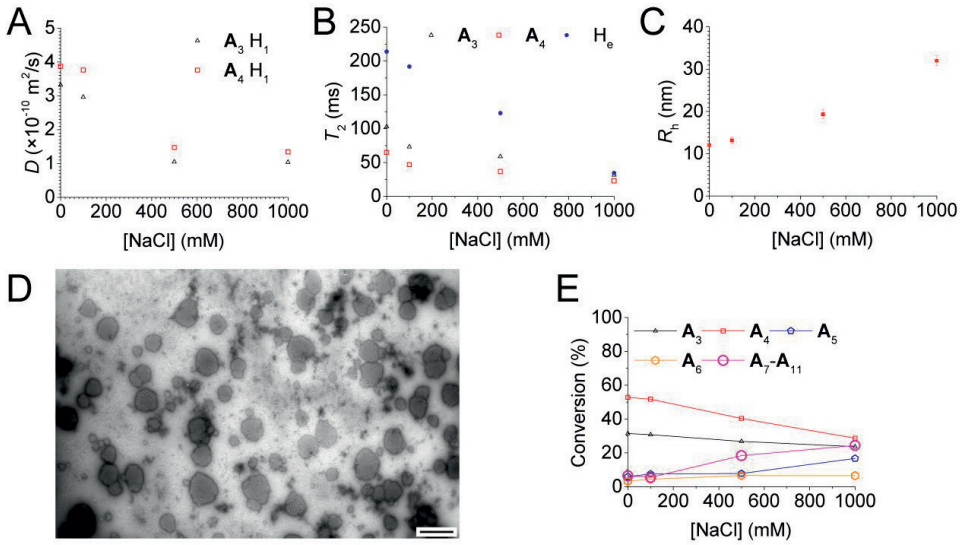

Figure 45 *D* (A) and T_2 (B) of $\mathbf{A}_3$ H_1 and $\mathbf{A}_4$ H_1 in the 1.8**A**-1.8$\mathbf{P}_{90}$-*z*NaCl DCLs. (C) Number averaged diameter of the 1.8**A**-1.8$\mathbf{P}_{90}$-*z*NaCl DCLs. determined by DLS analysis. (D) TEM image of the salt-induced aggregation, scale bar = 500 nm. (E) HPLC analysis to the 1.8**A**-1.8$\mathbf{P}_{90}$-*z*NaCl DCLs. From original publication III.

Indeed, after adding increasing amounts of NaCl, the molecular motions of both $\mathbf{P}_{90}$ and $\mathbf{A}_n$ were further restricted by the more ordered solvent environment, as evidenced by decreased *D* and T_2 with increasing *z* (**Figure 45**A and B). Additionally, DLS analysis showed that the number-averaged R_h increased as the salt concentration rose, suggesting salt-induced enhanced aggregation (**Figure 45**C). TEM revealed irregular nano-aggregates with diameters ranging from 30 to 300 nm (**Figure 45**D). HPLC analysis found that the production of larger macrocycles $\mathbf{A}_5$-$\mathbf{A}_{11}$ was upregulated as aggregation emerged (**Figure 45**E).

These results suggest that $\mathbf{A}_4$ lost its ability to compensate for the entropy loss by facilitating dynamic configurational exchanges due to the solvent's restrictive effect. Consequently, as shown by the DLS analysis and TEM, the self-assembly between $\mathbf{P}_{90}$ and $\mathbf{A}_n$ underwent aggregation to compensate for the entropy loss, which was detrimental to the formation of supramolecular self-assemblies with high configurational entropy. The aggregation concentrated $\mathbf{A}_n$ within and led to the amplification of larger macrocycles under the guidance of Le Chatelier's principle.

3.2.7 Conclusion

In this second part of the study, we have demonstrated a novel strategy for controlling entropy-driven configurational dynamics in DCC through the use of polymeric templates. Our key findings are summarized as follows:

First, we showed that polymeric templates can introduce a controllable entropic network within DCC systems. This provides a new approach for manipulating entropy-driven configurational dynamics, expanding the methodologies available for controlling supramolecular self-assembly.

Second, by applying a penalty to the conformational entropy of the polymeric template—achieved through increased binding of dynamic combinatorial macrocycles (DCMs)—we facilitated the formation of high-entropy and high-kinetic-energy single-chain polymer–macrocycle complexes. This adaptation compensates for the loss of conformational entropy by enhancing the configurational entropy of the supramolecular assembly, allowing for more dynamic and transient interactions.

Third, when a penalty was applied to the solvation entropy, such as by adding kosmotropic salts like NaCl, we observed that aggregation between polymer–macrocycle complexes became predominant. The restricted molecular motion and decreased solvation entropy led to the system compensating through aggregation, which concentrated the macrocycles and amplified larger species under the guidance of Le Chatelier's principle.

These findings highlight the critical role of entropic contributions in controlling the self-assembly processes within DCC systems. By strategically manipulating different forms of entropy—conformational and solvation—we can direct the formation of desired supramolecular structures. This work opens new avenues for the design and synthesis of advanced materials with tailored properties, leveraging entropy network to achieve high configurational entropy in supramolecular assemblies.

3.3 The cooperation between multiple dynamics: the multi-stage and pathway-dependent self-assembly mediated by a di-block copolymeric template

Building upon the first two projects, where polymeric templates were developed to regulate dynamic combinatorial chemistry (DCC) either through conformational dynamics or entropy-driven configurational dynamics, we sought to explore how these different types of dynamics could work together to achieve higher-order complexity and functionality in systems chemistry.

In systems chemistry, understanding the interplay between different dynamics is crucial for developing systems with emergent properties. For example, significant research has focused on how different types of dynamic covalent reactions can operate together within a single chemical system. These reactions can be orthogonal or communicating and may work simultaneously or sequentially. Such diverse working modes not only increase the system's complexity—better mimicking biological behaviors—but also empower chemical systems to function as molecular machinery and form functional hydrogels. In stark contrast, due to the lack of dynamics in conventional templates, there has been little research on template effects involving multiple dynamics.

Now, with the introduction of two new dynamics brought by polymeric templates, it is possible to construct a chemical system where different dynamics originate from the template itself and to study how they interact.

Therefore, in the third part of my thesis, I aimed to investigate what new emergent properties would arise when both dynamics operate together within the same polymeric template. The two different polymeric templates from the first two projects were combined to form a diblock copolymeric template, $\mathbf{PT}_{60}$-$\mathbf{P}_{90}$. This $\mathbf{PT}_{60}$-$\mathbf{P}_{90}$ was interacted with $\mathbf{A}_n$ in different stoichiometries to trigger distinct dynamics and achieve multi-stage control over the self-assembly process. Moreover, the fresh building block **A** was found to be an essential kinetic intermediate that counters the kinetic barrier of interparticle charge repulsion and mediates polymersome fusion in a controllable manner.

3.3.1 Synthesis and characterization the co-polymeric template $\mathbf{PT}_{60}$-$\mathbf{P}_{90}$

The synthetic and purification procedure was similar to the previous two polymers (**Figure 46**A). Briefly, in a 15 mL aqueous solvent (DMF/H_2O = 3/7 v/v), $\mathbf{P}_{90}$ was used as the macromolecular chain transfer agent (**MCTA**, 0.90 g, ~0.02 mmol, ~1.00 eq.), **AVCA** (0.0070 g, 0.01 mmol, ~1.00 eq.) was used as the initiator, and **MAPTAC** was the monomer (0.4892 g, 1.190 mmol, ~ 59.50 eq.). The product was 1.3 g as pale yellow solid. The DP_n of the $\mathbf{PT}_{60}$ block was determined by comparing the integration area of the characteristic proton H_e on the $\mathbf{PT}_{60}$ block and H_g on the $\mathbf{P}_{90}$ block: $DP_n = 90 \times 2I_e/11I_f$ (**Figure 46**B).

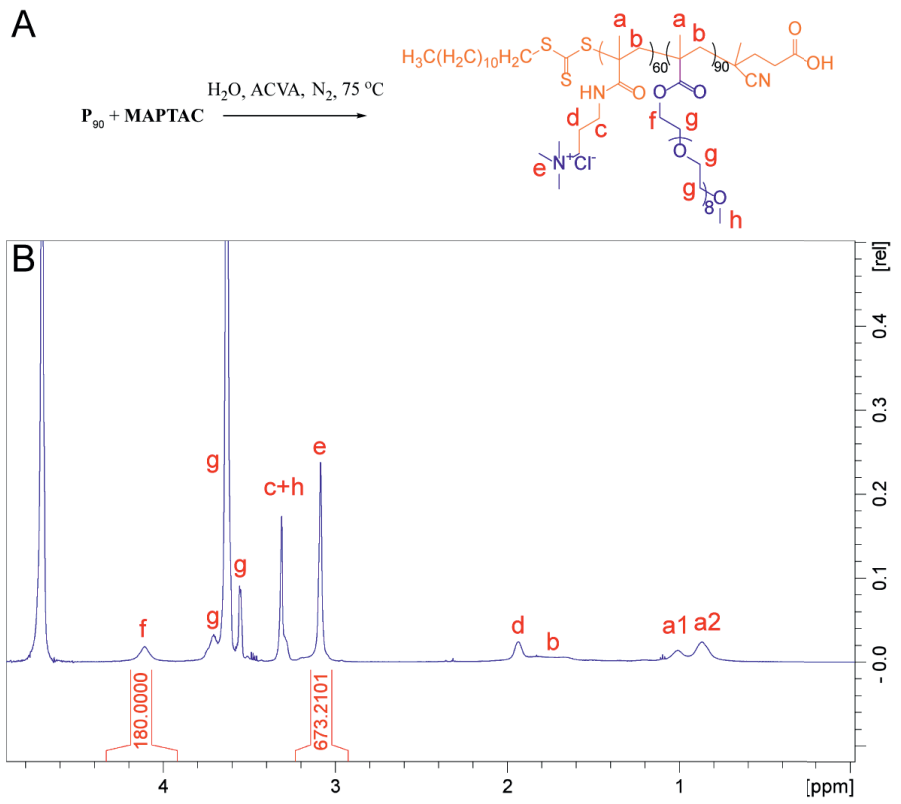

Figure 46 (A) Scheme of RAFT polymerization for $\mathbf{PT_{60}}$-$\mathbf{P_{90}}$ diblock copolymer. (B) ^{1}H NMR spectrum and peak assignment of the $\mathbf{PT_{60}}$-$\mathbf{P_{90}}$ diblock copolymer dissolved in deuterated phosphate buffer at pD 7.4, measured at 298 K, 600 MHz. From original publication IV.

3.3.2 Characterizing the binding stages featured by binding stoichiometry and binding modes of DCM to the co-polymeric template

To elucidate the binding stages between $\mathbf{A}_n$ and $\mathbf{PT_{60}}$-$\mathbf{P_{90}}$ diblock copolymer, a series of DCLs (x**A**-15$\mathbf{PT_{60}}$-$\mathbf{P_{90}}$) was prepared. Each DCL contained a fixed concentration of $\mathbf{PT_{60}}$-$\mathbf{P_{90}}$ at 15 mM (in terms of its monomeric pendants, comprising 6.00 mM cationic pendants from the $\mathbf{PT_{60}}$ block and 9.00 mM neutral pendants from the $\mathbf{P_{90}}$ block) and increasing concentrations of **A** from 0.12 to 15.00 mM. After equilibration, the x**A**-15$\mathbf{PT_{60}}$-$\mathbf{P_{90}}$ DCLs were analyzed by ^{1}H NMR and ^{1}H–^{1}H NOESY to determine the binding modes (**Figure 47**). Two distinct binding stages emerged from the NMR results:

First Binding Stage ([**A**] = 0.12 to 6.00 mM)**:** Within this concentration range, only the cationic $\mathbf{PT_{60}}$ block interacted with $\mathbf{A}_n$. As **A** concentration increased, the

proton signals from the **PT**$_{60}$ block in the polymer displayed an upfield shift, became progressively broader, and showed reduced integration, while the neutral **P**$_{90}$ block remained unchanged (**Figure 47**A). These chemical shift alterations indicated that **A**$_n$ bound exclusively to the cationic block, neutralizing its charge. Moreover, NOESY 2D plot of the 3**A**-15**PT**$_{60}$-**P**$_{90}$ DCL confirmed that **A**$_n$ exhibited NOE correlations only with the cationic **PT**$_{60}$ block and not with the neutral **P**$_{90}$ block (**Figure 47**B), supporting the proposed binding mode.

Second Binding Stage ([**A**] = 6.18 to 9.00 mM**):** Beyond the critical point at 6.00 mM (where the cationic sites are saturated), additional **A**$_n$ began to bind the neutral **P**$_{90}$ block. In this range, only proton signals associated with the **P**$_{90}$ segment underwent significant chemical shift changes (**Figure 47**A), indicating that the excess **A**$_n$ species now interacted with the neutral domain of the copolymer. In detail, NOESY 2D plot of the 15**A**-15**PT**$_{60}$-**P**$_{90}$ DCL showed a major correlation between **A**$_n$ and H$_g$ (**Figure 47**C).

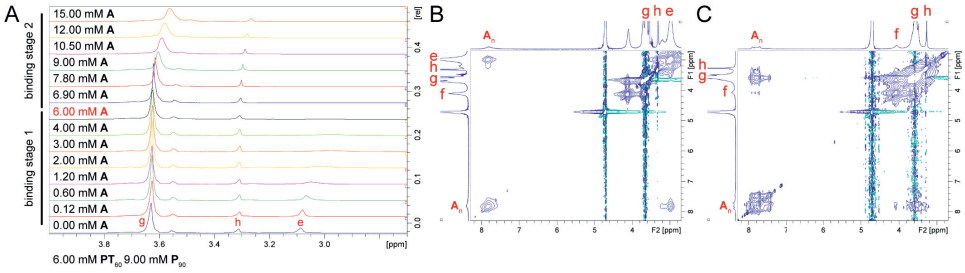

Figure 47 (A) ^{1}H NMR spectra of the *x***A**-15**PT**$_{60}$-**P**$_{90}$ DCLs. ^{1}H-^{1}H NOESY 2D plot of sample (B) 3**A**-15**PT**$_{60}$-**P**$_{90}$ DCL and (C) 15**A**-15**PT**$_{60}$-**P**$_{90}$ DCL. The samples were dissolved in deuterated phosphate buffer at pD 7.4 and measured at 298 K, 600 MHz. From original publication IV.

3.3.3 Multi-stage self-assembly at different binding stages

As the amount of **A**$_n$ increased, three stages of self-assembly were observed: (1) Janus single-chain nanoparticles (Janus-SCNPs), (2) polymeric micelles/vesicles, and (3) fused polymersomes.

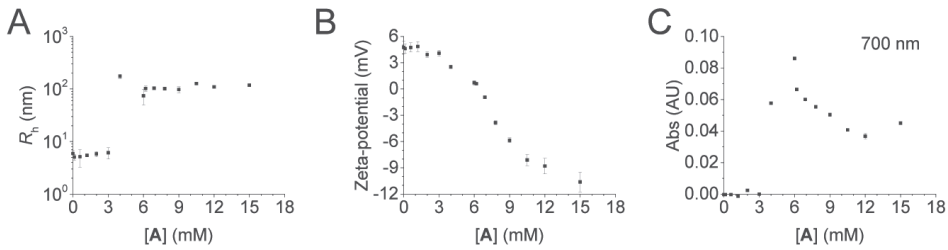

Figure 48 Number-averaged R_h determined by DLS analysis (A), Zeta potential (B), and turbidity obtained from UV-Vis spectra (C) of the *x***A**-15$\mathbf{PT}_{60}$-$\mathbf{P}_{90}$ DCLs. From original publication IV.

Stage 1: Janus-SCNP to Polymer Micelle/Vesicle Transition

Initially, when $\mathbf{A}_n$ concentration was below 3 mM, the number-averaged R_h measured by DLS remained below 10 nm, and the zeta-potential was slightly positive (~+4 mV) (**Figure 48**A and B). This size was not substantially larger than that of free $\mathbf{PT}_{60}$-$\mathbf{P}_{90}$, indicating that the assembly remained at the single-chain level. Since $\mathbf{A}_n$ bound only to the cationic $\mathbf{PT}_{60}$ block at this stage, the resulting structure can be described as a Janus-SCNP, well-solvated and transparent (no significant turbidity increase). TEM image of the 3**A**-15$\mathbf{PT}_{60}$-$\mathbf{P}_{90}$ DCL revealed tadpole-like nanoparticles with longitudinal dimensions of 20–100 nm, a typical morphology for Janus-SCNPs (**Figure 49**A).

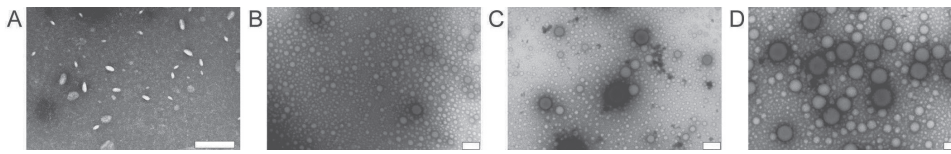

Figure 49 TEM images of 3**A**-15$\mathbf{PT}_{60}$-$\mathbf{P}_{90}$ DCL (A), 6**A**-15$\mathbf{PT}_{60}$-$\mathbf{P}_{90}$ DCL (B), 9**A**-15$\mathbf{PT}_{60}$-$\mathbf{P}_{90}$ DCL (C), 12**A**-15$\mathbf{PT}_{60}$-$\mathbf{P}_{90}$ DCL (D). Scale bar = 200 nm. From original publication IV.

As $\mathbf{A}_n$ concentration increased beyond 3 mM, the R_h rose sharply to 50–200 nm, accompanied by a near-neutral zeta-potential when [$\mathbf{A}_n$] reached 6 mM (**Figure 48**A and B), where the cationic and anionic charges were approximately balanced. Under these conditions, the NMR signals from both $\mathbf{A}_n$ and the cationic $\mathbf{PT}_{60}$ block disappeared (**Figure 47**A), suggesting the formation of a neutral complex. Enhanced turbidity indicated aggregation into larger structures (**Figure 48**C). TEM images in this range showed polymer micelles/vesicles (**Figure 49**B). Thus, by the end of the first binding stage (at neutralization), the self-assembly transitioned from Janus-SCNPs to polymeric micelles/vesicles.

Stage 2: Polymersome Formation and Fusion

In the second binding stage, when $\mathbf{A}_n$ concentration exceeded the saturation point for the $\mathbf{PT}_{60}$ block, additional $\mathbf{A}_n$ began interacting with the neutral $\mathbf{P}_{90}$ block. Interestingly, although the number-averaged R_h did not change significantly, the turbidity decreased as more $\mathbf{A}_n$ was introduced, and the zeta-potential shifted increasingly into the negative range (**Figure 48**B). TEM revealed larger polymersomes as the $\mathbf{A}_n$ concentration rose (**Figure 49**B-D), confirming that $\mathbf{A}_n$ addition induced fusion of the polymersomes, reducing the number of separate vesicles and thus lowering turbidity.

However, this observation appears counterintuitive: increased negative zeta-potential typically enhances colloidal stability by increasing interparticle repulsion, which should oppose fusion. The simultaneous increase in zeta-potential and enhanced fusion suggests that the interplay between polymer dynamics and DCM binding in this system introduces an unconventional mechanism of self-assembly control.

3.3.4 Characterizing the interplay between polymer dynamics and DCMs that induced the multi-stage self-assembly

3.3.4.1 Conformational dynamics for the formation of Janus-SCNP

Before half-neutralization in the first binding stage, self-assembly was mediated primarily by conformational dynamics, as discussed previously. To investigate these dynamics, we conducted DOSY and T_2 measurements on the 2**A**-15$\mathbf{PT}_{60}$-$\mathbf{P}_{90}$ DCL to assess the behavior of the $\mathbf{PT}_{60}$-$\mathbf{P}_{90}$ copolymer template (**Figure 50**A).

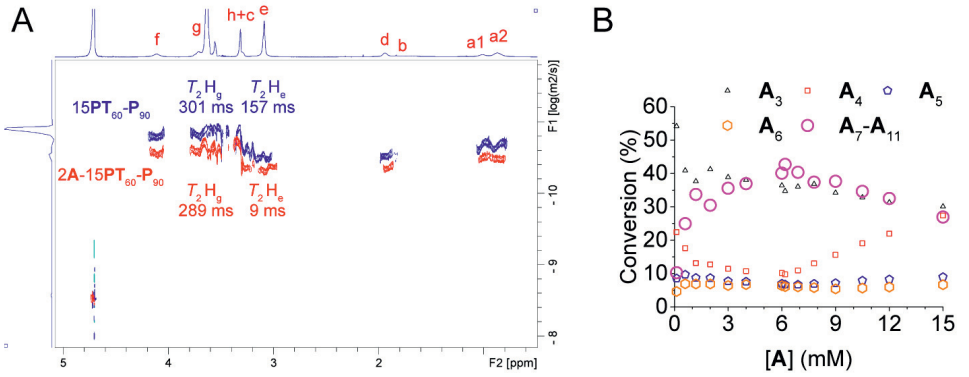

Figure 50 (A) Parallel comparison of DOST 2D plots and T_2 values between the 15**PT**$_{60}$-**P**$_{90}$ control sample and 2**A**-15**PT**$_{60}$-**P**$_{90}$ DCL. ^{1}H NMR spectrum in the F2 dimension is for qualitative localization of the 2D signals. Experiments were at 298 K and 600 MHz. (B) Conversion of **A** to different **A**$_n$ species of the *x***A**-15**PT**$_{60}$-**P**$_{90}$ DCLs determined by HPLC analysis. From original publication IV.

DOSY results showed that **PT**$_{60}$-**P**$_{90}$ exhibited a larger D (or smaller R_h) in the presence of **A**$_n$ compared to its free form (**Figure 50**A), confirming the polymer's folding. Further T_2 analysis revealed that only the cationic **PT**$_{60}$ block underwent significant folding (**Figure 50**A): in 2**A**-15**PT**$_{60}$-**P**$_{90}$, the T_2 of H_g in the **P**$_{90}$ block decreased by only about 4–10% relative to free **PT**$_{60}$-**P**$_{90}$, whereas the T_2 of H_e in the **PT**$_{60}$ block decreased by approximately 94%. Since only the cationic **PT**$_{60}$ block was bound by **A**$_n$ in this stage, these results indicate that **A**$_n$ selectively drives the folding of the **PT**$_{60}$ domain, leaving the **P**$_{90}$ domain largely unaffected and unbound.

3.3.4.2 Conformational dynamics initiate entropy-driven formation of polymer micelle/vesicle

Once the degree of neutralization passes the halfway mark in the first binding stage, entropy begins to influence the self-assembly of Janus-SCNPs into polymeric micelles/vesicles. As more **A**$_n$ is introduced, enhanced hydrophobic complexation occurs within the **PT**$_{60}$ block, evidenced by increasing **A**$_7$-**A**$_{11}$ and decreasing **A**$_3$ and **A**$_4$ conversions from HPLC analysis (**Figure 50**B). In earlier sections, **A**$_7$-**A**$_{11}$ were identified as contributing to hydrophobic cores, while **A**$_3$ and **A**$_4$ formed more hydrophilic shells.

The shift in DCM composition leads to an increase in hydrophobicity within the **PT**$_{60}$ block, imposing a penalty on solvation entropy. In response, the system reconfigures: the hydrophobic segments become hidden within the assembly's interior, while the hydrophilic **P**$_{90}$ segments remain more exposed. ^{1}H NMR spectra confirm this rearrangement (**Figure 47**A), showing loss of **PT**$_{60}$ signals but persistent

bound-free signals from the $\mathbf{P}_{90}$ block, consistent with micelle/vesicle structures that minimize solvation entropy.

3.3.4.3 Kinetic intermediate of DCMs initiate the polymersome fusion against enhanced interparticle repulsion

In the second binding stage, as $\mathbf{A}_n$ concentration exceeds the full neutralization point, additional $\mathbf{A}_n$ binds to the neutral $\mathbf{P}_{90}$ block on the micelles/vesicles (**Figure 47**A, **Figure 48**C, **Figure 49**B-D), facilitating their fusion into larger polymersomes. Surprisingly, as more $\mathbf{A}_n$ is added, the zeta-potential becomes increasingly negative (**Figure 48**B), enhancing electrostatic repulsion between particles. Such repulsion typically hinders fusion in equilibrium systems, making this behavior unusual and significant.

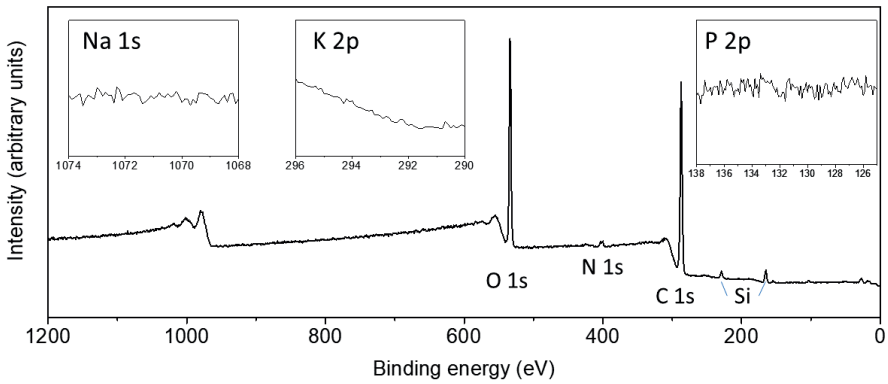

Figure 51 XPS analysis of the powder sample of fused polymersome showing its elemental composition, full spectrum and zoomed insets of Na 1s, K 2p, and P 2p. From original publication IV.

In biological contexts, cell fusion—an essential process for intercellular communication—must also overcome strong electrostatic repulsion between negatively charged cell surfaces[155, 156]. Cells achieve this by employing SNARE (soluble N-ethylmaleimide-sensitive-factor attachment protein receptor) proteins to build essential kinetic intermediates for facilitating membrane fusion over the kinetic barrier of charge repulsion[157]. Similarly, we identified a kinetic intermediate—free **A** (prior to oxidation)—that interacts with both cationic and neutral blocks to overcome the repulsive barrier and promote fusion.

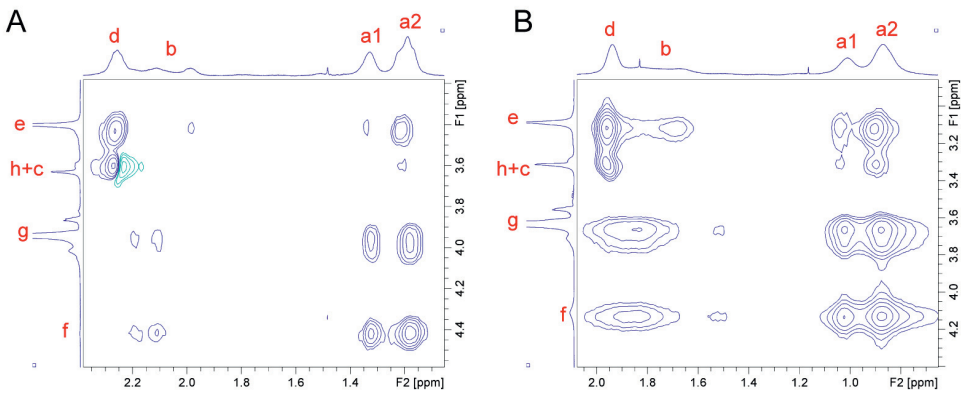

Figure 52 ^{1}H-^{1}H NOESY 2D plot of 5 mM **PT**$_{60}$-**P**$_{90}$ (A) and 15 mM **PT**$_{60}$-**P**$_{90}$ (B). NOESY was operated at 298 K, 600 MHz. From original publication IV.

First, we confirmed that salts did not contribute to the fusion process. X-ray photoelectron spectroscopy (XPS) analysis of fused polymersomes in the 18**A**-15**PT**$_{60}$-**P**$_{90}$ DCL revealed no detectable K, Na, or P elements (**Figure 51**). Since only KH_2PO_4 and NaOH were used to prepare the buffer, the absence of these elements in the polymersome indicates that salts did not alleviate charge repulsion.

We then examined the role of polymer concentration on inter-polymer interactions. Without added **A**$_n$, a 15 mM **PT**$_{60}$-**P**$_{90}$ solution showed significant NOE correlations between the neutral and cationic blocks, implying inter-chain interactions (**Figure 52**). At a lower concentration of 5 mM **PT**$_{60}$-**P**$_{90}$ (2 mM **PT**$_{60}$ pendants and 3 mM **P**$_{90}$ pendants), NOESY experiments revealed no such interactions, confirming an inter-polymer-interaction-free state (**Figure 52**). Another set of DCLs (*x***A**-5**PT**$_{60}$-**P**$_{90}$) was then prepared by varying **A**$_n$ concentrations from 2 to 18 mM at 5 mM **PT**$_{60}$-**P**$_{90}$. Even without pre-existing inter-polymer interactions, these samples still underwent fusion, as confirmed by turbidity changes, the formation of opaque samples, and TEM images at higher **A**$_n$ concentrations (**Figure 53**A-D). Thus, pre-existing inter-chain interactions were not essential for fusion.

To identify the critical step in the fusion process, we conducted kinetic monitoring of molecular interactions during DCL equilibration. From NOESY 2D plot (**Figure 53**E), we observed that native (reduced) **A**—before oxidation—interacted with both the cationic **PT**$_{60}$ and neutral **P**$_{90}$ blocks. Upon oxidation to **A**$_n$ mixtures, the interaction remained only between **A**$_n$ and the cationic **PT**$_{60}$ block, which rapidly formed stronger hydrophobic assemblies upon further increasing of n and made signals unobservable. This suggests that the primary fresh **A** is the crucial kinetic intermediate enabling fusion, as it alone can interact simultaneously with both blocks.

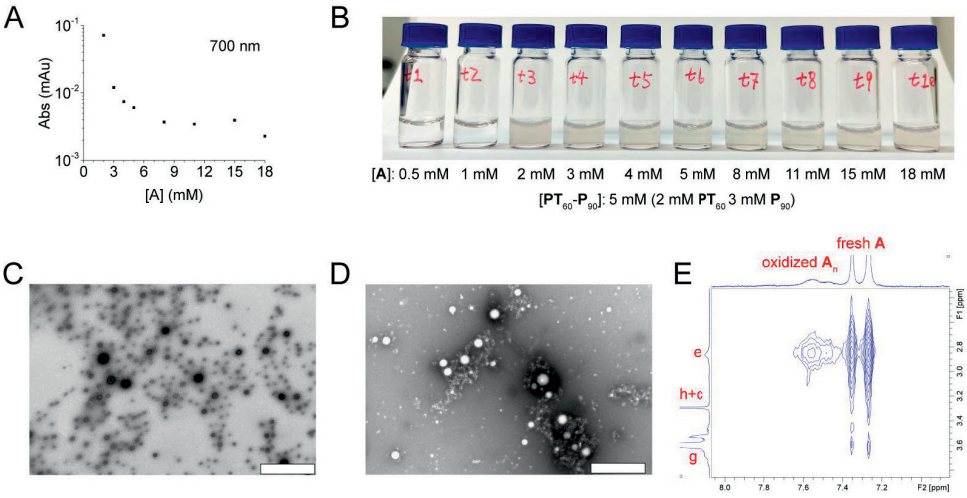

Figure 53 Turbidity measurement (A) and visual appearance (B) of the *x***A**-5**PT**$_{60}$-**P**$_{90}$ DCLs. TEM images of the 5**A**-5**PT**$_{60}$-**P**$_{90}$ DCL (C) and 18**A**-5**PT**$_{60}$-**P**$_{90}$ DCL (D). (E) ^{1}H-^{1}H NOESY 2D plot of the 5**A**-5**PT**$_{60}$-**P**$_{90}$ at the beginning of the sample preparation before full oxidation. Experiment was operated at 298 K and 600 MHz. From original publication IV.

To verify this, we prepared another set of DCLs (*x***A**$_n$-5**PT**$_{60}$-**P**$_{90}$) by directly mixing **PT**$_{60}$-**P**$_{90}$ with pre-oxidized **A**$_n$ species in the absence of free **A**. According to the turbidity measurements and visual appearance, these samples remained transparent and stable, showing no fusion or aggregation (**Figure 54**A and B). TEM further confirmed steady self-assemblies below 100 nm (**Figure 54**C and D). Reintroducing 1 mM free **A** into an equilibrated 5**A**$_n$-5**PT**$_{60}$-**P**$_{90}$ solution induced an uprised turbidity at the new equilibrium (**Figure 54**E), which indicated the newly introduced free **A** initiated the fusion. Further introducing 1 mM free **A** and equilibrating the sample again would decrease the turbidity (**Figure 54**E), suggesting a continued enhancement on the fusion. Conversely, adding dithiothreitol (DTT) to the no-fusion 5**A**$_n$-5**PT**$_{60}$-**P**$_{90}$ solution did not affect their self-assembly state, as shown by un-changed turbidity (**Figure 54**E). This is probably due to newly produced **A** by reducing via DTT was readily and strongly trapped in the polymer micelle/vesicle, unable to meditate inter-self-assembly interactions. Whereas the newly introduced **A** was not kinetically trapped in the beginning, allowing for itself to interact with multiple self-assemblies and mediate polymersome fusion.

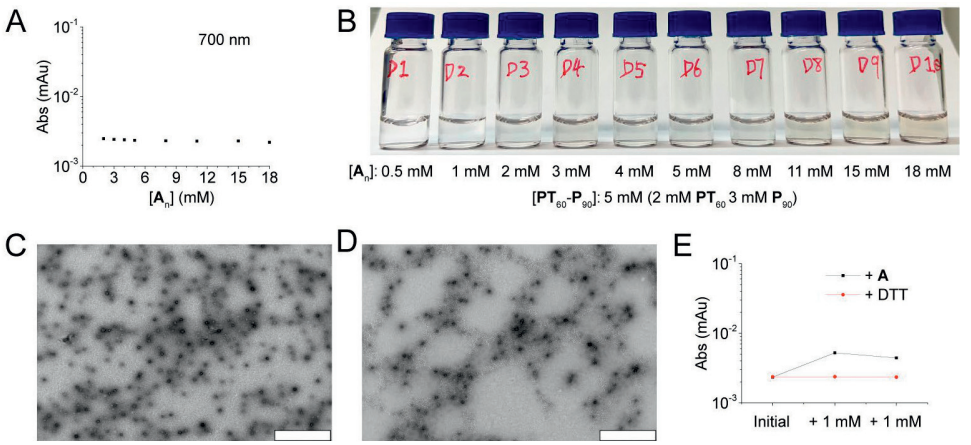

Figure 54 Turbidity measurement (A) and visual appearance (B) of the $x\mathbf{A}_n$-5$\mathbf{PT}_{60}$-$\mathbf{P}_{90}$ DCLs. TEM images of the 5$\mathbf{A}_n$-5$\mathbf{PT}_{60}$-$\mathbf{P}_{90}$ DCL (C) and 18$\mathbf{A}_n$-5$\mathbf{PT}_{60}$-$\mathbf{P}_{90}$ DCL (D). (E) Free thiol addition experiment to the 5$\mathbf{A}_n$-5$\mathbf{PT}_{60}$-$\mathbf{P}_{90}$ DCL, measured by the turbidity tests. Each time, 1 mM fresh **A** or DTT was added to the pre-equilibrated DCLs, and turbidity values at the equilibriums were recorded. From original publication IV.

In summary, the presence of fresh **A** as a kinetic intermediate is necessary to overcome the electrostatic barrier and facilitate polymersome fusion. By interacting with both the cationic and neutral blocks at the inter-chain level, **A** enables the system to mimic biological fusion processes despite heightened charge repulsion.

3.3.4.4 Fusion's feedback to DCMs on the hydrodynamic interface

In biological systems, the fusion of biological membranes usually works as a trigger to bring downstream alterations to the system[155, 156]. Thus, having unraveled the mechanism behind polymersome fusion, we next investigated how the polymersome fusion brought feedback to the DCMs of $\mathbf{A}_n$.

In x**A**-5$\mathbf{PT}_{60}$-$\mathbf{P}_{90}$ (fusion) or $x\mathbf{A}_n$-5$\mathbf{PT}_{60}$-$\mathbf{P}_{90}$ (no fusion) DCLs—irrespective of whether fusion occurred—$\mathbf{A}_4$ was progressively amplified during the second binding stage as binding intensified. HPLC analyses showed similar amplification profiles in both sets of DCLs (**Figure 55**A-C). However, in the fusion DCLs, there was a less $\mathbf{A}_4$ amplification at the enhanced consumption of $\mathbf{A}_7$- $\mathbf{A}_{11}$ once [$\mathbf{A}_n$] exceeded 8 mM.

To elucidate this feedback mechanism, first we confirmed $\mathbf{A}_4$ was amplified to compensate for the binding-induced penalty on conformational entropy by its enhanced motional dynamics at bound state, as established in Section 3.2. Indeed, in both x**A**-5$\mathbf{PT}_{60}$-$\mathbf{P}_{90}$ and $x\mathbf{A}_n$-5$\mathbf{PT}_{60}$-$\mathbf{P}_{90}$ DCLs, $\mathbf{A}_4$ had much higher T_2 than $\mathbf{A}_3$, and the T_2 of $\mathbf{A}_4$ increased more sensitively than $\mathbf{A}_3$ along with the decreased T_2 of H_g (**Figure 55**D-F), confirming the entropy-driven amplification of the entropy compensator of $\mathbf{A}_4$.

Under this amplification mechanism, we continued to investigate the reason for the amplification change of $\mathbf{A}_4$. We noticed that, over [**A**] = 8 mM where the fusion started to present feedback to DCMs, there was less decrease of T_2 of H_g in the fusion samples (**Figure 55**F), which might posit less requirements to amplify $\mathbf{A}_4$ for entropy compensation. In addition, in the fusion samples, the T_2 of $\mathbf{A}_4$ was largely less than that of the no-fusion samples, suggesting a more restricted molecular motion of $\mathbf{A}_4$ upon fusion. As we had proved that the enhanced motional dynamics of $\mathbf{A}_4$ was benefited from its binding mode that was more associated with the water swollen in the polymer framework, and polymersome fusion could sequester more water out of the self-assembly, $\mathbf{A}_4$ could be less dynamic in a less hydrated fused polymersome.

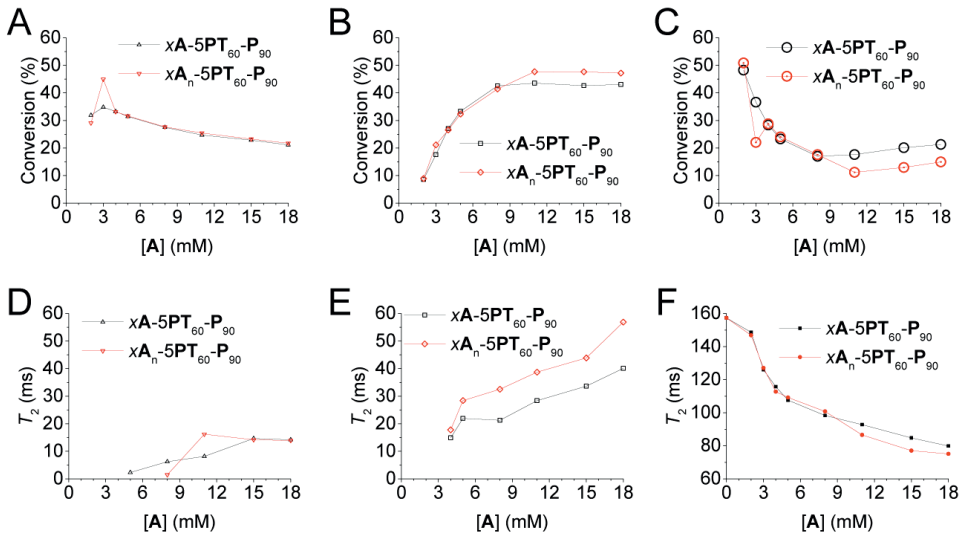

Figure 55 Conversion of **A** to $\mathbf{A}_3$ (A), $\mathbf{A}_4$ (B), and $\mathbf{A}_7$- $\mathbf{A}_{11}$ (C) in the *x***A**-5**PT**$_{60}$-**P**$_{90}$ or *x***A**$_n$-5**PT**$_{60}$-**P**$_{90}$ DCLs. T_2 of the $\mathbf{A}_3$ H_1 (D), $\mathbf{A}_4$ H_1 (D), and **PT**$_{60}$-**P**$_{90}$ H_g (D) in the *x***A**-5**PT**$_{60}$-**P**$_{90}$ or *x***A**$_n$-5**PT**$_{60}$-**P**$_{90}$ DCLs. From original publication IV.

Furthermore, polymersome fusion or other types of inter-particle aggregation had been well-known for increasing the solvation entropy by releasing more free solvent molecules[143], which could help compensate the binding-induced conformational entropy penalty and cut down the need for the production of $\mathbf{A}_4$. Moreover, the fused polymersome brought their bound $\mathbf{A}_n$ together and enhanced the local concentration of $\mathbf{A}_n$, which amplified $\mathbf{A}_7$- $\mathbf{A}_{11}$ under the Le Chatelier's principle.

In conlude, the kinetic pathway of $\mathbf{A}_n$ synthesis drove the polymersome fusion, which further posited feedback to the $\mathbf{A}_n$ synthesis. Due to dehydration and increased solvation entropy caused by fusion, the amplification of $\mathbf{A}_4$ was decreased. And the

enhanced local concentration of $\mathbf{A}_n$ upon fusion pushed more production of $\mathbf{A}_7$- $\mathbf{A}_{11}$ under the Le Chatelier's principle.

3.3.5 Conclusion

(1) Two distinct binding stages were observed as the $\mathbf{A}_n$ concentration ([$\mathbf{A}_n$]) increased relative to the cationic $\mathbf{PT}_{60}$ block concentration ([$\mathbf{PT}_{60}$]). When [$\mathbf{A}_n$] < [$\mathbf{PT}_{60}$], all An species preferentially bound to the cationic $\mathbf{PT}_{60}$ block, defining the first binding stage. As [$\mathbf{A}_n$] surpassed [$\mathbf{PT}_{60}$], all additional $\mathbf{A}_n$ bound to the neutral $\mathbf{P}_{90}$ block, marking the onset of the second binding stage.

(2) Within the first binding stage and before half-charge neutralization, the self-assembly formed Janus single-chain nanoparticles (Janus-SCNPs), driven by conformational dynamics. After half-charge neutralization, the emerging excess hydrophobic interactions prompted by increased $\mathbf{A}_n$ loading led to the formation of polymeric micelles or polymersomes. In this process, hydrophobic segments clustered internally to minimize the penalty on solvation entropy, while the hydrophilic $\mathbf{P}_{90}$ segments remained exposed at the assembly's surface.

(3) In the second binding stage, the fresh **A** species served as a crucial kinetic intermediate to induce polymersome fusion. This intermediate uniquely interacted with both the cationic $\mathbf{PT}_{60}$ block and the neutral $\mathbf{P}_{90}$ block, thereby enabling fusion despite increasing surface charge repulsion (**Figure 56**).

(4) Regardless of whether polymersome fusion occurred, entropy-driven configurational dynamics triggered similar amplification of the $\mathbf{A}_4$ species during the second binding stage. The binding of $\mathbf{A}_n$ imposed a penalty on the conformational entropy of the surface $\mathbf{P}_{90}$ chains, restricting their mobility. To compensate, $\mathbf{A}_4$ was amplified to facilitate more dynamic bound-state motion, thereby increasing the configurational entropy at the interface and maintaining the system's structural adaptability (**Figure 56**).

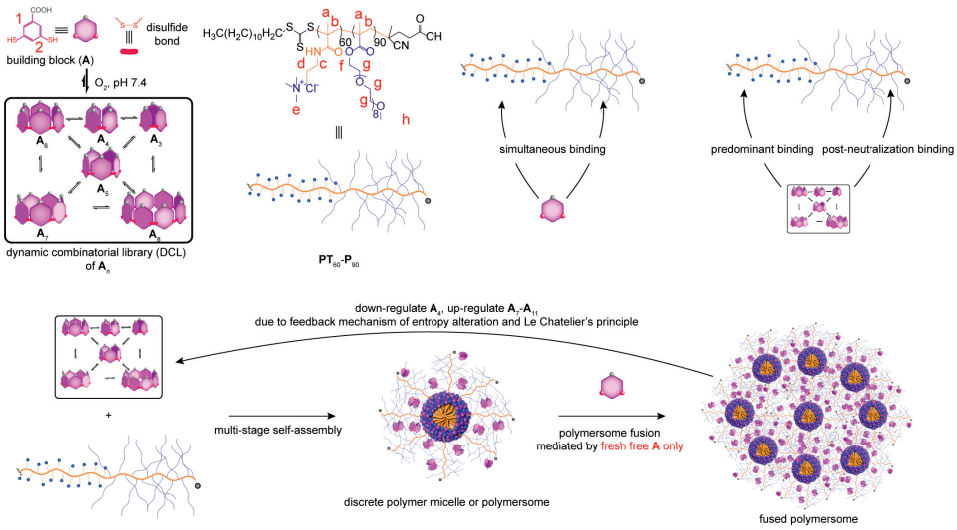

Figure 56 Scheme of the mechanism of controlled polymersome fusion and its feedback to the DCMs' production in the polymersome. The chemical systems were operated in phosphate buffer at pH 7.4, room temperature and atmospheric pressure. From original publication IV.

4 Summary

This thesis established a new scientific paradigm that leverages the intrinsic polymer dynamics of polymeric templates within dynamic combinatorial chemistry (DCC) to achieve greater complexity and novel functional behaviors. The polymeric templates were mixed with dynamic combinatorial libraries of macrocyclic disulfides (DCMs), the polymer-DCMs assembly would then response with different dynamics interactive with the structural transition of DCMs.

In the first part, conformational dynamics were harnessed to realize the first example of single-chain folding mediated by DCMs as non-covalent crosslinkers featuring self-adaptive chemical structures. This demonstrated how subtle modifications in polymer conformation can guide the formation of intricate nanoscale architectures. In comparison, static non-covalent crosslinkers, including a macrocyclic disulfide with static chemical structure regardless the dynamic assembly processes, were less effective to drive the folding.

The second part introduced a new class of DCC driven by entropy-driven configurational dynamics. By constructing an entropic network, it became possible to synthesize polymer–DCMs supramolecular self-assemblies endowed with high configurational entropy and enhanced kinetic energy. This expanded the functional repertoire of DCC, paving the way for materials with greater structural variability and responsiveness.

Finally, in the third part, the two dynamics identified above—conformational and entropic—were integrated into a single chemical system. This integration enabled crosstalk between distinct template-driven dynamics and unveiled a new mechanism for polymersome fusion. The ability to combine multiple dynamic processes within one system opens the door to more complex, life-like behavior in synthetic chemical assemblies.

Together, these findings highlight the potential of polymeric templates to introduce new dynamic dimensions into DCC, ultimately fostering the emergence of advanced functionalities and complex, adaptive materials.

Acknowledgements

The biggest thanks to my supervisor Dr. Jianwei Li. You offered me the strongest support to my study and life in Turku. Your motivation and patience to me made my PhD study a joyful experience. It was from you that I learnt how to conduct high-quality scientific research in all aspects. Most importantly, you offered me the envaluable opportunities to exercise my research ideas, communicate with the giants (including you) and learning new things that I was interested. I hope the very best and happy life for you and your lovely family

I deeply appreciate my supervisor Dr. Sirpa Jalkanen. Besides your important help to my cell experiments, your advice is largely pivotal for my research and career development. Your leadership and mentorship not only facilitated a fantastic and lovely research environment for us in the Medicity research laboratory, but also set up a great example for us on being an excellent scientist and leader.

I'm so happy and thankful to have my follow-up committee, Dr. Jianwei Li, Dr. Sirpa Jalkanen, Dr. Jing Tang. Your insightful questions, comments, motivations, and suggestions in each meeting could always make my up-coming study clearer and initiate the many important improvements.

My sincere respect and gratitude to my senior colleagues Dr. Yu Cao and Dr. Jingjing Yu. I could not have such a great kick-start in the lab without you. You warmly and patiently teached me solid practical skills and passed me your precious research experiences in organic chemistry and supramolecular chemistry, from the most basic things to every single detail you could recall.

I greatly appreciate Dr. Jani Rahkila, Tuomas Niemi-Aro, and Dr. Perttu Permi for your solid support and passing me many precious knowledge in NMR application, which are indispensable for the smooth development of my research and carreer.

Many thanks to Markus Peurla, I learnt from you the very important TEM skills, especially negative staining. These skills helped me to have reliable insights to the many interesting events happened in the nano-micro world.

I express my gratitude whole-heartly to Dr. Ermei Mäkilä, Dr. Sari Granroth, Dr. Ville Liljeström, Xun Sun, Dr. Jinghui Luo, Dr. Xue Zhang, Dr. Leena Pitkänen, Dr. Jessica Rosenholm, and Dr. Lippo Lassila, for your friendly and strong support on many characterization techniques, including SEM, DSC, TGA, XPS, SAXS, AFM,

SEC, DLS, and Rheometry. The quality of my research had been assured with the help from your excellent expertise.

It was a wonderful experience to tackle the mass photometry characterization together with Dr. Anastassios (Tassos) C. Papageorgiou. Thank you Tassos, you're always there to help us with your warm support.

Thank you John for being our lovely friend and technician in Medicity. I wish you the very best for your wonderful and peaceful life after retirement.

A lot of thanks goes to Jiaoyan Xu, Dr. Hongyi Xu and Dr. Xiaodong Zou for hosting our research collaboration in the Stockholm University. It was an exciting experience to cooperate with you on the research project to resolve the structure of drug-loading nano assembly. I opened my eyes in the many powerful EM and ED techniques and many important inter-sections between chemistry and physics.

Thank you Dr. Yonglei Lyu for introducing this great PhD opportunity to me.

Many respect and thanks to Jinghui Yang, we had been rest assured with your reliable maintenance to many important lab equipments, most importantly all the LC systems. Without you, our research would be much harder and slower as there had always been some issues in those delicate machines. I wish you and your wife Xin Wang a lovely and happy future life.

Thank you Chong Chen for serving me your top-level cooking, however I think you can still catch up with chef Jinghui Yang. I hope you can graduate very soon and find your dream job.

Many respect to Dr. Xiaoxia Wu for your outstanding working ethnics that sets a very good example for us.

Great thanks to Dr. Qing Li for carrying our basketball games, you were the Michael Jordan in Turku.

A lot of thanks to Dr. Jian Yang for encouraging me in the beginning of my PhD study, and many interesting research collaborations and discussions.

Thank you very much Ferdinand Holzhausen for trusting me and working with me for your internship. It was my great pleasure to be your internship host, which was a happy and fruitful experience. We learnt from each other in many aspects and together took remarkable progress in hiking and research work.

During my participation to research conferences and schools, I was deeply thankful to discuss about my research projects with Dr. Sijbren Otto, Dr. E. W. Meijer, Dr. Hector Martinez-Seara Monne, and Nobel laureate Dr. Sir James Fraser Stoddart. Your insightful and critical questions and comments truly opened my mind and helped me to take the research to the next level. From these communications, I deepened my understanding that the research quality is originally about the quality of the research questions throughout the research process.

I'm thankful to have my very important "non-research-related" friends during my PhD study: Bojun Li, Honghao Du, Dr. Jie Li, Jiaming Wang, Dr. Shufan Fei,

Jinglu Chen, Yu Guo, Xiaoyu Hu, Yaohan Xu, Zhaodong Yin, Yufei Xu, Ligui Wang, Dr. Lili Li, Asuka Toyofuku, Jalmari Polari, Dr. Elmeri Jokinen, Yangyang Zhao, Dr. Mengyuan Xiong, Dr. Zelin (Wei) Zhang, Zhe Yu, Dr. Kang Chen, Dr. Shuxun Liu,

How lucky I am to have such a great and strong friendship with Xuncheng. You're always there to support me, and the trust between us is so precious. We had together been through a lot envaluable and unforgettable experiences in both study and life.

My life is happy in Turku because I have my lovely girl friend Caihong. The winter is not dark nor cold because of your love and support. Any written or spoken word can never fully express how great the happiness is when you're with me.

I'm blessed to have my beloved and lovely family. My mother Jun Wang, father Defeng Qi, uncle Deyu Qi, aunt Xiulian He, grandpa Yuting Wang and Zhizhong Qi, grandma Shulan Guan and Qiaoe Guo, and many other dear family members. It has been always your love and support that helped to build my mental strength and happy life during my growing up. I wish you the best for your happiness, health, and peace.

Whatever the good things I got, publications, degrees, or anything else, is only one kind of reflection of the beautiful connection between me and all the lovely people that be with me, love me, and support me. I'm thankful that I have been greatly loved and blessed in this wonderful world. Hence, whatever I do, should be dedicated to bring happy and healthy life to the people, which is the most important task in the end.

20250117
Dawei Qi
齐大卫

References

(1) Lehn, J.-M.; Eliseev, A. V. Dynamic Combinatorial Chemistry. *Science* **2001**, *291* (5512), 2331-2332.

(2) Corbett, P. T.; Leclaire, J.; Vial, L.; West, K. R.; Wietor, J.-L.; Sanders, J. K. M.; Otto, S. Dynamic Combinatorial Chemistry. *Chemical Reviews* **2006**, *106* (9), 3652-3711.

(3) Reek, J. N.; Otto, S. *Dynamic combinatorial chemistry*; John Wiley & Sons, 2010.

(4) Cougnon, F. B. L.; Sanders, J. K. M. Evolution of Dynamic Combinatorial Chemistry. *Accounts of Chemical Research* **2012**, *45* (12), 2211-2221.

(5) Moulin, E.; Cormos, G.; Giuseppone, N. Dynamic combinatorial chemistry as a tool for the design of functional materials and devices. *Chemical Society Reviews* **2012**, *41* (3), 1031-1049.

(6) Frei, P.; Hevey, R.; Ernst, B. Dynamic Combinatorial Chemistry: A New Methodology Comes of Age. *Chemistry – A European Journal* **2019**, *25* (1), 60-73.

(7) Ludlow, R. F.; Otto, S. Systems chemistry. *Chemical Society Reviews* **2008**, *37* (1), 101-108, 10.

(8) Li, J.; Nowak, P.; Otto, S. Dynamic Combinatorial Libraries: From Exploring Molecular Recognition to Systems Chemistry. *Journal of the American Chemical Society* **2013**, *135* (25), 9222-9239.

(9) Mattia, E.; Otto, S. Supramolecular systems chemistry. *Nature Nanotechnology* **2015**, *10* (2), 111-119.

(10) Ashkenasy, G.; Hermans, T. M.; Otto, S.; Taylor, A. F. Systems chemistry. *Chemical Society Reviews* **2017**, *46* (9), 2543-2554.

(11) Das, K.; Gabrielli, L.; Prins, L. J. Chemically Fueled Self-Assembly in Biology and Chemistry. *Angewandte Chemie International Edition* **2021**, *60* (37), 20120-20143.

(12) Das, K.; Chen, R.; Chandrabhas, S.; Gabrielli, L.; Prins, L. J. Design of Chemical Fuel-Driven Self-Assembly Processes. In *Out-of-Equilibrium (Supra)molecular Systems and Materials*, 2021; pp 191-213.

(13) Ji, Q.; Lirag, R. C.; Miljanić, O. Š. Kinetically controlled phenomena in dynamic combinatorial libraries. *Chemical Society Reviews* **2014**, *43* (6), 1873-1884.

(14) Chen, X.; Würbser, M. A.; Boekhoven, J. Chemically Fueled Supramolecular Materials. *Accounts of Materials Research* **2023**, *4* (5), 416-426.

(15) van Esch, J. H.; Klajn, R.; Otto, S. Chemical systems out of equilibrium. *Chemical Society Reviews* **2017**, *46* (18), 5474-5475.

(16) Le Chatelier, H. L. J. C. R. A. d. S. Sur un énoncé général des lois des équilibres chimiques. **1884**, *99*, 786-789.

(17) De Heer, J. The principle of Le Châtelier and Braun. *Journal of Chemical Education* **1957**, *34* (8), 375.

(18) Jia, C.; Qi, D.; Zhang, Y.; Rissanen, K.; Li, J. Strategies for Exploring Functions from Dynamic Combinatorial Libraries. *ChemSystemsChem* **2020**, *2* (5), e2000019.

(19) Hartman, A. M.; Gierse, R. M.; Hirsch, A. K. H. Protein-Templated Dynamic Combinatorial Chemistry: Brief Overview and Experimental Protocol. *European Journal of Organic Chemistry* **2019**, *2019* (22), 3581-3590.

(20) Canal-Martín, A.; Pérez-Fernández, R. Protein-Directed Dynamic Combinatorial Chemistry: An Efficient Strategy in Drug Design. *ACS Omega* **2020**, *5* (41), 26307-26315.
(21) Saha, P.; Panda, D.; Dash, J. Nucleic acids as templates and catalysts in chemical reactions: target-guided dynamic combinatorial chemistry and in situ click chemistry and DNA/RNA induced enantioselective reactions. *Chemical Society Reviews* **2023**, *52* (13), 4248-4291.
(22) Brisig, B.; Sanders, J. K. M.; Otto, S. Selection and Amplification of a Catalyst from a Dynamic Combinatorial Library. *Angewandte Chemie International Edition* **2003**, *42* (11), 1270-1273.
(23) Dydio, P.; Breuil, P.-A. R.; Reek, J. N. H. Dynamic Combinatorial Chemistry in Chemical Catalysis. *Israel Journal of Chemistry* **2013**, *53* (1-2), 61-74.
(24) Iwasawa, N.; Ono, K. 3D-Boronic Ester Architectures: Synthesis, Host-Guest Chemistry, Dynamic Behavior, and Supramolecular Catalysis. *The Chemical Record* **2022**, *22* (1), e202100214.
(25) Mullins, A. G.; St. Louis, L. E.; Waters, M. L. Using changes in speciation in a dynamic combinatorial library as a fingerprint to differentiate the methylation states of arginine. *Chemical Communications* **2020**, *56* (28).
(26) Harrison, E. E.; Carpenter, B. A.; St. Louis, L. E.; Mullins, A. G.; Waters, M. L. Development of "Imprint-and-Report" Dynamic Combinatorial Libraries for Differential Sensing Applications. *Journal of the American Chemical Society* **2021**, *143* (36), 14845-14854.
(27) Harrison, E. E.; Waters, M. L. Application of an Imprint-and-Report Sensor Array for Detection of the Dietary Metabolite Trimethylamine N-Oxide and Its Precursors in Complex Mixtures. *Angewandte Chemie International Edition* **2022**, *61* (33), e202205193.
(28) Harrison, E. E.; Waters, M. L. Detection and differentiation of per- and polyfluoroalkyl substances (PFAS) in water using a fluorescent imprint-and-report sensor array. *Chemical Science* **2023**, *14* (4), 928-936.
(29) Otto, S.; Furlan, R. L. E.; Sanders, J. K. M. Selection and Amplification of Hosts From Dynamic Combinatorial Libraries of Macrocyclic Disulfides. *Science* **2002**, *297* (5581), 590-593.
(30) Corbett, P. T.; Otto, S.; Sanders, J. K. M. Correlation between Host–Guest Binding and Host Amplification in Simulated Dynamic Combinatorial Libraries. *Chemistry – A European Journal* **2004**, *10* (13), 3139-3143.
(31) Ferguson Johns, H. P.; Harrison, E. E.; Stingley, K. J.; Waters, M. L. Mimicking Biological Recognition: Lessons in Binding Hydrophilic Guests in Water. *Chemistry – A European Journal* **2021**, *27* (22), 6620-6644.
(32) Ingerman, L. A.; Cuellar, M. E.; Waters, M. L. A small molecule receptor that selectively recognizes trimethyl lysine in a histone peptide with native protein-like affinity. *Chemical Communications* **2010**, *46* (11), 1839-1841.
(33) James, L. I.; Beaver, J. E.; Rice, N. W.; Waters, M. L. A Synthetic Receptor for Asymmetric Dimethyl Arginine. *Journal of the American Chemical Society* **2013**, *135* (17), 6450-6455.
(34) E. Beaver, J.; C. Peacor, B.; V. Bain, J.; James, L. I.; L. Waters, M. Contributions of pocket depth and electrostatic interactions to affinity and selectivity of receptors for methylated lysine in water. *Organic & Biomolecular Chemistry* **2015**, *13* (11), 3220-3226.
(35) Pinkin, N. K.; Liu, I.; Abron, J. D.; Waters, M. L. Secondary Binding Interactions in a Synthetic Receptor for Trimethyllysine. *Chemistry – A European Journal* **2015**, *21* (49), 17981-17986.
(36) Pinkin, N. K.; N. Power, A.; Waters, M. L. Late stage modification of receptors identified from dynamic combinatorial libraries. *Organic & Biomolecular Chemistry* **2015**, *13* (44), 10939-10945.
(37) Gober, I. N.; Waters, M. L. Optimization of a synthetic receptor for dimethyllysine using a biphenyl-2,6-dicarboxylic acid scaffold: insights into selective recognition of hydrophilic guests in water. *Organic & Biomolecular Chemistry* **2017**, *15* (37), 7789-7795.
(38) Peacor, B. C.; Ramsay, C. M.; Waters, M. L. Fluorogenic sensor platform for the histone code using receptors from dynamic combinatorial libraries. *Chemical Science* **2017**, *8* (2), 1422-1428.
(39) Mullins, A. G.; Pinkin, N. K.; Hardin, J. A.; Waters, M. L. Achieving High Affinity and Selectivity for Asymmetric Dimethylarginine by Putting a Lid on a Box. *Angewandte Chemie International Edition* **2019**, *58* (16), 5282-5285.

(40) Beeren, S. R.; Sanders, J. K. M. Discovery of Linear Receptors for Multiple Dihydrogen Phosphate Ions Using Dynamic Combinatorial Chemistry. *Journal of the American Chemical Society* **2011**, *133* (11), 3804-3807.
(41) Furlan, R. L. E.; Ng, Y.-F.; Otto, S.; Sanders, J. K. M. A New Cyclic Pseudopeptide Receptor for Li+ from a Dynamic Combinatorial Library. *Journal of the American Chemical Society* **2001**, *123* (36), 8876-8877.
(42) Rauschenberg, M.; Bomke, S.; Karst, U.; Ravoo, B. J. Dynamic Peptides as Biomimetic Carbohydrate Receptors. *Angewandte Chemie International Edition* **2010**, *49* (40), 7340-7345.
(43) Iwasawa, N.; Takahagi, H. Boronic Esters as a System for Crystallization-Induced Dynamic Self-Assembly Equipped with an "On−Off" Switch for Equilibration. *Journal of the American Chemical Society* **2007**, *129* (25), 7754-7755.
(44) Otto, S.; Kubik, S. Dynamic Combinatorial Optimization of a Neutral Receptor That Binds Inorganic Anions in Aqueous Solution. *Journal of the American Chemical Society* **2003**, *125* (26), 7804-7805.
(45) Kubik, S.; Goddard, R.; Otto, S.; Pohl, S.; Reyheller, C.; Stüwe, S. Optimization of the binding properties of a synthetic anion receptor using rational and combinatorial strategies. *Biosensors and Bioelectronics* **2005**, *20* (11), 2364-2375.
(46) Rodriguez-Docampo, Z.; Pascu, S. I.; Kubik, S.; Otto, S. Noncovalent Interactions within a Synthetic Receptor Can Reinforce Guest Binding. *Journal of the American Chemical Society* **2006**, *128* (34), 11206-11210.
(47) Rodriguez-Docampo, Z.; Eugenieva-Ilieva, E.; Reyheller, C.; Belenguer, A. M.; Kubik, S.; Otto, S. Dynamic combinatorial development of a neutral synthetic receptor that binds sulfate with nanomolar affinity in aqueous solution. *Chemical Communications* **2011**, *47* (35), 9798-9800.
(48) Li, J.; Nowak, P.; Otto, S. An Allosteric Receptor by Simultaneous "Casting" and "Molding" in a Dynamic Combinatorial Library. *Angewandte Chemie International Edition* **2015**, *54* (3), 833-837.
(49) Komáromy, D.; Tezcan, M.; Schaeffer, G.; Marić, I.; Otto, S. Effector-Triggered Self-Replication in Coupled Subsystems. *Angewandte Chemie International Edition* **2017**, *56* (46), 14658-14662.
(50) Sluysmans, D.; Stoddart, J. F. The Burgeoning of Mechanically Interlocked Molecules in Chemistry. *Trends in Chemistry* **2019**, *1* (2), 185-197. DOI: 10.1016/j.trechm.2019.02.013.
(51) Han, X.; Liu, G.; Liu, S. H.; Yin, J. Synthesis of rotaxanes and catenanes using an imine clipping reaction. *Organic & Biomolecular Chemistry* **2016**, *14* (44), 10331-10351.
(52) Li, J.; Nowak, P.; Fanlo-Virgós, H.; Otto, S. Catenanes from catenanes: quantitative assessment of cooperativity in dynamic combinatorial catenation. *Chemical Science* **2014**, *5* (12), 4968-4974.
(53) Lyu, Y.; Hu, Y.; Yang, J.; Wang, X.; Li, J. Mutualistic Synthesis from Orthogonal Dynamic Covalent Reactions. *Angewandte Chemie International Edition* **2024**, *63* (44), e202412020.
(54) Jiao, T.; Wu, G.; Zhang, Y.; Shen, L.; Lei, Y.; Wang, C.-Y.; Fahrenbach, A. C.; Li, H. Self-Assembly in Water with N-Substituted Imines. *Angewandte Chemie International Edition* **2020**, *59* (42), 18350-18367.
(55) Belowich, M. E.; Stoddart, J. F. Dynamic imine chemistry. *Chemical Society Reviews* **2012**, *41* (6), 2003-2024.
(56) Yu, J.; Gaedke, M.; Schaufelberger, F. Dynamic Covalent Chemistry for Synthesis and Co-conformational Control of Mechanically Interlocked Molecules. *European Journal of Organic Chemistry* **2023**, *26* (8), e202201130.
(57) Tung, S.-T.; Lai, C.-C.; Liu, Y.-H.; Peng, S.-M.; Chiu, S.-H. Synthesis of a [2]Catenane from the Sodium Ion Templated Orthogonal Arrangement of Two Diethylene Glycol Chains. *Angewandte Chemie International Edition* **2013**, *52* (50), 13269-13272.
(58) Ashbridge, Z.; Fielden, S. D. P.; Leigh, D. A.; Pirvu, L.; Schaufelberger, F.; Zhang, L. Knotting matters: orderly molecular entanglements. *Chemical Society Reviews* **2022**, *51* (18), 7779-7809.
(59) Fielden, S. D. P.; Leigh, D. A.; Woltering, S. L. Molecular Knots. *Angewandte Chemie International Edition* **2017**, *56* (37), 11166-11194.

(60) Lam, R. T. S.; Belenguer, A.; Roberts, S. L.; Naumann, C.; Jarrosson, T.; Otto, S.; Sanders, J. K. M. Amplification of Acetylcholine-Binding Catenanes from Dynamic Combinatorial Libraries. *Science* **2005**, *308* (5722), 667-669.
(61) Au-Yeung, H. Y.; Pantoş, G. D.; Sanders, J. K. M. Dynamic Combinatorial Donor−Acceptor Catenanes in Water: Access to Unconventional and Unexpected Structures. *The Journal of Organic Chemistry* **2011**, *76* (5), 1257-1268.
(62) Au-Yeung, H. Y.; Cougnon, F. B. L.; Otto, S.; Pantoş, G. D.; Sanders, J. K. M. Exploiting donor–acceptor interactions in aqueous dynamic combinatorial libraries: exploratory studies of simple systems. *Chemical Science* **2010**, *1* (5), 567-574.
(63) Au-Yeung, H. Y.; Dan Pantoş, G.; Sanders, J. K. M. Amplifying Different [2]Catenanes in an Aqueous Donor−Acceptor Dynamic Combinatorial Library. *Journal of the American Chemical Society* **2009**, *131* (44), 16030-16032.
(64) Ponnuswamy, N.; Cougnon, F. B. L.; Clough, J. M.; Pantoş, G. D.; Sanders, J. K. M. Discovery of an Organic Trefoil Knot. *Science* **2012**, *338* (6108), 783-785.
(65) Allen, C. D.; Link, A. J. Self-Assembly of Catenanes from Lasso Peptides. *Journal of the American Chemical Society* **2016**, *138* (43), 14214-14217.
(66) Schröder, H. V.; Zhang, Y.; Link, A. J. Dynamic covalent self-assembly of mechanically interlocked molecules solely made from peptides. *Nature Chemistry* **2021**, *13* (9), 850-857.
(67) Li, J.; Cvrtila, I.; Colomb-Delsuc, M.; Otten, E.; Otto, S. An "Ingredients" Approach to Functional Self-Synthesizing Materials: A Metal-Ion-Selective, Multi-Responsive, Self-Assembled Hydrogel. *Chemistry – A European Journal* **2014**, *20* (48), 15709-15714.
(68) Nowak, P.; Colomb-Delsuc, M.; Otto, S.; Li, J. Template-Triggered Emergence of a Self-Replicator from a Dynamic Combinatorial Library. *Journal of the American Chemical Society* **2015**, *137* (34), 10965-10969.
(69) Wu, X.; Xing, J.; Lyu, Y.; Yu, J.; Yang, J.; Qi, D.; Wang, X.; Lin, J.; Shao, G.; Wu, A.; et al. Kinetic control over co-self-assembly using an *in situ* dynamic covalent reaction resulting in a synergistic chemo-photodynamic therapy. *Cell Reports Physical Science* **2023**, *4* (10).
(70) Wu, X.; Zhang, D.; Pan, T.; Li, J.; Xie, Y.; Zhang, C.; Pan, C.; Zhang, Z.; Lin, J.; Wu, A.; et al. Stimuli-Responsive Codelivery System Self-Assembled from in Situ Dynamic Covalent Reaction of Macrocyclic Disulfides for Cancer Magnetic Resonance Imaging and Chemotherapy. *ACS Applied Materials & Interfaces* **2023**, *15* (38), 44773-44785.
(71) Lyu, Y.; Wu, X.; Papageorgiou, A. C.; Yang, J.; Wang, X.; Qi, D.; Li, J. Dynamic covalent macrocycles co-delivering genes and drugs against drug-resistant cancer. *Cell Reports Physical Science* **2022**, *3* (11).
(72) Cao, Y.; Yang, J.; Eichin, D.; Zhao, F.; Qi, D.; Kahari, L.; Jia, C.; Peurla, M.; Rosenholm, J. M.; Zhao, Z.; et al. Self-Synthesizing Nanorods from Dynamic Combinatorial Libraries against Drug Resistant Cancer. *Angewandte Chemie International Edition* **2021**, *60* (6), 3062-3070.
(73) Yang, J.; Wang, X.; Wu, X.; Lyu, Y.; Papageorgiou, A. C.; Li, J. Quantitative synthesis of dynamic combinatorial macrocycles accelerated by preorganization of AIEgens for live visualization of drug release. *Cell Reports Physical Science* **2024**, 102355.
(74) Lyu, Y.; Wu, X.; Papageorgiou, A. C.; Yang, J.; Wang, X.; Qi, D.; Li, J. Dynamic covalent macrocycles co-delivering genes and drugs against drug-resistant cancer. *Cell Reports Physical Science* **2022**, *3* (11), 101150.
(75) Bartolec, B.; Altay, M.; Otto, S. Template-promoted self-replication in dynamic combinatorial libraries made from a simple building block. *Chemical Communications* **2018**, *54* (93), 13096-13098.
(76) Mahon, C. S.; Jackson, A. W.; Murray, B. S.; Fulton, D. A. Investigating templating within Polymer-Scaffolded Dynamic Combinatorial Libraries. *Polymer Chemistry* **2013**, *4* (2), 368-377.
(77) Fulton, D. A. Dynamic Combinatorial Libraries Constructed on Polymer Scaffolds. *Organic Letters* **2008**, *10* (15), 3291-3294.

(78) Mahon, C. S.; McGurk, C. J.; Watson, S. M. D.; Fascione, M. A.; Sakonsinsiri, C.; Turnbull, W. B.; Fulton, D. A. Molecular Recognition-Mediated Transformation of Single-Chain Polymer Nanoparticles into Crosslinked Polymer Films. *Angewandte Chemie International Edition* **2017**, *56* (42), 12913-12918.
(79) Mahon, C. S.; Fulton, D. A. Templation-induced re-equilibration in polymer-scaffolded dynamic combinatorial libraries leads to enhancements in binding affinities. *Chemical Science* **2013**, *4* (9), 3661-3666.
(80) Mahon, C. S.; Jackson, A. W.; Murray, B. S.; Fulton, D. A. Templating a polymer-scaffolded dynamic combinatorial library. *Chemical Communications* **2011**, *47* (25), 7209-7211.
(81) Mahon, C. S.; Fascione, M. A.; Sakonsinsiri, C.; McAllister, T. E.; Bruce Turnbull, W.; Fulton, D. A. Templating carbohydrate-functionalised polymer-scaffolded dynamic combinatorial libraries with lectins. *Organic & Biomolecular Chemistry* **2015**, *13* (9), 2756-2761.
(82) Ruiz-Sanchez, A. J.; Higgs, P. L.; Peters, D. T.; Turley, A. T.; Dobson, M. A.; North, A. J.; Fulton, D. A. Probing the Surfaces of Biomacromolecules with Polymer-Scaffolded Dynamic Combinatorial Libraries. *ACS Macro Letters* **2017**, *6* (9), 903-907.
(83) Han, Y.; Nowak, P.; Colomb-Delsuc, M.; Leal, M. P.; Otto, S. Instructable Nanoparticles Using Dynamic Combinatorial Chemistry. *Langmuir* **2015**, *31* (46), 12658-12663.
(84) Nowak, P.; Saggiomo, V.; Salehian, F.; Colomb-Delsuc, M.; Han, Y.; Otto, S. Localized Template-Driven Functionalization of Nanoparticles by Dynamic Combinatorial Chemistry. *Angewandte Chemie International Edition* **2015**, *54* (14), 4192-4197.
(85) Carbajo, D.; Pérez, Y.; Bujons, J.; Alfonso, I. Live-Cell-Templated Dynamic Combinatorial Chemistry. *Angewandte Chemie International Edition* **2020**, *59* (39), 17202-17206.
(86) Corredor, M.; Carbajo, D.; Domingo, C.; Pérez, Y.; Bujons, J.; Messeguer, A.; Alfonso, I. Dynamic Covalent Identification of an Efficient Heparin Ligand. *Angewandte Chemie International Edition* **2018**, *57* (37), 11973-11977.
(87) Kriebisch, C. M. E.; Burger, L.; Zozulia, O.; Stasi, M.; Floroni, A.; Braun, D.; Gerland, U.; Boekhoven, J. Template-based copying in chemically fuelled dynamic combinatorial libraries. *Nature Chemistry* **2024**, *16* (8), 1240-1249.
(88) Balakrishna, B.; Menon, A.; Cao, K.; Gsänger, S.; Beil, S. B.; Villalva, J.; Shyshov, O.; Martin, O.; Hirsch, A.; Meyer, B.; et al. Dynamic Covalent Formation of Concave Disulfide Macrocycles Mechanically Interlocked with Single-Walled Carbon Nanotubes. *Angewandte Chemie International Edition* **2020**, *59* (42), 18774-18785.
(89) Kraus, J.; Meingast, L.; Hald, J.; Beil, S. B.; Biskupek, J.; Ritterhoff, C. L.; Gsänger, S.; Eisenkolb, J.; Meyer, B.; Kaiser, U.; et al. Simultaneous Inside and Outside Functionalization of Single-Walled Carbon Nanotubes. *Angewandte Chemie International Edition* **2024**, *63* (20), e202402417.
(90) Yu, J.; Qi, D.; Li, J. Design, synthesis and applications of responsive macrocycles. *Communications Chemistry* **2020**, *3* (1), 189.
(91) Parker, A. J.; Kharasch, N. The Scission of The Sulfur-Sulfur Bond. *Chemical Reviews* **1959**, *59* (4), 583-628.
(92) Foss, O. CHAPTER 9 - IONIC SCISSION OF THE SULFUR-SULFUR BOND. In *Organic Sulfur Compounds*, Kharasch, N. Ed.; Pergamon, 1961; pp 83-96.
(93) Kice, J. L. Electrophilic and nucleophilic catalysis of the scission of the sulfur-sulfur bond. *Accounts of Chemical Research* **1968**, *1* (2), 58-64.
(94) Danehy, J. P.; Doherty, B. T.; Egan, C. P. Oxidation of organic divalent sulfur by iodine. II. Equilibrating thiol-iodine-disulfide-hydrogen iodide system in acetic acid and evidence for sulfenyl iodide intermediates. *The Journal of Organic Chemistry* **1971**, *36* (17), 2525-2530.
(95) Shigeru, O. Organic sulfur chemistry: structure and mechanism. London: CRC Press: 1991.
(96) Otto, S. An Approach to the De Novo Synthesis of Life. *Accounts of Chemical Research* **2022**, *55* (2), 145-155.

(97) Adamski, P.; Eleveld, M.; Sood, A.; Kun, Á.; Szilágyi, A.; Czárán, T.; Szathmáry, E.; Otto, S. From self-replication to replicator systems en route to de novo life. *Nature Reviews Chemistry* **2020**, *4* (8), 386-403.
(98) Otto, S. Dynamic Molecular Networks: From Synthetic Receptors to Self-Replicators. *Accounts of Chemical Research* **2012**, *45* (12), 2200-2210.
(99) Mastalerz, M. Shape-Persistent Organic Cage Compounds by Dynamic Covalent Bond Formation. *Angewandte Chemie International Edition* **2010**, *49* (30), 5042-5053.
(100) Grubbs, R. H. Olefin metathesis. *Tetrahedron* **2004**, *60* (34), 7117-7140.
(101) Becker, M. R.; Watson, R. B.; Schindler, C. S. Beyond olefins: new metathesis directions for synthesis. *Chemical Society Reviews* **2018**, *47* (21), 7867-7881.
(102) Quaglio, D.; Zappia, G.; De Paolis, E.; Balducci, S.; Botta, B.; Ghirga, F. Olefin metathesis reaction as a locking tool for macrocycle and mechanomolecule construction. *Organic Chemistry Frontiers* **2018**, *5* (20), 3022-3055.
(103) Gedde, U. *Polymer physics*; Springer Science & Business Media, 1995.
(104) Doi, M.; Edwards, S. F.; Edwards, S. F. *The theory of polymer dynamics*; oxford university press, 1988.
(105) Richter, D.; Kruteva, M. Polymer dynamics under confinement. *Soft Matter* **2019**, *15* (37), 7316-7349, 10.1039/C9SM01141B.
(106) Bailey, E. J.; Winey, K. I. Dynamics of polymer segments, polymer chains, and nanoparticles in polymer nanocomposite melts: A review. *Progress in Polymer Science* **2020**, *105*, 101242.
(107) Eisenberg, H. DNA flexing, folding, and function. *Accounts of Chemical Research* **1987**, *20* (8), 276-282.
(108) Pan, T.; Sosnick, T. RNA FOLDING DURING TRANSCRIPTION. **2006**, *35* (Volume 35, 2006), 161-175.
(109) Martin, A. C. R.; Orengo, C. A.; Hutchinson, E. G.; Jones, S.; Karmirantzou, M.; Laskowski, R. A.; Mitchell, J. B. O.; Taroni, C.; Thornton, J. M. Protein folds and functions. *Structure* **1998**, *6* (7), 875-884.
(110) Liberles, D. A.; Teichmann, S. A.; Bahar, I.; Bastolla, U.; Bloom, J.; Bornberg-Bauer, E.; Colwell, L. J.; de Koning, A. P. J.; Dokholyan, N. V.; Echave, J.; et al. The interface of protein structure, protein biophysics, and molecular evolution. *Protein Science* **2012**, *21* (6), 769-785.
(111) Cheng, C.-C.; Chang, F.-C.; Yen, H.-C.; Lee, D.-J.; Chiu, C.-W.; Xin, Z. Supramolecular Assembly Mediates the Formation of Single-Chain Polymeric Nanoparticles. *ACS Macro Letters* **2015**, *4* (10), 1184-1188.
(112) Mavila, S.; Eivgi, O.; Berkovich, I.; Lemcoff, N. G. Intramolecular Cross-Linking Methodologies for the Synthesis of Polymer Nanoparticles. *Chemical Reviews* **2016**, *116* (3), 878-961.
(113) ter Huurne Gijs, M.; Palmans Anja, R. A.; Meijer, E. W. Supramolecular Single-Chain Polymeric Nanoparticles. *CCS Chemistry* **2019**, *1* (1), 64-82.
(114) Alqarni, M. A. M.; Waldron, C.; Yilmaz, G.; Becer, C. R. Synthetic Routes to Single Chain Polymer Nanoparticles (SCNPs): Current Status and Perspectives. *Macromolecular Rapid Communications* **2021**, *42* (11), 2100035.
(115) Ellis, R. J.; Van der Vies, S. M. J. A. r. o. b. Molecular chaperones. **1991**, *60* (1), 321-347.
(116) Hartl, F. U.; Bracher, A.; Hayer-Hartl, M. Molecular chaperones in protein folding and proteostasis. *Nature* **2011**, *475* (7356), 324-332.
(117) Ellgaard, L.; McCaul, N.; Chatsisvili, A.; Braakman, I. Co- and Post-Translational Protein Folding in the ER. *Traffic* **2016**, *17* (6), 615-638.
(118) Nitika; Porter, C. M.; Truman, A. W.; Truttmann, M. C. Post-translational modifications of Hsp70 family proteins: Expanding the chaperone code. *Journal of Biological Chemistry* **2020**, *295* (31), 10689-10708..
(119) Cortez, L.; Sim, V. The therapeutic potential of chemical chaperones in protein folding diseases. *Prion* **2014**, *8* (2), 197-202.

(120) Balchin, D.; Hayer-Hartl, M.; Hartl, F. U. In vivo aspects of protein folding and quality control. *Science* **2016**, *353* (6294), aac4354.
(121) Hosono, N.; Gillissen, M. A. J.; Li, Y.; Sheiko, S. S.; Palmans, A. R. A.; Meijer, E. W. Orthogonal Self-Assembly in Folding Block Copolymers. *Journal of the American Chemical Society* **2013**, *135* (1), 501-510.
(122) Moreno, A. J.; Lo Verso, F.; Sanchez-Sanchez, A.; Arbe, A.; Colmenero, J.; Pomposo, J. A. Advantages of Orthogonal Folding of Single Polymer Chains to Soft Nanoparticles. *Macromolecules* **2013**, *46* (24), 9748-9759.
(123) Lo Verso, F.; Pomposo, J. A.; Colmenero, J.; Moreno, A. J. Multi-orthogonal folding of single polymer chains into soft nanoparticles. *Soft Matter* **2014**, *10* (27), 4813-4821, 10.1039/C4SM00459K.
(124) Blazquez-Martín, A.; Verde-Sesto, E.; Moreno, A. J.; Arbe, A.; Colmenero, J.; Pomposo, J. A. Advances in the Multi-Orthogonal Folding of Single Polymer Chains into Single-Chain Nanoparticles. In *Polymers*, 2021; Vol. 13.
(125) Yarlagadda, V.; Akkapeddi, P.; Manjunath, G. B.; Haldar, J. Membrane Active Vancomycin Analogues: A Strategy to Combat Bacterial Resistance. *Journal of Medicinal Chemistry* **2014**, *57* (11), 4558-4568.
(126) Corbett, P. T.; Sanders, J. K. M.; Otto, S. Exploring the Relation between Amplification and Binding in Dynamic Combinatorial Libraries of Macrocyclic Synthetic Receptors in Water. *Chemistry – A European Journal* **2008**, *14* (7), 2153-2166.
(127) Pinto, L. F.; Correa, J.; Martin-Pastor, M.; Riguera, R.; Fernandez-Megia, E. The Dynamics of Dendrimers by NMR Relaxation: Interpretation Pitfalls. *Journal of the American Chemical Society* **2013**, *135* (5), 1972-1977.
(128) Pinto, L. F.; Riguera, R.; Fernandez-Megia, E. Stepwise Filtering of the Internal Layers of Dendrimers by Transverse-Relaxation-Edited NMR. *Journal of the American Chemical Society* **2013**, *135* (31), 11513-11516.
(129) Liao, S.; Wei, L.; Abriata, L. A.; Stellacci, F. Control and Characterization of the Compactness of Single-Chain Nanoparticles. *Macromolecules* **2021**, *54* (24), 11459-11467.
(130) Nagao, M.; Miura, Y. Correlation between Self-Folding Behavior of Amphiphilic Polymers and Their Molecular Flexibility. *ACS Macro Letters* **2023**, *12* (6), 733-737.
(131) Balendiran, G. K.; Dabur, R.; Fraser, D. The role of glutathione in cancer. *Cell Biochemistry and Function* **2004**, *22* (6), 343-352.
(132) Webb, B. A.; Chimenti, M.; Jacobson, M. P.; Barber, D. L. Dysregulated pH: a perfect storm for cancer progression. *Nature Reviews Cancer* **2011**, *11* (9), 671-677.
(133) George, E. P.; Ritchie, R. O. High-entropy materials. *MRS Bulletin* **2022**, *47* (2), 145-150.
(134) Ma, Y.; Ma, Y.; Wang, Q.; Schweidler, S.; Botros, M.; Fu, T.; Hahn, H.; Brezesinski, T.; Breitung, B. High-entropy energy materials: challenges and new opportunities. *Energy & Environmental Science* **2021**, *14* (5), 2883-2905.
(135) Sun, Y.; Dai, S. High-entropy materials for catalysis: A new frontier. *Science Advances 7* (20), eabg1600.
(136) Mei, H.; Zhang, Y.; Zhang, P.; Ricciardulli, A. G.; Samorì, P.; Yang, S. Entropy Engineering of 2D Materials. *Advanced Science* **2024**, *n/a* (n/a), 2409404.
(137) Han, L.; Zhu, S.; Rao, Z.; Scheu, C.; Ponge, D.; Ludwig, A.; Zhang, H.; Gutfleisch, O.; Hahn, H.; Li, Z.; et al. Multifunctional high-entropy materials. *Nature Reviews Materials* **2024**.
(138) Zhu, H.; Chen, L.; Sun, B.; Wang, M.; Li, H.; Stoddart, J. F.; Huang, F. Applications of macrocycle-based solid-state host–guest chemistry. *Nature Reviews Chemistry* **2023**, *7* (11), 768-782.
(139) Stupp, S. I.; LeBonheur, V.; Walker, K.; Li, L. S.; Huggins, K. E.; Keser, M.; Amstutz, A. Supramolecular Materials: Self-Organized Nanostructures. *Science* **1997**, *276* (5311), 384-389.
(140) Amabilino, D. B.; Smith, D. K.; Steed, J. W. Supramolecular materials. *Chemical Society Reviews* **2017**, *46* (9).

(141) Dumele, O.; Chen, J.; Passarelli, J. V.; Stupp, S. I. Supramolecular Energy Materials. *Advanced Materials* **2020**, *32* (17), 1907247.
(142) Sheehan, F.; Sementa, D.; Jain, A.; Kumar, M.; Tayarani-Najjaran, M.; Kroiss, D.; Ulijn, R. V. Peptide-Based Supramolecular Systems Chemistry. *Chemical Reviews* **2021**, *121* (22), 13869-13914.
(143) Zhang, X.; Dai, X.; Gao, L.; Xu, D.; Wan, H.; Wang, Y.; Yan, L.-T. The entropy-controlled strategy in self-assembling systems. *Chemical Society Reviews* **2023**, *52* (19), 6806-6837.
(144) Donets, S.; Sommer, J.-U. Molecular Dynamics Simulations of Strain-Induced Phase Transition of Poly(ethylene oxide) in Water. *The Journal of Physical Chemistry B* **2018**, *122* (1), 392-397.
(145) Liese, S.; Gensler, M.; Krysiak, S.; Schwarzl, R.; Achazi, A.; Paulus, B.; Hugel, T.; Rabe, J. P.; Netz, R. R. Hydration Effects Turn a Highly Stretched Polymer from an Entropic into an Energetic Spring. *ACS Nano* **2017**, *11* (1), 702-712.
(146) Mayumi, K. Molecular dynamics and structure of polyrotaxane in solution. *Polymer Journal* **2021**, *53* (5), 581-586.
(147) Zhang, S.; Li, W.; Luan, J.; Srivastava, A.; Carnevale, V.; Klein, M. L.; Sun, J.; Wang, D.; Teora, S. P.; Rijpkema, S. J.; et al. Adaptive insertion of a hydrophobic anchor into a poly(ethylene glycol) host for programmable surface functionalization. *Nature Chemistry* **2023**, *15* (2), 240-247.
(148) Zhang, S.; Srivastava, A.; Li, W.; Rijpkema, S. J.; Carnevale, V.; Klein, M. L.; Wilson, D. A. Molecular Engineering of pH-Responsive Anchoring Systems onto Poly(ethylene glycol) Corona. *Journal of the American Chemical Society* **2023**, *145* (19), 10458-10462.
(149) Rogers, B. A.; Okur, H. I.; Yan, C.; Yang, T.; Heyda, J.; Cremer, P. S. Weakly hydrated anions bind to polymers but not monomers in aqueous solutions. *Nature Chemistry* **2022**, *14* (1), 40-45.
(150) Zhang, Y.; Furyk, S.; Bergbreiter, D. E.; Cremer, P. S. Specific Ion Effects on the Water Solubility of Macromolecules: PNIPAM and the Hofmeister Series. *Journal of the American Chemical Society* **2005**, *127* (41), 14505-14510.
(151) Mayer, M.; Meyer, B. Characterization of Ligand Binding by Saturation Transfer Difference NMR Spectroscopy. *Angewandte Chemie International Edition* **1999**, *38* (12), 1784-1788.
(152) Mayer, M.; Meyer, B. Group Epitope Mapping by Saturation Transfer Difference NMR To Identify Segments of a Ligand in Direct Contact with a Protein Receptor. *Journal of the American Chemical Society* **2001**, *123* (25), 6108-6117.
(153) Poole Iii, D. A.; Bobylev, E. O.; Mathew, S.; Reek, J. N. H. Entropy directs the self-assembly of supramolecular palladium coordination macrocycles and cages. *Chemical Science* **2022**, *13* (34).
(154) Shimizu, S.; McLaren, W. M.; Matubayasi, N. The Hofmeister series and protein-salt interactions. *The Journal of Chemical Physics* **2006**, *124* (23), 234905.
(155) Wickner, W.; Schekman, R. Membrane fusion. *Nature Structural & Molecular Biology* **2008**, *15* (7), 658-664.
(156) Blumenthal, R.; Clague, M. J.; Durell, S. R.; Epand, R. M. Membrane Fusion. *Chemical Reviews* **2003**, *103* (1), 53-70.
(157) Jahn, R.; Cafiso, D. C.; Tamm, L. K. Mechanisms of SNARE proteins in membrane fusion. *Nature Reviews Molecular Cell Biology* **2024**, *25* (2), 101-118.

List of Figures, Tables and Appendices

Figures

Tables

TURUN
YLIOPISTO
UNIVERSITY
OF TURKU

ISBN 978-952-02-0181-4 (print)
ISBN 978-952-02-0182-1 (pdf)
ISSN 0082-7002 (print)
ISSN 2343-3175(online)

Punamusta oy, Joensuu, Finland 2025